A STUDY ON LASER WELDABILITY IMPROVEMENT OF NEWLY DEVELOPED HAYNES 282 SUPERALLOY

By

LAWRENCE OPEYEMI OSOBA

A Thesis Submitted to the Faculty of Graduate Studies of

The University of Manitoba

in partial fulfillment of the requirements of the degree of

Doctor of Philosophy

Department of Mechanical and Manufacturing Engineering

University of Manitoba

Winnipeg

Abstract

Haynes alloy 282 is a new gamma prime (γ') precipitation strengthened nickel-base superalloy developed for high temperature applications in land-based and aero turbine engines. Joining is a crucial process both during the manufacturing of new components and repair of service-damaged turbine parts. Unfortunately, the new superalloy cracks during laser beam welding (LBW), which is an attractive technique for joining superalloys components due to its low heat input characteristic that preclude the geometrical distortion of welded components. This research is therefore initiated with the goal of studying and developing an effective approach for preventing or minimizing cracking during LBW of the new superalloy Haynes 282. Careful and detailed electron microscopy and spectroscopy study reveal, for the first time, the formation of sub-micron grain boundary M_5B_3 particles, in the material. Microstructural study of welded specimens coupled with Gleeble thermo-mechanical physical simulations shows that the primary cause of weld heat affected zone (HAZ) cracking in the alloy is the sub-solidus liquation reaction of intergranular M_5B_3 borides in the material. Further weldability study showed that the HAZ liquation cracking problem worsens with reduction in welding heat input, which is normally necessary to produce the desired weld geometry with minimum distortion. In order to minimize the HAZ cracking during low heat input laser welding, microstructural modification of the alloy by heat treatment at 1080 - 1100^{o}C has been developed. The pre-weld heat treatment minimizes cracking in the alloy by reducing the volume fraction of the newly identified M_5B_3 borides, while also minimizing non-equilibrium grain boundary segregation of boron liberated during dissociation of the

boride particles. Further improvement in resistance to cracking was produced by subjecting the material to thermo-mechanically induced grain refinement coupled with a pre-weld heat treatment at 1080^{o}C. This approach produces, for the first time, crack-free welds in this superalloy, and the benefit of this procedure in preventing weld cracking in the new material is preserved after post-weld heat treatment (PWHT), as additional cracking was not observed in welded specimens subjected to PWHT.

Acknowledgements

I thank my supervisor, Dr O.A. Ojo for given me the opportunity to work on this research topic. I am grateful for his guidance, mentorship, enormous research contribution, access to metallurgical research facilities and support throughout the course of this study. I also appreciate my advisory committee members, Dr J.R. Cahoon and Dr E. El-Salakawy for their cooperation and timely advice in the course of this study.

The financial assistance of Natural Science and Engineering Research Council of Canada (NSERC) and the University of Manitoba through the University of Manitoba Graduate fellowship is highly appreciated. I thank Haynes International Incorporation, USA for the material supplied as well as Standard Aero Ltd., Winnipeg, Canada for their assistance with the laser welding process.

I thank Messer Jon Van Dorp, Don Madis, Mike Boswisk, Dr R.G Ding, Dr Shidu, Dr Khan and Garry Good for their technical assistance. I also thank my colleagues and friends - Mr & Mrs Oyedele Ola, Richard Buckson, Mark Amegadzie, Omudhohwo Oshobe, Juhiana Hunedy, Jinal Sanghvi, Nana Tsiquayeaba, Dr, Ayo Afolabi, Dr, Anthony Odiwe, Muyiwa Olagoke and Mr & Mrs Tope Elemeje.

I am profoundly thankful to my siblings - Professor G. A. Osoba, Dr F. O. Oshoba, Dr J. B. Osoba and Mrs A. Owolabi for their continue support in all ramifications. I acknowledge the invaluable support and encouragement of Dr. & Mrs Odeshi, Dr Samuel Paul, Professor S.A. Balogun and Pastor & Mrs Okunnu.

I specially appreciate my darling wife Adunola for her trust and motivation towards the realization of this program and to my lovely children - Faith Toluwani, David Olamilekan and Daniella Akorede. The sacrifices and inconveniences you endured throughout the period of my study is appreciated. Finally, my wholehearted appreciation goes to God, The Almighty, The giver of life, The unsearchable source of all wisdom and understanding without whom there would have been no progress or any life accomplishment.

Dedication

To

My mother, Ebudola Regina Osoba

and

My wife, Adunola Osoba

TABLE OF CONTENTS

List of Figures

List of Tables

List of Copyrighted Materials for which permission was obtained

Figure 2-2: Source – "Encyclopedia of Material Science and Engineering" Reprinted with permission from Elsevier (10th April, 2012) and the Author (27th March, 2012).

Figure 2-3: Source – "Welding Metallurgy" 2nd Edition by Sindo Kuo. Reprinted with permission from Global Right Department, John Willy and Sons, Incorporation - October 28th, 2011

Figure 2-4: Source – "Welding Metallurgy" 2nd Edition by Sindo Kuo. Reprinted with permission from Global Right Department, John Willy and Sons, Incorporation - October 28th, 2011

Figure 2-7: Source – "Welding Metallurgy" 2nd Edition by Sindo Kuo. Reprinted with permission from Global Right Department, John Willy and Sons, Incorporation - October 28th, 2011

Figure 2-8: Source: "Treatise on Materials Science and Technology: Embrittlement of Engineering Alloys" by H. D. Solomon. Reprinted with permission from the Elsevier (1st May, 2012)

Figure 2-9: Source – "ASM Technical Guide 1998" Reprinted with permission from ASM – April 4th, 2012

Figure 2-10: Source: "British Welding Journal" by J.C. Borland. Reproduced courtesy of TWI Ltd (22nd May, 2012)

Figure 2-11: Source – "Foundry 1952" Reprinted with permission from Penton Media Inc. – April 20th, 2012

Figure 2-12: Source – "Foundry 1952" Reprinted with permission from Penton Media Inc. April 20th, 2012

Figure 2-13: Source: "British Welding Journal" by J.C. Borland. Reproduced courtesy of TWI Ltd (22nd May, 2012)

Figure 2-14: Source: “British Welding Journal” by J.C. Borland. Reproduced courtesy of TWI Ltd (22nd May, 2012)

Figure 2-15: Source – Welding Journal, Reprinted with permission

Figure 2-16: Source – Welding Journal, Reprinted with permission

Figure 2-17: Source – Welding Journal, Reprinted with permission

Figure 2-18: Source – “Welding Metallurgy” 2nd Edition by Sindo Kuo. Reprinted with permission from Global Right Department, John Willy and Sons, Incorporation - October 28th, 2011

Figure 2-19: Source – “Welding Metallurgy” 2nd Edition by Sindo Kuo. Reprinted with permission from Global Right Department, John Willy and Sons, Incorporation - October 28th, 2011

Figure 2-20: Source – PhD Thesis Lin Wangen, 1991” Reprinted with permission from the Author - April 17th, 2012.

Figure 2-21: Source – “PhD Thesis Lin Wangen, 1991” Reprinted with permission from the Author - April 17th, 2012.

Figure 2-22: Source - “PhD Thesis Lin Wangen, 1991” Reprinted with permission from the Author - April 17th, 2012.

Figure 2-23: Source - Welding Journal, Reprinted with permission

Figure 4-18: Source – Metallurgical and Materials Transaction A. Reprinted with permission from RightsLink / Springer 23rd July, 2012.

CHAPTER 1

INTRODUCTION

1.1 General Overview

Superalloys are high performance heat-resistant materials which have high strengths at elevated temperatures and good corrosion and oxidation resistance. Subsequent to their development and continual improvement, they have found applications in aircrafts, marine and industrial gas turbines, rocket engines, nuclear reactors and petrochemical equipment [1].

There is, however, an ever increasing demand to increase the overall efficiency of gas turbine, so as to improve fuel economy and reduce greenhouse gas emission. New alloy designs and upgrade of existing alloys as means of producing better performance components have been used in the past few decades, for example, compositional modification of Inconel 718 to produce Inconel 718 Plus and the development of new alloys, such as Haynes alloy 282. The Haynes alloy 282 used in this study is a new gamma prime (**γ'**) precipitation strengthened nickel-base superalloy developed in 2005 to meet the challenges of higher turbine engine service temperature and efficiency. This new alloy exhibits a unique combination of excellent creep properties and thermal stability that surpasses those of some of the existing superalloys, such as Waspaloy, Inconel 718 and Haynes alloy 263. Hence, Haynes alloy 282 is referred to as a "fabricable γ' strengthened superalloy" [2].

Nevertheless, as component integrity and turbine efficiency increase, so do the geometric complexities of the engine design, such that large cast sections components are now being re-designed to be made up of smaller parts that are joined together by appropriate fusion welding process during fabrication. In addition, the repair of damaged or service degraded parts is often preferred to total replacement owing to the high manufacturing cost of new components and long delivery time. Therefore, commercial application of a new alloy is significantly influenced by the ease of fabrication and repair by joining process. Fusion welding is a known economical and versatile technique for joining nickel-base superalloys, both during fabrication as well as in repairing in-service damaged components. Laser beam welding (LBW) is one of the fusion welding processes which has attracted considerable interest in recent years for fabrication and repair of complex aerospace structures due to its high speed, flexibility, high-energy density and power transfer rate to produce low heat input welds with reduced heat affected zone and physical distortions.

The new Haynes alloy 282, like other precipitation hardened nickel-base superalloys is susceptible to cracking during fusion welding. The causes of weld cracking in this new alloy were not known and limited information about the weldability of the material was available in the literature prior to this research. Accordingly, this PhD thesis research was set up with the following key objectives.

1.2 Research Objectives

1. to perform a comprehensive and systematic study, involving careful and detailed microstructural examination, analysis and physical simulation, to determine the causes of cracking in Haynes alloy 282 during LBW; and

2. to use the understanding of causes of cracking to develop suitable procedure for preventing or minimizing cracking in the newly developed Haynes alloy 282 during LBW.

1.3 Methodology

In order to achieve these goals, Haynes alloy 282 material supplied by Haynes International Incorporation, Kokomo, USA, in the form of mill bright-annealed plates were cut to welding test specimens and subjected to various pre-weld heat treatments. LBW was carried out by using a CO_2-gas laser beam welder at Standard Aero, Winnipeg. Physical simulation of HAZ microstructure in the material was performed by using Gleeble thermo-mechanical simulation system at the University of Manitoba. Microstructure of all specimens were examined and characterised by the use of standard metallographic techniques involving optical microscopy, electron microprobe analysis, analytical scanning electron and transmission electron microscopy and spectroscopy techniques. In addition, secondary ion mass spectroscopy (SIMS) was used to study elemental grain boundary segregation, while, differential scanning calorimetry (DSC) was used to determine the major phase transformation temperatures in the alloy.

1.4 Major Findings

An electron microscopy study of the standard heat treated alloy shows that, in addition to $M_{23}C_6$ and MC-type carbide particles that were previously reported to be present in the alloy, precipitates based on a new phase, M_5B_3 boride, which has not been reported in the new alloy, are formed along the intergranular region. Formation of the grain boundary M_5B_3 borides is found to significantly reduce the ductility of the new alloy at high temperatures. The ductility degradation of the alloy at high temperatures owing to the liquation reaction of the boride particles is found to be the primary cause of the HAZ cracking in the alloy during LBW. Complete dissolution of the liquating M_5B_3 particles by pre-weld heat treatment exacerbates rather than reduce susceptibility to cracking due to non-equilibrium intergranular segregation of boron (B) atoms liberated by the complete dissolution of the boride particles, during cooling from heat treatment temperature. Consequently, to reduce HAZ cracking, a pre-weld heat treatment at 1080^oC - 1100^oC, which reduces the volume fraction of the M_5B_3 particles and minimizes non-equilibrium grain boundary B segregation has been developed and experimentally confirmed to be effective.

Further improvement in cracking resistance to produce crack-free welds is achieved by subjecting the alloy to thermo-mechanically induced grain refinement coupled with a pre-weld heat treatment at 1080^oC. Gleeble hot ductility test shows that formation of crack-free welds is unexplainable by mere reduction in grain size without considering the effect of grain refinement on the intergranular liquid produced by the sub-solidus liquation of the M_5B_3 borides. In addition, the research shows that the benefit

of the new approach developed in this study in improving the resistance of the alloy to weld cracking is not undermined during post-weld heat treatment (PWHT).

Careful consideration of the findings in this study will enable the effective use of LBW for the fabrication and repair of service-damaged aero-engine components made of Haynes alloy 282. This will significantly enable a wider industrial application of the new material which is designed and developed for better aircraft engine efficiency, and as such, contribute to the cost-reduction, safety enhancement and reduction of green-house emission through better aero-engine efficiency. The novel contribution of the research has been published or accepted in 3 refereed international journals and 1 in a conference proceeding (full paper).

1.5 Thesis Organization

This dissertation consists of six chapters. The outline of each chapter is as follows,

- Chapter 1 contains a brief introduction of the subject matter, problem definition and methodology,
- Chapter 2 comprises a general literature review on the physical and welding metallurgy of nickel-base superalloys as well as available information on Haynes alloy 282,
- Chapter 3 provides details of the experimental procedure and instruments used,
- Chapter 4 provides analysis, discussion and results of the experimental work,
- Chapter 5 presents a summary of the major findings and conclusions, and

- Chapter 6 provides suggestions for future research.

CHAPTER 2

LITERATURE REVIEW

2.1 Introduction

This chapter contains a review of literature, including, literature review of some selected thesis [3-5], on the physical metallurgy of nickel-base superalloys in general as well as available information on wrought Haynes alloy 282. This is followed by a general review of conventional and high energy beam fusion welding processes, welding metallurgy, residual stresses, weld defects, weld cracking and theories that include the review of some weldability testing techniques and ends with the objectives and scope of the thesis.

The physical metallurgy of nickel-base superalloys is complex due to the need to produce elevated temperature materials with remarkable tensile strength, creep rupture strength, corrosion and oxidation resistance as required in gas turbine engine applications [6]. The excellent corrosion and oxidation resistance of nickel-base superalloy are achieved with the addition of alloying elements, such as chromium (Cr), aluminum (Al), and molybdenum (Mo), while the tensile and creep rupture strength are first enhanced with the addition of elements that have slow diffusivity such as Mo and tungsten (W) during production, followed by precipitation hardening prior to or after processing and before deployment to service. The high temperature strength of nickel-base superalloys, in particular, is mainly derived from the precipitation of an ordered LI_2 intermetallic Ni_3 (Al, Ti) γ' phase within the γ matrix or by precipitation of a DO_2 intermetallic Ni_3Nb γ'' phase. Niobium (Nb), titanium (Ti), Mo and Cr are the major metallic carbide formers

in superalloys, while boron (B) and zirconium (Zr) are added to enhance creep rupture properties [7]

2.2 Wrought Nickel-Base Haynes Alloy 282

The new Haynes alloy 282, is a γ' precipitation strengthened alloy in the class of Waspaloy and Rene 41, but with compositional modifications [2] as shown in Table 2-1. The tensile strength, creep rupture strength, as well as physical properties of the alloy are presented in Tables 2-2, 2-3 and 2-4, respectively [8].

Major compositional design of Haynes alloy 282 as compared to other alloys in its class are the lower concentrations of Al and Ti, which is a major limiting factor that controls the volume fraction and precipitation kinetics of the main strengthening phase, γ'. Cobalt (Co) is added to stabilize γ' by controlling the γ' solvus temperature apart from being a solid solution strengthener. The addition of Cr provides resistance to both oxidation and hot corrosion while Mo is primarily added to enhance creep strength, weight fraction and solvus of γ' [2]. The concentration of alloying elements, iron (Fe), silicon (Si) and manganese (Mn) are strictly limited to a maximum, and also, there is a noticeable preclusion of Nb in the alloy. The commercially recommended pre-weld solution heat treatment (SHT) procedure for the alloy ranges from 1121^{o}C to 1149^{o}C followed by rapid cooling.

Major phases reported in the alloy prior to and after SHT include: primary gamma (γ) phase and MC type carbide and carbonitride [2]. The size of MC type carbides ranges from 2 μm to about 15 μm, and they are intragranularly and intergranularly dispersed within the γ matrix. The estimated working temperature of Haynes alloy 282 is well

Table 2 - 1: Chemistry of wrought Haynes alloy 282 and other Ni-base superalloy in its class.

Element	**Weight Percent (wt. %)**			
	Haynes 282	**Waspaloy**	**Rene 41**	**Haynes 263**
Nickel (Ni)	**57 bal.**	58 bal.	52 bal.	52 bal.
Chromium (Cr)	**20**	19	19	20
Cobalt (Co)	**10**	13.5	11	20
Molybdenum (Mo)	**8.5**	4.3	10	6
Titanium (Ti)	**2.1**	3	3.1	2.4 max
Aluminum (Al)	**1.5**	1.5	1.5	0.6 max
Zirconium (Zr)	**-**	0.05	-	-
Iron (Fe)	**1.5 max**	2 max	5 max	0.7 max
Manganese (Mn)	**0.3 max**	0.1 max	0.1 max	0.4
Silicon (Si)	**0.15 max**	0.15 max	0.5 max	0.2
Carbon (C)	**0.06**	0.08	0.09	0.06
Boron (B)	**0.005**	0.006	0.006	0.005

Table 2 - 2: Average Tensile Properties of Haynes alloy 282* [8].

Temperature ^{o}C	0.2% Yield Strength (MPa)	Ultimate Tensile Strength (MPa)	% Elongation	% RA
Room Temp.	715	1147	30	31
600	645	1023	32	33
700	648	983	29	28
800	590	750	26	29
900	404	458	41	56
1000	75	115	77	98

* Solution Annealing: 1135^{o}C + Age- Hardening: 1010^{o}C/2hrs/AC +788^{o}C/8hrs/AC.

Source: Alloy Digest Haynes 282. Reprinted with permission of ASM (18thApril, 2012).

Table 2 - 3: Comparative Creep-Rupture Properties of Weld Metal to Base Metal of Haynes alloy 282* [8]

Temperature ^{o}C	Stress (MPa)	Material	Time to 1% Creep (Hrs)	Time to Rupture (Hrs)
760	345	Base Metal*	96.8	237.5
		All Weld Metal**	197.0	364.8
927	48	Base Metal*	335.6	792.3
		All Weld Metal**	648.0	950.5

* Solution Annealed + Age-Hardened, **GMAW Welded + Solution Annealed + Age-Hardened

Source: Alloy Digest Haynes 282. Reprinted with permission of ASM (18thApril, 2012).

Table 2 - 4: Mechanical/Physical Properties of Haynes alloy 282* [8]

Melting Range	1300-1375^{o}C
Density	8270 Kg/m^{3}
Thermal Conductivity at 1000^{o}C	28.9 W/m·k
Coefficient of Thermal Expansion at 1000^{o}C	16.9 µm/m·k
Young Modulus at 1000^{o}C	140 GPa
Shear Modulus at 1000^{o}C	51 GPa
Poisson Ratio at 1000^{o}C	0.363

* Age-Hardened at 1010^{o}C /2 hour /air cool + 788^{o}C/ 2 hour/air cool

Source: Alloy Digest Haynes 282. Reprinted with permission of (ASM 18thApril, 2012).

above 800^{o}C. Since its introduction in 2005 this alloy has received considerable attention as a potential candidate for several applications in both aero- and land-based power generation gas turbine engines [9].

Waspaloy is a γ' strengthened wrought nickel-base superalloy developed in the late 1940s by Pratt & Whitney. Since then, Waspaloy has been widely used for turbine disks, blades and fasteners. The working temperature of Waspaloy is about 700^{o}C [10], and its extensive use has been attributed to the high creep resistance at elevated temperature. Long term creep rupture strength of about 300 MPa at 100,000 hours at 700^{o}C can be achieved by Waspaloy, whereas turbine rotor material requires only 100 MPa at 700^{o}C [11]. Nonetheless, Waspaloy is susceptible to crack formation in the fusion zone and heat affected zone during welding and PWHT [6]. The standard pre-weld solution heat treatment for Waspaloy involves a solution annealing heat treatment at 1080^{o}C for 4 hours followed by water quenching and holding at 850^{o}C for 2 hours, then air cooled, plus holding at 760^{o}C for 16 hours, and followed by air cooling. This heat treatment is known to produce optimum creep and stress-rupture properties in the alloy. Major phases reported in Waspaloy includes: primary and secondary γ' phases (24 mole % at 760^{o}C), MC and $M_{23}C_6$ type carbides.

Rene 41, like Waspaloy and Haynes alloy 282, is also principally strengthened by γ' and has found useful applications in the welding of stationary structural components of jet and gas turbine engines that operate at temperatures up to about 900^{o}C. Although generally weldable, the susceptibility to cracking depends on the pre-weld and PWHT cycles employed [12]. The major phases present in Rene 41 includes: γ' phase (27 mole % at 760^{o}C), MC, M_6C, and $M_{23}C_6$ type carbides. In general, of all the three families of

superalloys, precipitation strengthened nickel-base and iron-nickel-base superalloys are considered to be less weldable than cobalt-base superalloys. This can be attributed to the presence of the γ' strengthening phase, in that when fusion welded, these alloys tend to be susceptible to hot cracking and PWHT cracking.

2.2.1 Microstructure of Wrought Nickel-Base Superalloys

The composition (elemental wt %) of wrought nickel-base superalloys varies from alloy to alloy, and hence the non-uniformity of their microstructure. However, major phases common to wrought superalloy and their influence on the mechanical and physical properties are discussed as follows.

2.2.1.1 The Gamma (γ) Phase

The gamma (γ) phase is a continuous matrix of face centered cubic (FCC) nickel-base austenite that usually contains a high percentage of solid solution elements, such as Co, Cr, Mo, W, Al, Nb and Ti [13-15]. These solid solution elements are mostly 'd' block elements which differ from nickel in atomic diameter by 1-18%, and usually occupy substitutional atomic positions in nickel crystal lattice, producing a distorted lattice with a spherical symmetrical stress field. This stress field can interact with that around a dislocation, producing an elastic solute atom-dislocation interaction that results in solid solution strengthening. In essence, the stress field around the atom of solid solution elements interacts with dislocation stress field and increases the stress required to move a dislocation by an amount given by Mott and Nabarro [16-17] as:

$$\Delta\sigma = G\delta^{4/3}c\left[\frac{c^{2/3}}{2\pi}\left(In\frac{1}{c}\right)^{4}\right]^{1/3} \quad \text{---------- (2.1)}$$

where **δ** is the lattice misfit, G is the modulus, σ is the stress and '**c**' is the solute concentration. In addition to strength enhancement, the Ni-γ phase can withstand severe temperature and time excursions. This endurance is attributed to many factors, such as the high tolerance of nickel for alloying without phase instability because of its nearly filled third electron shell [17]. The tendency of elemental Cr addition to form Cr_2O_3 - a rich protective scale with low cation vacancy content, thereby restricting the diffusion rate of metallic elements outwards, and prevents the diffusion of non-metallic elements, such as, oxygen (O), nitrogen (N), sulphur (S) and other aggressive atmospheric elements inward. Also, at high temperatures, there is a strong tendency to form Al_2O_3 - a rich scale with exceptional resistance to oxidation which is similar in characteristic to the rich protective scale of Cr_2O_3 [15].

2.2.1.2 Gamma Prime (γ')

The high temperature strength of nickel-base superalloys is derived from the precipitation of γ'- an FCC LI_2 ordered intermetallic compound Ni_3 (Al, Ti). A typical unit cell of the LI_2 crystal structure of the γ' phase is shown in Figure 2-1. This γ' particle, form in alloys that contain Ti and Al in amounts which exceed its solubility in nickel rich γ matrix as a coherent precipitate phase. Ardell [18] in his review on precipitation hardening, concluded that in nickel-base superalloys, γ' precipitation occurs by homogenous nucleation with low surface energy followed by growth and coarsening, during which the volume fraction of precipitates remains constant with extraordinary long-term stability. In addition to Al and Ti as major constituents of the γ' phase, it has been suggested that the γ' phase may also consist of several other solute elements in trace

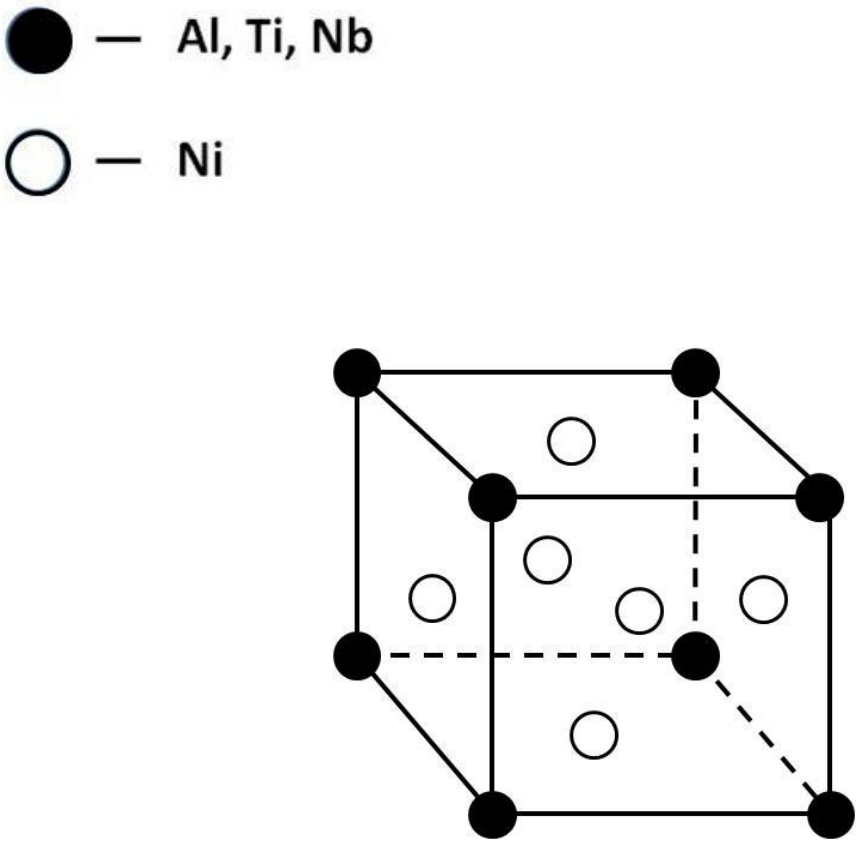

Figure 2-1: Unit Cell illustrating LI_2 ordered FCC lattice of γ' phase

amounts, which results in a more complex chemical compositions. Fayman [19] found that coarse primary γ' particles in Waspaloy are rich in Al and Ti whereas the fine secondary γ` particles are richer in Cr, Fe and Mo. The composition of the primary and secondary γ` particles (wt. %) were reported as ($Ni._{75}Co._{03}Cr._{02}Mo._{02}Ti._{10}Al._{07}Fe._{004}$) and ($Ni._{72}Co._{03}Cr._{04}Mo._{05}Ti._{10}Al._{06}Fe._{006}$), respectively.

Although the γ' precipitate is coherent with the matrix, there exists a small misfit at the γ-γ' interface [20], the magnitude of which is known to influence the γ' precipitate morphology [21]. Hagel and Beattie [22] found that γ' occurs as spheres at 0-0.2% lattice mismatch, becomes cubes at mismatches around 0.5-1.0% and then plates at mismatches above 1.25%. The mechanical properties of nickel-base superalloys are strongly influenced by the morphology, distribution and size of γ' precipitates within the γ matrix. Strength has been related to the interactions between γ' particles and moving dislocations, in that when the particle size is small, moving dislocation tends to shear the particle, whereas when the particle is large, it is by-passed. When precipitates are sheared, under applied strain (compressive or tensile), the strength of a γ' precipitation strengthened nickel-base alloy will now depend on (i) Order Hardening and (ii) Coherency Hardening.

Order Hardening

In this case, strengthening is achieved when the ordered γ' coherent precipitates are sheared by a glide dislocation that moves through the matrix, creating an anti-phase boundary (APB) fault on the slip plane of the precipitate phase in the process. Dislocation travelling through a γ-γ' system moves in pairs, shearing the γ' phase particles with the

formation of APB. The first dislocation is followed by the second dislocation that restores the order in the sheared particles by removing the APB that was created by the first. The shearing of the γ' precipitate phase by the dislocation system eventually produces an ordering effect within the γ-γ' system which increases the amount of energy required to pass dislocations through the precipitates [23-25]. As such, the higher the APB energy, the higher is the force required for dislocations to shear through the alloy matrix. Nickel-base superalloys with high volume fraction of γ' show a remarkable increase in strength with increasing temperature up to 800^{o}C as a result of the increase in degree of ordered hardening with increase temperature [13]. For a single dislocation, the increase in strength is given by Brown [26] as:

$$\Delta\tau = \gamma_0^{3/2} / 2b\left[4fr/\pi\Gamma\right]^{1/2} \text{ ---------- (2.2)}$$

and for a dislocation pair

$$\Delta\tau = \gamma_o / 2b\{\left[4\gamma_o fr/\pi\Gamma\right]^{1/2} - f\} \text{ ---------- (2.3)}$$

where $\boldsymbol{\gamma_o}$ is the specific APB energy, **r** is the average dimension of the particle intersected by a slip band, **b** is the Burgers vector of the matrix, **f** is the volume fraction of the precipitates and **Γ** is the line tension of a dislocation.

Coherency Hardening

The coherency hardening mechanism, which is also known as misfit hardening, has been attributed to the interaction of glide dislocations with the elastic coherency strain field around coherent γ' precipitates. The coherent strain field around a precipitate makes it difficult for glide dislocation to penetrate the γ' precipitates during both γ' cutting and

by-passing situations encountered during deformation. The strain field is a result of lattice misfit measured as the degree of disregistry between the γ and the γ' phases irrespective of the similarities between their crystal structure as well as the closeness of their lattice parameters. The interaction of glide dislocation with this strain field ultimately increases the critical resolved shear stress (CRSS) to cut through or by-pass a particle by movement of dislocation [21]. For coherency hardening, the increase in yield strength or the CRSS $\Delta\tau_{CRSS}$ is given as:

$$\Delta\tau_{CRSS} = 3G_{\Sigma}{}^{3/2}\left[\frac{hf}{2b}\right]^{1/2} \quad \text{---------- (2.4)}$$

where **G** is the modulus, **ε** is the constrained lattice strain and ***h*** is the mean particle diameter. b and f are as defined in Equations 2.2 and 2.3

Dislocation By-passing of γ'

The strength (hardness) of precipitation strengthened nickel-base superalloys is also influenced by the γ' precipitate particle size. As the size of the γ' particles increase, the tendency for a moving dislocation to by-pass large γ' particles, either by looping or dislocation climb becomes considerably higher. The critical size for the change in mechanism from cutting into by-passing depends on the alloy chemistry and can vary from about 300 Å to 2500 Å; higher sizes for alloys with high Al + Ti, γ' volume fraction. The contribution of γ' particle by-passing to increase in critical resolved shear strength due to dislocation looping is given by Orowan [24] as:

$$\Delta\tau CRSS = 0.2\, Gb\phi\, 2/\lambda\ \ In\, h/2b \text{ ---------- (2.5)}$$

where h is the mean particle diameter, ϕ is the angle between the Burgers vector and tangent to the dislocation line, λ the mean interparticle spacing, and G the shear modulus of the matrix lattice. Usually, the relationship in Equation 2.5 only applies to particle sizes larger than those observed in conditions that corresponding to peak strength.

2.2.1.3 Carbides

The carbon (C) content of wrought nickel-base superalloys varies from 0.02 to about 0.2 percent (in cast superalloys, the C content can be up to 0.6 percent) and it is the C content that determines the amount of carbides [13]. Wide ranges of carbide types are formed during solidification from melt when carbon combines with reactive and refractory elements such as Ti, tantalum (Ta), Nb and hafnium (Hf). The formation commences once the C concentration exceeds 0.05% [25]. In general, carbides are hard, relatively stable and vary in size which ranges from a few to hundreds of microns. Carbides have an FCC structure with no distinct orientation with the matrix and are more brittle than the γ matrix. When present in an optimum amount, and properly distributed along grain boundaries, carbides positively influence high temperature strength, ductility and creep properties of nickel-base alloys. Their absence and/or distribution in non preferred morphologies causes coalesce of voids and excess grain boundary sliding during high temperature deformation and processing. Common types of carbides formed in wrought nickel-base superalloys are MC, $M_{23}C_6$ and M_6C [13].

MC type carbides are monocarbide with the general formula MC, where 'M' stands for metallic elements, such as Ti, Ta, Nb, or W. The preferred order of formation of MC carbides in superalloys is HfC, TaC, NbC, and TiC in order of deceasing stability [13-14]. These carbides are formed just below the temperature where solidification begins (during freezing) and appear either in coarse random cubic or as discrete particles heterogeneously distributed throughout the alloy matrix, both in intragranular and transgranular positions. They dissolve with difficulty in the solid phase during solution heat treatment and restrict grain growth when present on grain boundaries. During heat treatment and/or in service at a temperature range of 760 to 980^{o}C, these MC type carbides can slowly decompose and/or degenerate into lower carbides [27-28]. The reactions are as follows:

$$MC + \gamma \longrightarrow M_{23}C_6 + \gamma' \ (760\text{-}980^{o}C) \quad (2.6)$$

$$MC + \gamma \longrightarrow M_6C + \gamma' \ (815\text{-}980^{o}C) \quad (2.7)$$

Besides that, $M_{23}C_6$ and M_6C can also interact, forming one from the other as

$$M_6C + M' \rightleftharpoons M_{23}C_6 + M'' \quad (2.8)$$

$$\text{e.g,} \quad Mo_3(Ni,Co)_3C + Cr \rightleftharpoons Cr_2Mo_2C_6 + (Ni,Co,Mo) \quad (2.9)$$

$M_{23}C_6$ can also form from excess soluble carbon in the alloy matrix when cast ingot cools through its solvus range (1000^{o}C – 1050^{o}C). In $M_{23}C_6$ type carbide, the 'M' is usually Cr, but can be replaced by Fe and to a lesser extent by W, Mo or Co.

$M_{23}C_6$ has a complex cubic structure with preference to precipitate on grain boundaries. Discontinuous blocky or globular $M_{23}C_6$ carbide particles at grain boundaries are considered to be beneficial, in that they enhance ductility and creep resistance by

inhibiting grain boundary sliding, while cellular or continuous $M_{23}C_6$ grain boundary film could initiate premature failure by reducing ductility. It has been reported that MC-carbide decomposition in the range of 900^{o}C to 1000^{o}C could result in a continuous $M_{23}C_6$ grain boundary liquid film that deteriorates ductility at high temperatures [27]. The M_6C type of carbides is similar to $M_{23}C_6$ carbides; both have a complex cubic structure and tend to form when the Mo and W contents of the base alloy are high. Studies have shown that when Mo or W exceeds 6-8% in nickel-base alloys, M_6C together with $M_{23}C_6$ can precipitate along grain boundaries and the composition of these M_6C carbides can widely vary from M_3C to $M_{13}C$ [27]. During wrought alloy processing, M_6C carbides have been reported to be more efficient in grain size control, because they are more stable up to a higher temperature than $M_{23}C_6$ carbides [28].

In addition to carbides, borides can also form in superalloys owing to small addition of B. Such addition may subsequently result in the precipitation of boride particles during alloy casting or heat treatment. While M_3B_2 has been reported as a general type [29-30], Zang et al. [31] and Shidu et al. [32] have also reported M_5B_3 boride type in IN 738 and Rene 80 respectively under certain heat treatment conditions. Borides are hard refractory particles with a blocky or half-moon shape. When present on grain boundaries, they delay the onset of grain boundary tearing during creep and act as a supplier of B for grain boundary strengthening [27-28]. However, there has been no evidence of borides reported in Waspaloy, Rene 41 and the new Haynes alloy 282 even though these superalloys contain B in concentrations that range from 50-60 part per million (ppm) by weight.

2.3 Welding Processes

The technique of joining objects which comprise two or more simple and/or intricate parts by non-mechanical means is crucial during fabrication and repair of appliances, machines, automotives and aerospace components/assemblies. The history of joining dates back to around 3000 BC when copper-gold and lead-tin alloys were first soldered, and as early as 1000 BC, iron was welded into composite tools and weapons. With the advent of electricity towards the end of the nineteenth century, modern welding technologies became available, which led to a drastic revolution in welding processes. Figure 2-2 lists some of the chronological developments of welding processes. Welding can be classified into three broad categories, namely: brazing, solid-state joining and fusion welding. The fusion welding process is the principal and conventional joining technique of interest in this study and as such, will be discussed next.

2.3.1 Conventional Fusion Welding Process [34]

Traditionally, fusion welding has been employed to repair damaged or worn out component of turbine engines. Even so, many complicated turbine components made from casting, forging, wrought shapes or machined from solid pieces rely on welding for the completion of fabrication processes. Literarily, welding is a method of bringing two pieces of materials close enough to one another so that the atoms on their surfaces may mutually attract and bond the pieces; however, this would require perfect alignment of the crystal lattice with clean surfaces which rarely exists. In order to overcome this

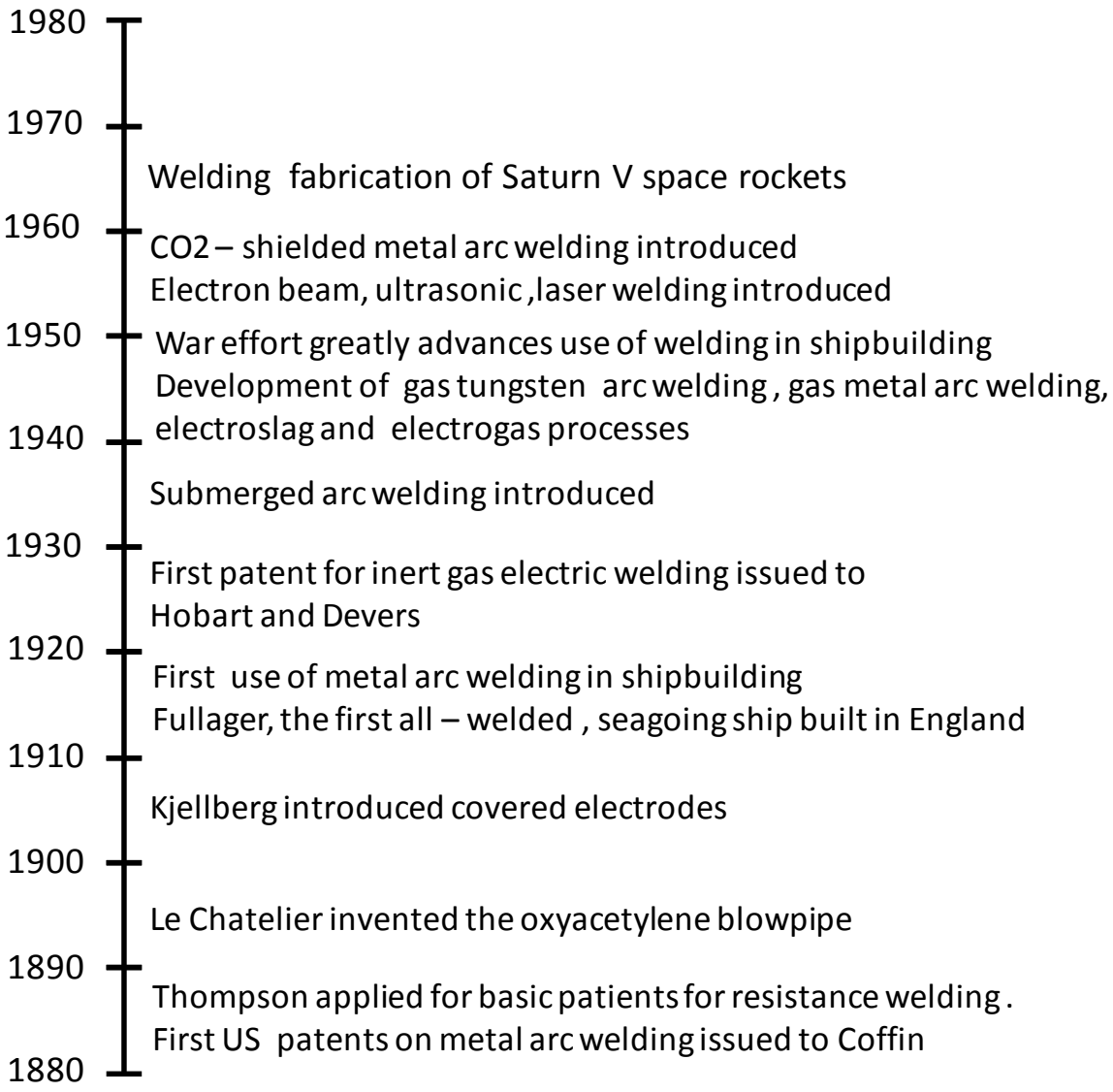

Figure 2-2: Chronological development of welding processes and their applications

Source: Encyclopedia of Materials Science and Engineering. Reprinted with permission from Elsevier (10th April, 2012) and the Author (27th March, 2012).

barrier, fusion welding process was developed as a joining process that involves the melting of two component surfaces to be joined by the use of a heat source, pressure, or both, with or without a filler alloy, which allows the mating surfaces to fuse together and solidify upon withdrawal of the heat source. In situations where a filler material is used, the filler could be of the same nominal composition as the base metal (provided that the joining is of components with the same composition) or as a composition compatible with the chemistry of the components being joined, both environmentally and mechanically. The heat source may vary from a chemical flame, to an arc, an electron beam, or a laser. Commonly used fusion welding processes are listed below based on their heat source. Two of the processes, namely, Arc Welding and Laser Beam Welding are discussed in this thesis.

1. Gas Welding – Oxyacetylene Welding (OAW)
2. Arc Welding – Shielded Metal arc Welding (SMAW), Gas Tungsten Arc Welding (GTAW), Plasma Arc Welding (PAW), Gas Metal Arc Welding (GMAW) and Submerged Arc Welding (SAW).
3. High Energy Beam Welding – Electron Beam Welding (EBW) and Laser Beam Welding (LBW).

2.3.2 Arc Welding

The arc welding process is the most commonly used of all the fusion welding processes and has been successfully used to weld most nickel base superalloys. The welding process involves the striking of an arc between an electrode and the workpiece, while the required temperature to melt and join the workpiece is attained during the

process. The heat generated by the arc melt the base metal or the base plus filler metal, producing a molten pool of metal that is protected by a slag or an inert gas blanket. Subsequently, the molten pool solidifies as the heat source is withdrawn from the molten area, forming a weld nugget referred to as fusion zone (FZ). The electrodes are either a consumable type (SMAW, GMAW, and SAW) or non consumable tungsten electrodes (GTAW, PAW). Of all the various arc welding processes, GTAW is the most widely used, especially where the joining of thin sheets is involved, and also because of its relatively low cost, simplicity and versatility.

A typical GTAW overall process and an enlarged weld area are schematically represented in Figure 2-3. The torch that holds the tungsten electrode is connected to a shielding gas cylinder along with a terminal of the power source. The workpiece is connected to the other terminal of the power source through a different cable. The shielding gas (Argon (Ar) or Helium (He)) goes through the torch body and is directed by a nozzle towards the weld pool to protect it from the air. Aside from its suitability to weld thin sections, GTAW usually produces clean, high-quality low-distortion welds and can be used to weld reactive metals, like, Al, Ti, Zr and Mg as well as to make autogenous butt joints. However, the deposition rate in GTAW is slow, and as such, a solid solution strengthened alloy filler is required when welding γ’ precipitation hardenable alloys and the use of a high strength filler is not encouraged because this leads to severe cracking. Also, in GTAW the HAZ size is large, and brittle tungsten inclusions are possible as a result of excessive welding current, which can cause melting of the electrode.

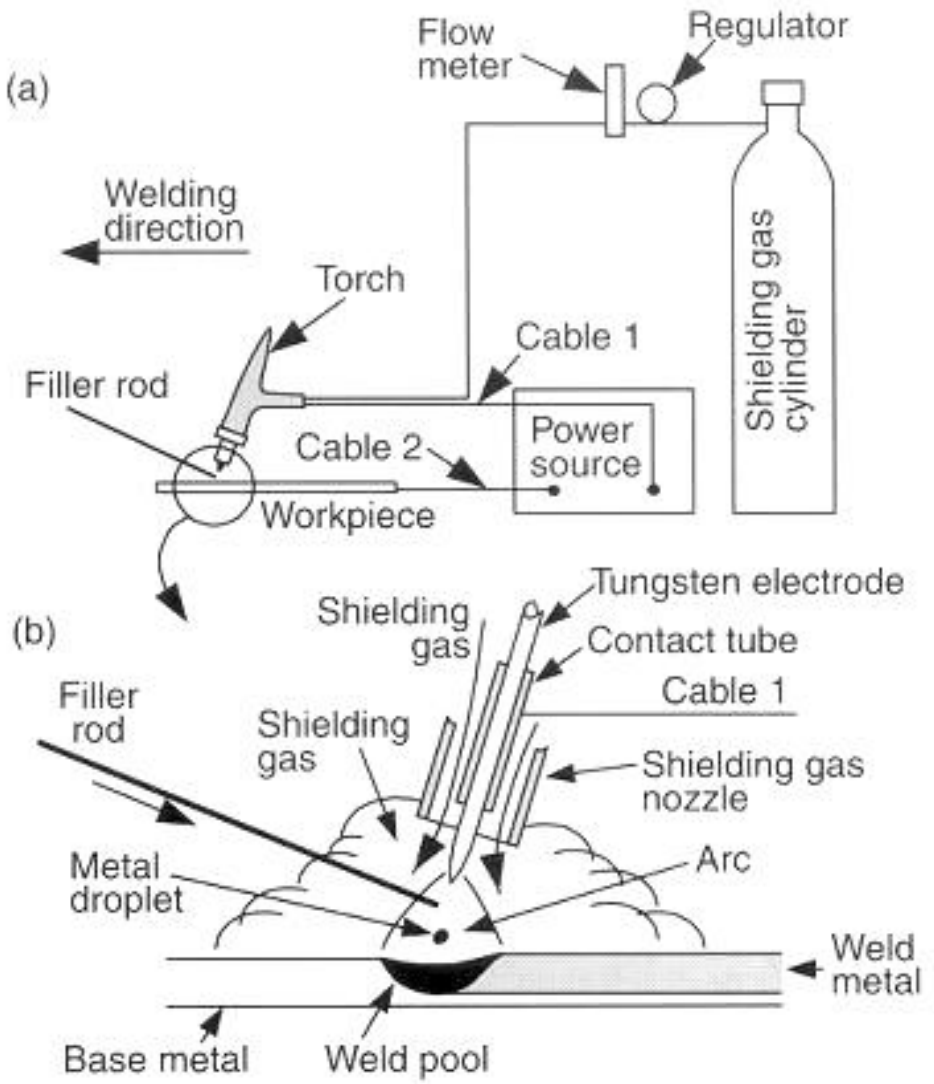

Figure 2-3: Gas tungsten Arc welding. a) Overall Process, b) Welding Area enlarged [34]

Source: "Welding Metallurgy" (2nd Ed) by Sindo Kuo . Reprinted with permission from the Global Rights Department, John Wiley & Sons, Inc. (28th October, 2011)

2.3.3 High Energy Beam Welding Process [34-35]

High energy beam welding processes were essentially developed to overcome the inherent high heat input limitations of OAW and arc welding processes, by providing processes with higher welding speed, deeper weld penetration, as well as better weld quality with low heat input and high solidification rates. Hence, these will result in less damage and/or impairment to the metallurgical and mechanical properties of the workpiece. EBW and LBW are two of the common high energy beam welding processes. A discussion on the LBW process is presented next.

2.3.4 Laser Beam Welding Process (LBW)

In the LBW process, the heat that melts and joins the metal surface is obtained from the application of a moving high density (10^5-10^7 W/cm^2) coherent optical energy source called laser. Laser is an acronym for "light amplification by stimulated emission of radiation". Owing to their coherent nature, laser beams can be focused and directed by optical elements, for example mirror or lenses, to a small spot in order to achieve high power density. Laser beams can be generated either by a solid-state laser or a gas laser. The schematics of the components of solid-state laser equipment and the laser energy emission process during laser production are shown in Figures 2-4a and b. In a solid-state laser, a single crystal is doped with a small concentration of transition elements or rare earth elements, for example in a yttrium-aluminum-garnet (YAG) laser, the YAG crystal is doped with neodymium. Upon exposure to high-intensity flash lamps, the electrons of the dopant element are selectively excited to higher energy levels, and lasing

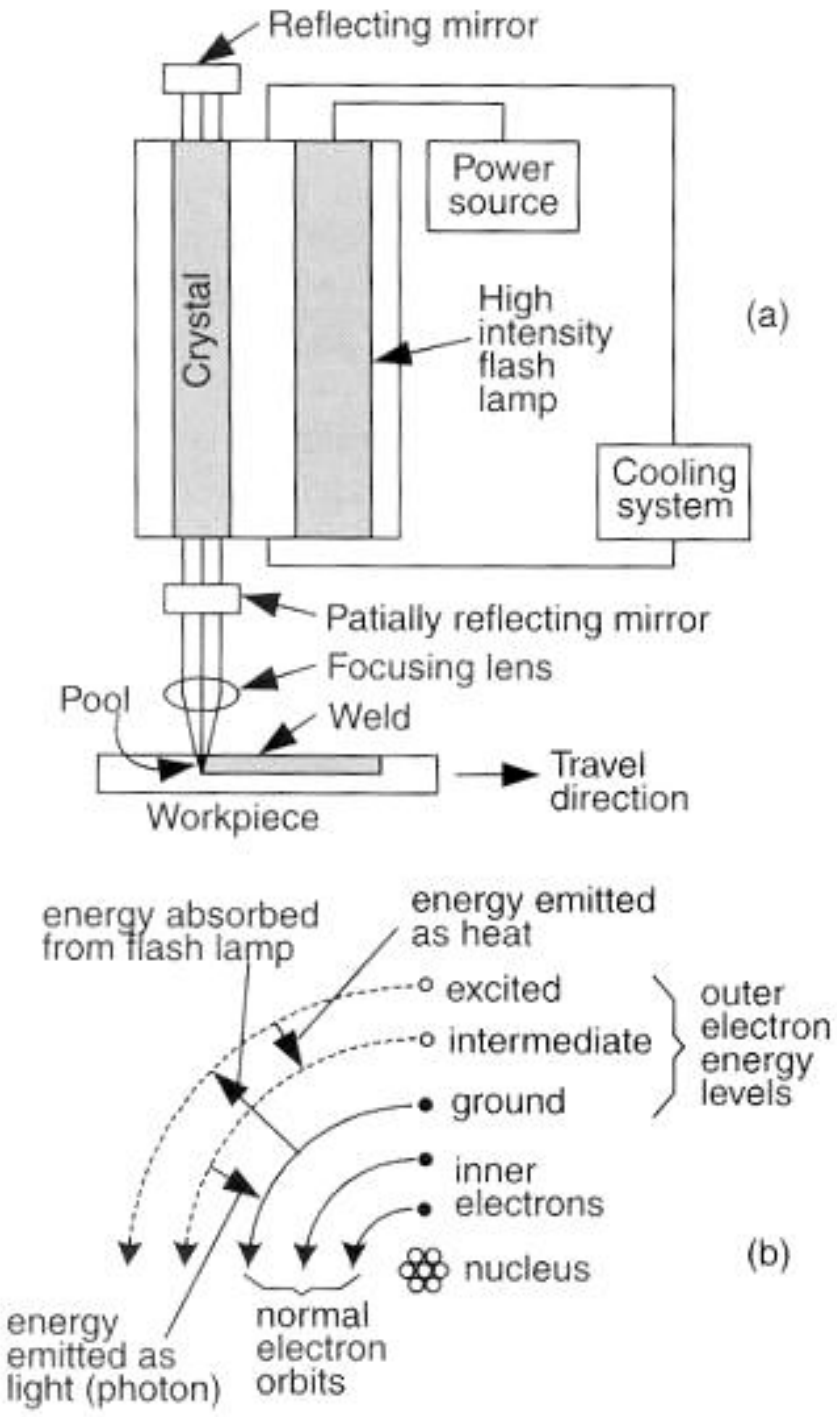

Figure 2-4: Solid-state laser beam welding: a) process, b) energy absorption and emission during laser beam welding [34]

Source: "Welding Metallurgy" (2nd Ed) by Sindo Kuo. Reprinted with permission from the Global Rights Department, John Wiley & Sons, Inc. (28th October, 2011)

(generation of laser beam) occurs when the excited electrons return to their normal energy state as shown in Figure 2-4b. In a CO_2 laser, a gas mixture of CO_2, nitrogen (N_2), and helium (He) is continuously excited by electrodes connected to the power supply and lases continuously. Apart from solid-state and gas laser techniques, semiconductor-based diode lasers (which have higher power and shorter wavelength) have also been developed.

The major advantages of the LBW process over conventional arc welding processes include: low heat input, producing deep penetrating weld with small HAZ size as well as reduction in physical distortion. Remote application is possible with the aid of fiber optics that can be used to transmit a coherent optical energy source. Unlike the EBW process, the LBW process does not require a vacuum or X-ray shielding devices, which in turn, reduces the running cost. However, optimization of the process parameters, such as beam energy, welding speed and laser focus point is important in order to achieve welds of high quality.

To protect the weld from oxidation (reaction with gases) and process instability due to plasma (ionization of metal vapor or shielding gases), shielding gas (He and/or Ar) are used. The shielding gases not only protect the molten metal from oxidation, they also minimize or prevent the influence of plasma from scattering or absorbing the laser beam and reducing the depth of penetration. Helium is often preferred over argon for high-power LBW because of its greater penetration depth, however, argon shielding has been found to improve penetration over pure He at high speed welding. Aside from cost, the ionization energy of He is higher than Ar, but lower than for air [34].

2.4 Welding Metallurgy [34, 36-38]

A weldment can be characterized by three major regions; namely, the FZ, HAZ surrounded by third region referred to as an unaffected base metal. In welds with filler, the FZ consists of a composite and an unmixed zone (Figure 2-5). It is usually the FZ that experiences a peak temperature that is well above the liquidus during weld thermal cycles, hence, within the FZ, complete melting and re-solidification of the parent metal occurs. In cases where filler is used, the weld pool dissolves some portion of the base metal (dilution). The solidification rate of the weld pool, as the heat source travels along the workpiece, varies from 10-10^3 K/s for conventional welding to 10^3-10^6 K/s for high energy beam welding processes. To some extent, a weld zone may be considered as a continuous casting; however, the high solidification rate in welds characteristically differs from near equilibrium cooling rates experienced during casting, which is typically less than $5^oC/s$.

In autogenous welding conditions, epitaxial solidification occurs; that is, the base metal acts as substrate on which the nucleation and growth of FZ solid phases occur by heterogeneous nucleation process. By this nucleation mechanism, a solid embryo of the weld metal freezes within a mould formed of the parent metal. Since the molten metal composition is identical to the parent metal, growth along a preferred orientation occurs as the heat of fusion is transferred to the base metal. The contact angle β between the solid phases formed and the metal substrate is influenced by the various surface energy acting. This can be further illustrated by using Equation (2.10) that has been derived for heterogeneous nucleation on a planar surface as shown in Figure 2-6,

$$\text{Cos } \beta = (\gamma ml - \gamma sm) / \gamma sl \quad \text{..... (2.10)}$$

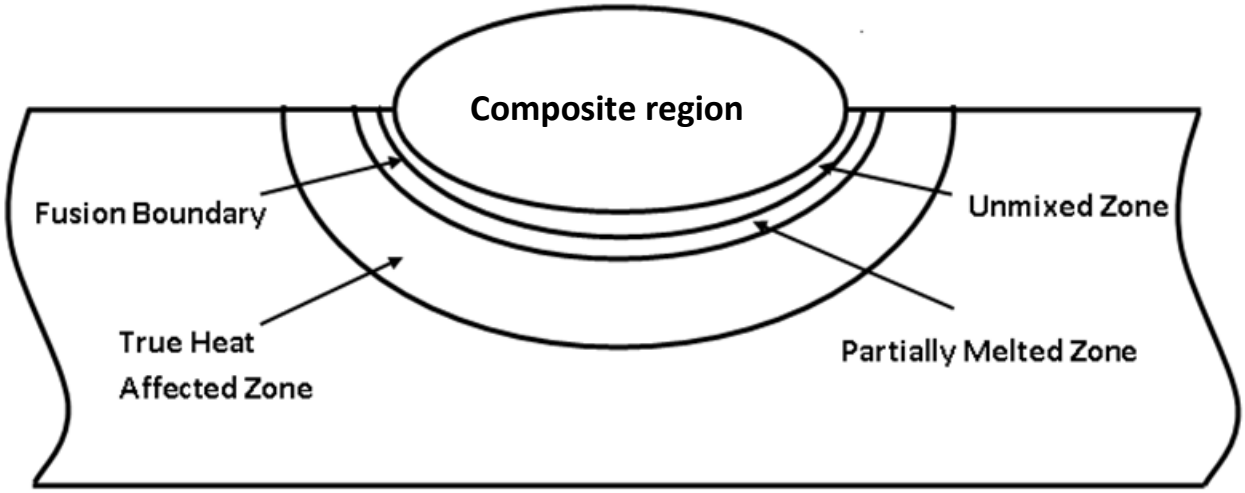

Figure 2-5: Different zones within a weld with filler

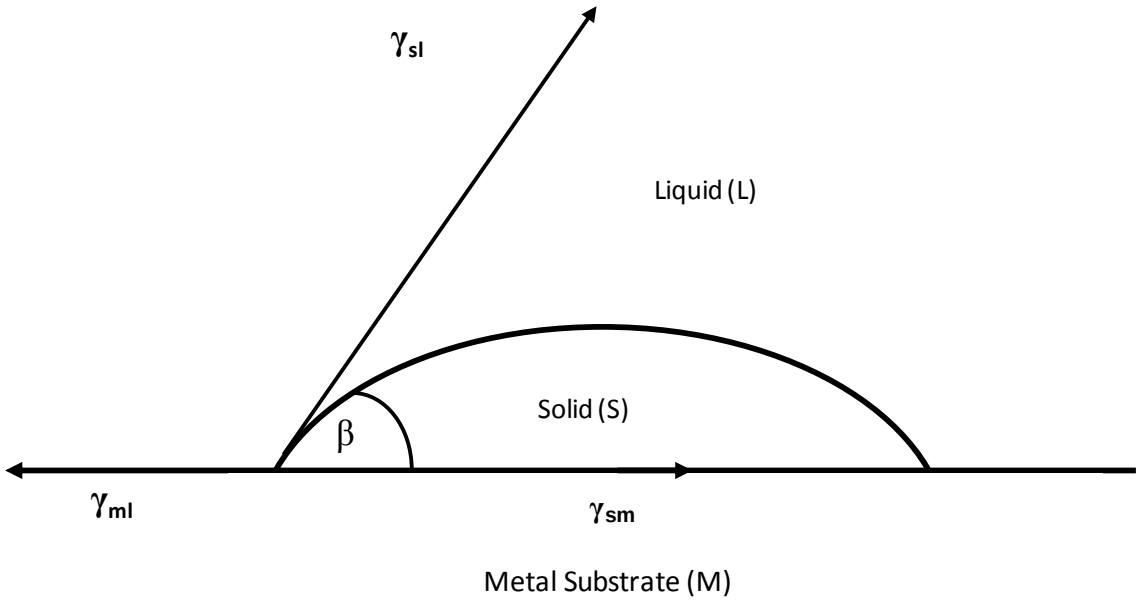

2 - 6: Surface forces present during heterogeneous nucleation of solid particle droplet on solid substrate

where γ_{ml}, γ_{sm}, and γ_{sl} are the interface energies for the metal/liquid, solid/metal and the solid/liquid interfaces, respectively. To a good approximation, $\gamma_{sm} = 0$ and $\gamma_{ml} = \gamma_{sl}$, thus, Cos $\beta = 1$ as $\beta = 0$ which causes spontaneous solidification, wherein no undercooling of the melt is required. In welds with filler, epitaxial growth may still occur but the classical heterogeneous nucleation process is most likely to dominate; i.e. the nucleation of new grains having varying crystallographic orientations with the parent metal in contact.

Surviving nuclei after solidification grows, and during this growth, the conditions in the immediate vicinity of the solid/liquid interface have a major influence on the microstructure of the FZ. As such, there can be various types of weld microstructural morphologies. In general, microstructural morphologies have been broadly categorized as planar, cellular and dendritic. In a planar solid/liquid interface, heat flow conditions are the rate controlling step and the direction of growth is perpendicular to the solidification front, that is, along the maximum thermal gradient (Figure 2-7a). Also, the thermal gradient in the weld pool is steeper at the region close to the fusion boundary than in the weld interior, because the degree of under-cooling in a solidifying melt is inversely proportional to the growth rate, G/R [38-39], where G is the thermal gradient and R is the cooling rate, which is higher when close to the fusion boundary.

Cellular growth is made up of many cells that grow relatively and uniformly parallel to one another. Similar to planar growth, the direction of the cell growth is also controlled by heat flow conditions (Figure 2-7b). Dendritic growth is however different, in that it is mainly controlled by growth crystallography considerations, that is, grains that have a preferred crystallographic axis which closely aligns with the heat flow directions survive while others that are not so well aligned are terminated (Figure 2-7c).

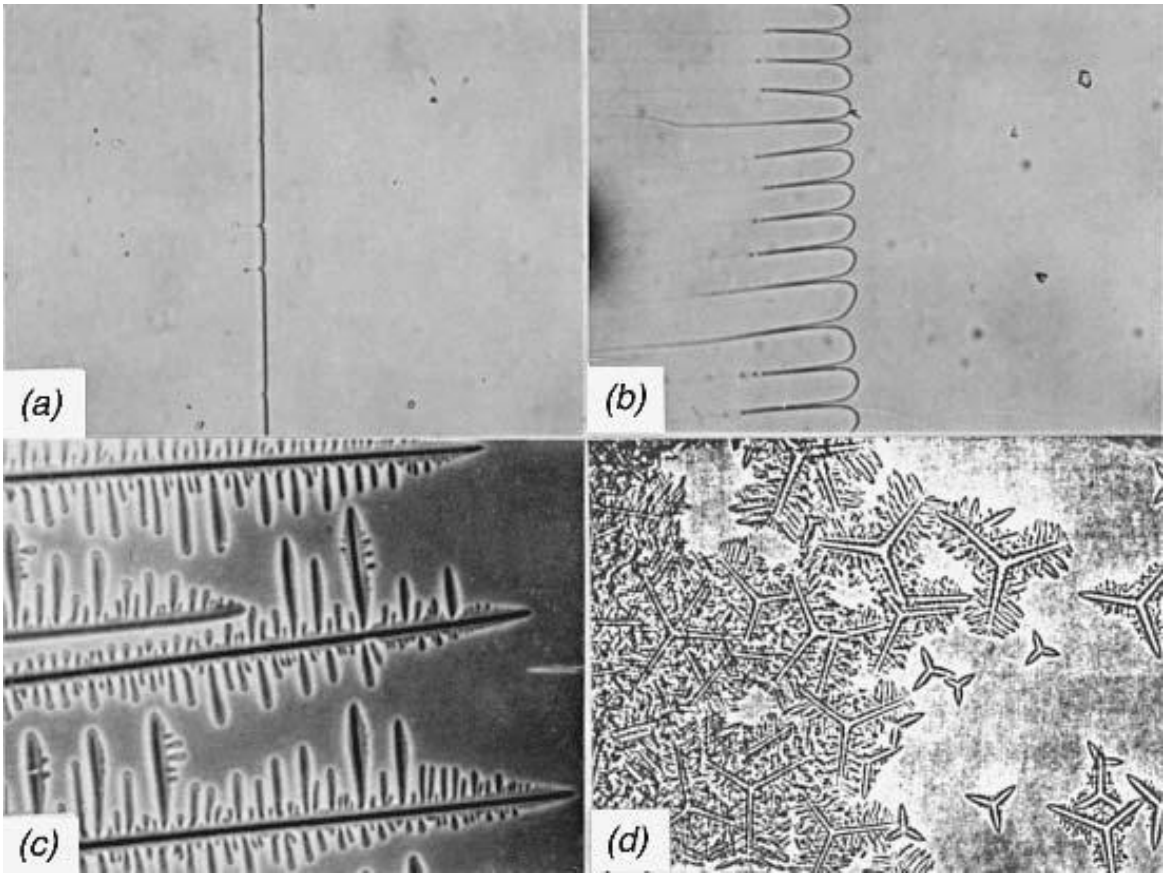

Figure 2-7: Basic Fusion Zone Solidification mode: a) Planar, b) Cellular, c) Dendritic, d) Equiaxed dendritic [34]

Source: "Welding Metallurgy" (2nd Ed) by Sindo Kuo. Reprinted with permission from the Global Rights Department, John Wiley & Sons, Inc. (28th October, 2011)

In cubic metal crystals, body-centered cubic (BCC) and FCC, the <100> directions is the preferred growth direction [34, 38], because the loose packing in this direction allows for a faster growth speed than in other closed packed directions.

There are two major types of dendritic growth, columnar and equiaxed dendritic growth. A packet of parallel dendrites along the same direction that combines to form a grain with a well-developed substructure is called columnar dendritic growth. Equiaxed dendritic growth (Figure 2.7d), on the other hand, is characterized by the growth of dendrites of different orientations in a liquid sufficiently cooled below the liquidus temperature, so as to ensure that spontaneous nucleation is possible. Each dendrite in equiaxed dendritic growth comprises separate grains in the final solidified structure, which are not necessarily parallel to each other. A combination of columnar and equiaxed grains may form in the weld zone; however, weld zone grains are either totally columnar or columnar near the fusion line and may change to an equiaxed structure near the centre, depending on the temperature gradient and growth rate or solidification rate. Grains perpendicular to the weld centerline are known to have poor tensile properties, while the formation of equiaxed grains is known to be desirable for optimum mechanical performance (tensile strength, ductility, and fracture toughness) as well as improved resistance to hot cracking [37].

The partially melted zone (PMZ) is the adjacent area immediately outside the weld metal where partial melting can occur during welding (Figure 2-5). The PMZ in association with the true HAZ (a portion where only solid state microstructural changes occur during welding) forms the entire HAZ area. In the HAZ, the peak temperature experienced during the weld thermal cycle lies between the liquidus and effective solidus

of the parent metal. The effective solidus is, however, always below the equilibrium solidus of an alloy because of localized segregation.

2.5 Elemental Solute Partitioning during Welding

Solute redistribution or partitioning of alloying elements into a solid or liquid phase, relative to the nominal solute concentrations during melt solidification, is an important phenomenon that has a major influence on the weld microstructure and weldability of superalloys. On a fine scale in the order of dendrite arm spacing, this is referred to as microsegregation whereas on a larger scale, it is known as macrosegregation. The relationship between hot cracking and elemental solute enrichment during weld solidification has been attributed to its effect [40] on the extension of the freezing temperature range, which causes solute segregation and non-planar solidification.

Although several models have been developed to explain solute partitioning and the resultant segregations that exist in solidified microstructures, the models are generally based on many assumptions [41- 46], that include:

I. that the solidification rate is rapid enough that there is no change in solid composition once it is formed.
II. that diffusion in the liquid results in a compositional gradient adjacent to the solid-liquid interface.

III. that mechanical mixing is possible in the liquid but not in the boundary layer adjacent to the solidifying interface where the diffusion produced compositional gradient exists; and

IV. at the solid/liquid interface, the composition of the solidifying metal and the adjacent liquid are the equilibrium composition prescribed by the phase diagram.

For the purpose of illustration, the solute segregation for an alloy of composition Co is explained by using Figure 2-8. Solidification starts at temperature T_1, which in magnitude is just below the liquidus temperature (T_m), wherein a solid of composition $C_s = kC_o$ is formed. k is the equilibrium partition coefficient, defined as the ratio of the solid to liquid composition at the solid/liquid interface during solidification. When $k < 1$, the solid (C_s) contains a lower concentration of the solute element than the bulk liquid and the excess solute is rejected into the liquid, raising the amount of solute in front of the solid/liquid interface.

Under equilibrium condition at the liquid/solid interface, the extra solute is mixed throughout the liquid, which slightly raises the liquid solute content. When the alloy is further cooled from T_1 to T_2, equilibrium conditions at the interface dictate that the solid has a composition Cs_2, which rejects more solute into the liquid and this will continue until the solid/liquid interface reaches T_3, where the solid formed has a composition Co and the adjacent liquid has a composition C_{L3} = Co/k. Here a steady state is attained and the amount of solute rejected is the amount required to raise the composition of the liquid at the solid/liquid interface to a composition Co/k, thus maintaining the shape of the composition gradient in the liquid just next to the solid/liquid interface. For an isomorphous system, where only a single type of crystal structure exists over all the

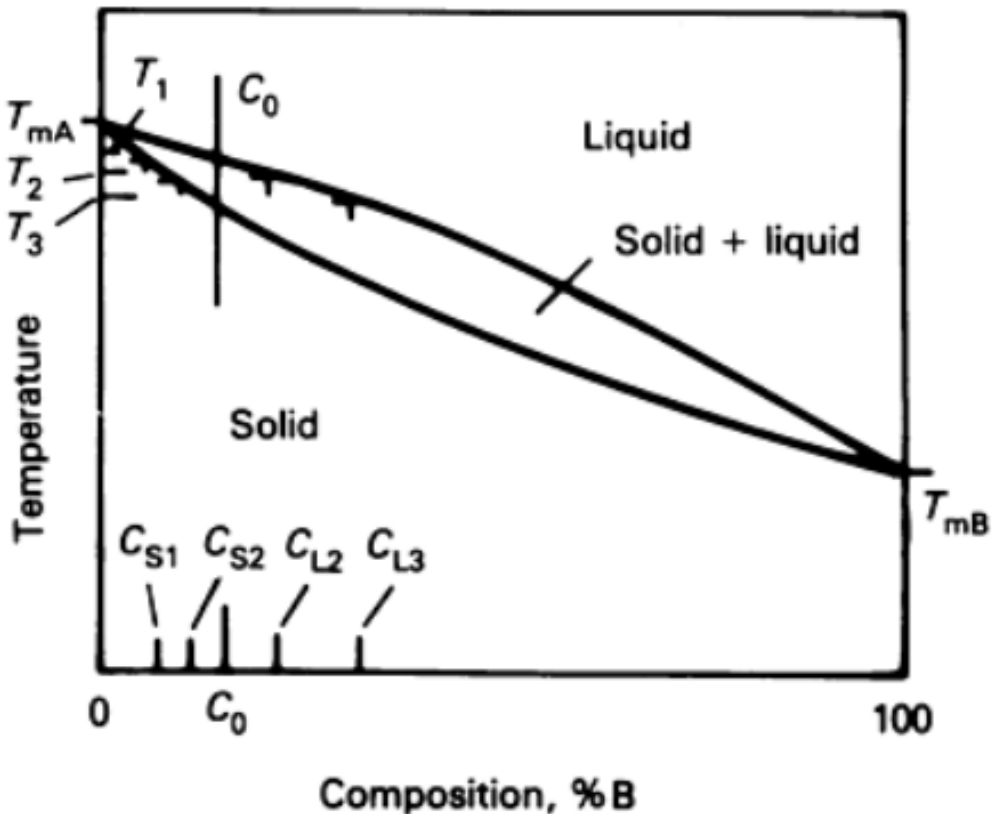

Figure 2-8: Phase diagram showing the compositions of the solid and liquid at four temperatures [40]

Source: "Treatise on Materials Science and Technology: Embrittlement of Engineering Alloys" by H. D. Solomon. Reprinted with permission from the Elsevier (1st May, 2012)

composition range, the final solid is the pure solute. However, for an eutectic system, the liquidus and the solidus meet at the eutectic composition and the final solid is eutectic. Under non-equilibrium conditions, such as during rapid solidification which is common during welding processes, the solid and the liquid at the solid/liquid interface are not at equilibrium and the excess solute in the liquid is not completely mixed because of the limited diffusion that takes place, which invariably results in the compositional gradient extending into the liquid from the solid/liquid interface. Several model exist that allow for non-equilibrium partition coefficient, k', and its variation with solidification velocity [47]. These models allow the partition coefficient to vary between the equilibrium value associated with the phase diagram at low growth velocities and a value of 1 at extremely high growth rates. When $k' = 1$, the solid that forms has the same composition as that of the liquid and is referred to as partitionless solidification. An important consequence of the non-equilibrium partitioning is that at high solidification rates, less solute redistribution occurs in a solidified structure which forms a more uniform composition. In this extreme case where less solute partitioning occurs, the appearance of normally occurring second phases may be avoided. These effects can be expected during rapid solidification of high energy density processes such as LBW and EBW.

In addition, a variety of non-equilibrium phases may be produced as a result of rapid solidification. These phases may be present in other compositions as equilibrium phases, with their range of stability simply extended. They may as well be new phases not normally found in the appropriate phase diagram of the alloy. More importantly, high cooling rates may have an indirect effect on the phases that form in the welded microstructure, even if solidification behaviour is not significantly affected. In some alloy

systems, the as-solidified phases are not stable at low temperatures and as such undergo a solid-state transformation during cooling. If solid state cooling is sufficiently fast, this transformation may be inhibited or altered in the case of diffusion controlled reactions. Alternatively, the nature of the transformation may be altered if sufficient time for diffusion is not available. Segregation during weld pool solidification may also lead to the occurrence of weld defects and/or variations in properties throughout the FZ.

2.6 Welding Defects [34, 38]

Welding defects are imperfections in the form of discontinuities, flaws, interruptions and/or ruptures that are present on the surface or internal structure of welds and as such, degrade the performance and integrity of weldments. The defects can originate either from processes, designs or metallurgical related problems. Figure 2-9a-e shows some typical weld defects common in welded alloys. Typical defects like porosity, lack of fusion, undercut, shrinkage voids, crater cracking, slag inclusion and lack of penetration are process or procedure related defects, while defects, such as high-low conditions, are design errors that arise from the misalignment of workpieces that are being welded or when the workpieces have unequal thickness. Crack and microfissuring (microscopic in size) are metallurgical related defects that are occasioned owing to high stress/strain generation during welding in combination with inherent material properties. Cracks in welds can be classified into two main categories, that is, those that can be attributed to the welding process itself and those that occur during service. Cracks that occur in the HAZ and FZ during solidification from weld thermal cycle or when a weldment is re-heated are termed ‘hot cracking’. Some common types of hot cracking are

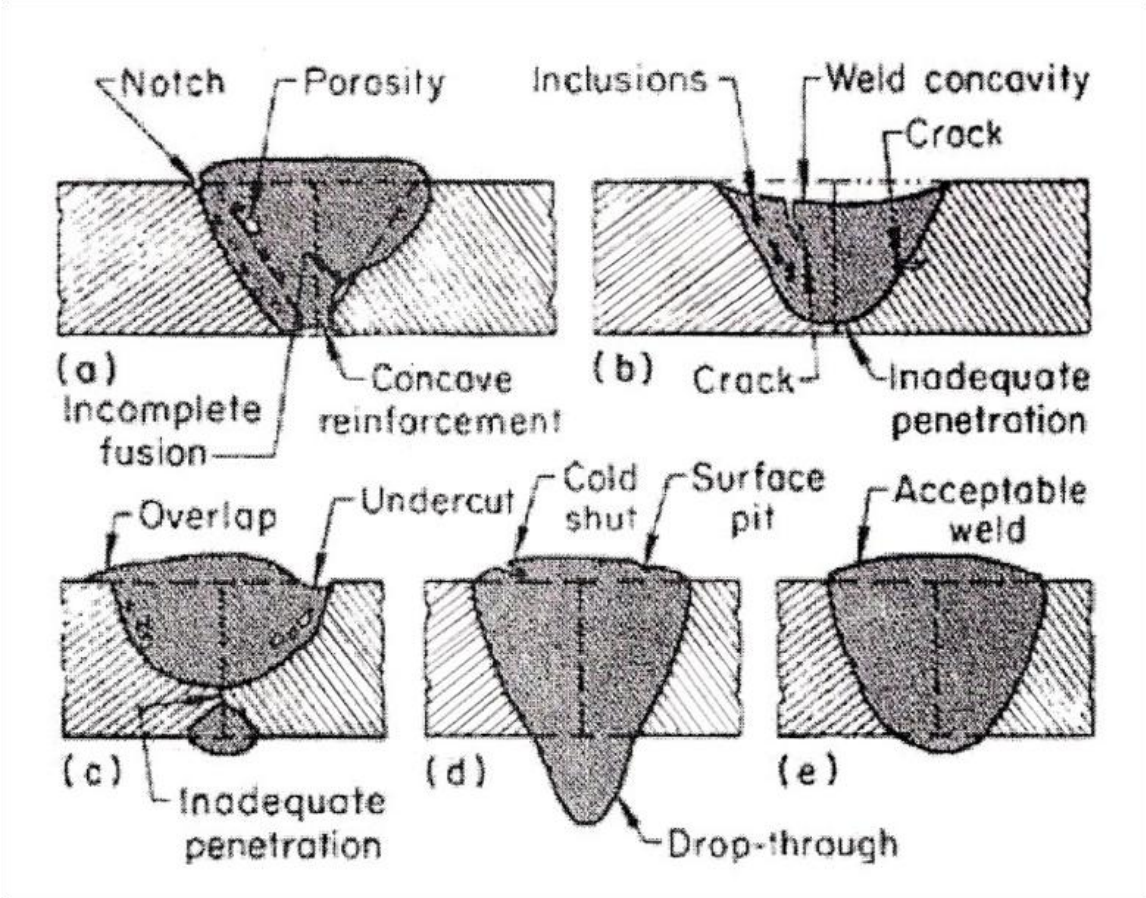

Figure 2-9: Typical Weld defects [7]

Source: "ASM Technical Guide 1998" by M.B. Bever. Reprinted with permission from the ASM (18th April, 2012)

listed below while those that are of interest to the present study are further reviewed based on their governing theories.

1. Solidification cracking – occurs mainly in the FZ.
2. Liquation cracking – occurs in the HAZ
3. Post weld heat treatment cracking – occurs in the FZ and HAZ
4. Cold cracking – occurs in the HAZ
5. Lamellar tearing – occurs in the HAZ close to FZ.

2.6.1 Solidification Cracking [34]

Solidification cracking in weldments is confined to the FZ, intergranular in nature and often reveals the dendritic morphology of the solidifying weld metal. The cracks are the result of the inability of partially solidified weld materials to accommodate thermally induced contraction stresses that developed during weld cooling and solidification [48]. The loss in ductility has been principally attributed to mechanical (stresses and strains) and metallurgical factors (presence of low melting point constituents that form as a result of segregation during liquid to solid phase transformation) [49]. The stresses and strains are inevitable; they result from solidification shrinkage of weld liquid and/or thermal expansion and contraction of FZ and HAZ. The effect of solidification shrinkage can be further aggravated where it is accompanied with rapid precipitation of second phase particles that have significant disregistry with the matrix.

Segregation induced metallurgical effects, however, occur due to the partitioning of elements during the initial stages of solidification, the amount/magnitude of which

depends on the partitioning coefficient *k*. The partitioning coefficient '*k'* is defined as the ratio of concentration of solute in solid to that in liquid in equilibrium with it [34]. Alloying elements with the smallest value of *k* have the greatest tendency to segregate to the solidifying liquid. As such, alloying/ trace elements like S, O, B, P, C, Ti, N and H in complex austenitic matrix of high temperature alloys with *k* values less than unity have the tendency to segregate into solidifying liquid where they form low melting phases and eutectics with the metal to produce wetting films at grain boundaries. The presence and persistence of the wetting films at grain boundaries at a time the weld is partially solidified reduces the surface to surface contact strength of the grain boundaries, and as such, lower the ductility of the metal. If and when the magnitude of contraction stresses generated in this period exceeds the rupture strength of the grain boundaries or cohesive strength of the grain, a rift (cracks) will occur. The extent/magnitude of cracking has been reported to be further influenced by many other related factors such as:

1. Solidification temperature range: A wider solidification temperature range means a larger area that is weak and susceptible to weld - solidification cracking. Alloys with positively partition elements ($k < 1$) will widen the region of weakness and raise the susceptibility to solidification cracking.

2. Amount and distribution of liquid during the terminal stage of solidification: Cracking susceptibility has been correlated with amount and distribution of liquid on grain boundaries in some alloy systems [34, 49-52]. Increases or decreases in susceptibility to cracking were found to correlate with solute content which determines the amount of terminal liquid. However, in pure metals, solidification

cracking was reportedly precluded owing to the absence of low melting point eutectics at the grain boundaries. In between these two scenarios, the volume of eutectic liquid in-between grains during the weld thermal cycle could be just adequate enough to form a thin continuous grain boundary film that makes the metal highly susceptible to cracking and without extra liquid for healing the cracks. The liquid must also wet and spread out over the grain boundary in a continuous or semi-continuous fashion to induce cracking. Liquid that exists in a localized pocket will improve resistance to cracking by increasing the fraction of the solid-solid contact area in-between the grains.

3. Grain structure of the weld metal: Weld metal with fine equiaxed grains were often found to be less susceptible to solidification cracking than those with coarse columnar grains. This was attributed to the improved ductility and ability of fine equiaxed grains to deform much more easily in order to accommodate contraction strains [53]. In addition, the grain boundary surface area is larger in fine equiaxed grain materials and as such, segregates of low melting point are less concentrated (or more evenly distributed for the same amount of segregant) in the grain boundaries. Consequently, weld-metals with coarse grain sizes would have a thicker liquid layer compared to the fine equiaxed grain structures if the same volume of liquid is present in both due to a reduction in available grain boundary area. Besides that, liquid feeding and healing of incipient cracks, where possible, can also be more effective with fine equiaxed grains [34].

4. Magnitude of contraction stresses: Two widely accepted pre-determined conditions for solidification cracking to occur are the concurrent presence of stresses/strains and a susceptible microstructure. Where the magnitude of stresses/strains (dependent on heat input parameters and constraint) that act on adjoining grains during solidification is negligible or completely absent, total crack length (TCL) and cracking tendency have been minimized or eliminated even under certain conditions where extensive liquation occurs [54-55].

5. Degree of restraint: Improper design of weld joints can lead to high degree of restraint and subsequently aid in solidification cracking [48]. The use of jigs and fixtures with good fit-up is recommended to reduce/eliminate weld restraint in addition to proper selection of the minimum allowable weld joint gap.

2.6.1.1 Solidification Cracking Theories [50, 56 - 58]

Many theories have been proposed to explain the formation of solidification cracks, among those, most notable are the shrinkage-brittleness and strain theories and Borland's generalized theory of hot cracking. The underlying concepts of these three theories are further reviewed below.

2.6.1.1.1 Shrinkage-Brittleness Theory (S.B.T)

The theory originated from the pioneering work of Vero [56], Singer et al. [50, 57] and Pumphrey et al. [58] on hot tearing/ cracking of aluminum alloys. The ideas

developed by them were found to be equally applicable to other alloy systems. Accordingly, the mechanism of cracking is attributed to the exhaustion of the ductility of a solid-liquid mass within a temperature interval, called the brittle temperature range (BTR), where solid-solid bridges have been established. The upper temperature limit of the BTR is referred to as the coherent temperature while the lower limit is called the solidus temperature. In their view, cracks are unlikely to form below the solidus temperature because it is assumed that solid-metal is ductile at subsolidus temperature. As such, cracking is only possible when it involves breaking of solid-solid bridges within a range of temperature between the coherent temperature and solidus.

In observing the illustrations in Figure 2-10, it is obvious that the BTR of an alloy as defined above lies within its solidification temperature range, in that, its covers the region from the solidus temperature point where the solid first appears, down to the lowest temperature at which liquid exist. In essence, the extent of this BTR can be greatly influenced by the alloy composition or any other factor that can modify the freezing range, such as the mode of liquid distribution. The mode of liquid phase distribution as well as the temperature gradient within the cooling mass has been reported [58] to influence the shape of dendrites (whether slender or thick) and the temperature at which the coherent network of solid forms during solidification. In the summaries of their work based on experimental observations [58], the influence of eutectics on shrinkage brittleness has been clarified. It was affirmed that during the solidification of an alloy, coherency is gained when the amount of interdendritic liquid (liquid fractions between the dendrites and not liquid entrapped within the arms of a single dendrite) falls below approximately 5%. An eutectic alloy which contains 5% or more of interdendritic liquid

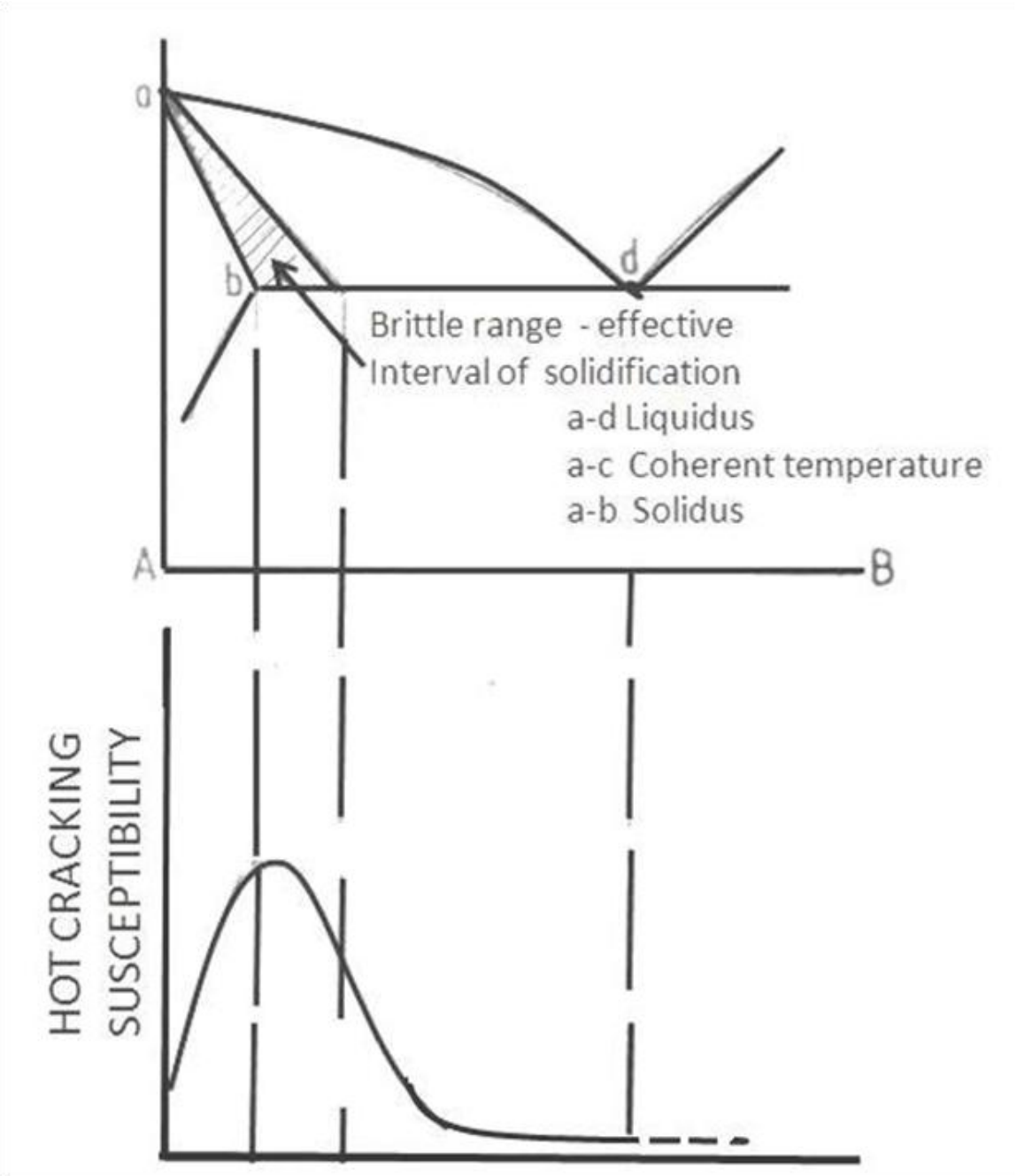

2-10: Hot cracking susceptibility of eutectiferous alloy [49].

Source: "British Welding Journal" by J.C. Borland. Reproduced courtesy of TWI Ltd (22nd May, 2012)

will not gain coherence until the eutectic temperature is reached and consequently will possess no brittle range. This is confirmed by the fact that aluminum binary and tertiary alloys show no tendency to cracking when the total alloy content exceeds a certain level [50, 52, 56].

The concept of "healing" was introduced by Vero [56] whereby incipient cracks, formed as a result of shrinkage brittleness, are considered to be filled with liquid and their harmful effects consequently subdued. Vero [56] postulated that if a solidifying metal contains more than a critical volume of eutectic, any cracks formed by the contraction of the primary crystal would be healed by the inflow of eutectic liquid. The concept of 'accommodation', which is an act to prevent cracking when an alloy is cooling through the BTR was first proposed by Singer and Cottrell [59] without a clear distinction from the concept of 'healing', but later, Pumphrey [58] distinguished it from the concept. Accommodation was defined as the degree to which an alloy is able to withstand shrinkage strain by movement of the crystal within the semi-solid mass. It was argued that in welds and small castings, accommodation is more likely to occur than healing, because for healing to occur, a critical volume fraction of liquid is necessary, which may not be present in these cases. Cracks are expected to occur when accommodation has proceeded as far as possible, but the crack may however be healed by a flow of liquid into it when there is a high proportion of liquid present or a particular ready supply from another part of the mass is possible.

The various ideas generated were further expanded by Medovar [60], who stated that the variation of hot cracking with alloying additions, for elements which form continuous solid solutions, is determined by the length of the freezing range. If alloying

elements are mutually soluble in either the liquid or solid state, then hot cracking should not occur, because the freezing temperature range will be very narrow. For systems that form primary solid solutions, even a very small addition of the second element will cause severe cracking, owing to the rapid increase in the freezing range, whilst further additions of the second element should tend to reduce cracking.

2.6.1.1.2 Strain Theory [61]

The strain theory was proposed by Pellini and colleagues [61] based on previous research on hot tearing in casting. The thrust of their proposition affirms that cracking is caused by localized strain that originates from thermal gradients developed during alloy solidification. That is, strain tends to tear apart solid masses of partially solidified materials separated by essentially continuous thin film of liquid. The major assumptions of the theory is that HAZ cracking results from the liquation of grain boundary segregates, which are present in the region that borders the fusion line of the weld. Also, hot cracking does not occur in the 'mushy' stage of solidification because shrinkage strains are more uniformly distributed among wide interdendritic liquid and stress relaxation by flow of the pasty mass is possible [58].

In essence, cracks will only develop when the liquid film stage is reached, solid-solid bridges have not been established and localized strains are exceedingly high. The importance of this concept is further appreciated by considering certain conditions where alloys passes through the solidification temperature range and develop an essentially continuous liquid film near their solidus irrespective of whether the process entails

heating or cooling. This stage is recognized as the liquid film stage, and therefore, the strength and ductility of a mass of solid grain separated by liquid films will be of extremely low order. As such, the time-temperature interval in which the liquid exist becomes very critical in determining the hot tearing/cracking stage. Segregation of minor alloying elements (S, P, and B) on the grain boundaries can locally depress the melting point or if the boundaries contain a continuous network of low-melting segregated material, the liquid will form below the bulk solidus of the alloy at the melting point/solidus temperature of the segregate. However, if the segregation is not continuous or uniform on the grain boundaries or the composition of the alloy approaches that of pure metal, the effectiveness of the liquid film is reduced and may persist only for few seconds unlike the scenario where the segregates are continuous and saturate the grain boundaries which allow the film stage to last several seconds or minutes.

The significance of the liquid film stage is that separation can still occur through the liquid film at some intermediate temperature range between the melting point of the segregated materials and the bulk solidus temperature depending on the amount and distribution of the film as schematically represented in Figure 2-11. The crack formation sequence is further explained by using the illustrations in Figure 2-12, which combine hot cracking of welds and HAZ. As the welding torch passes any location along the workpiece, liquid pool formed behind the torch passes the segregate region and melting occurs between the grains. Also, the segregate films on the grain boundaries melt across the region where the temperature rises to the solidus temperature of the segregate film, causing separation of the adjacent grains. The lateral distance from the fusion line to which melting occurs is determined by the thermal gradient perpendicular to the weld and

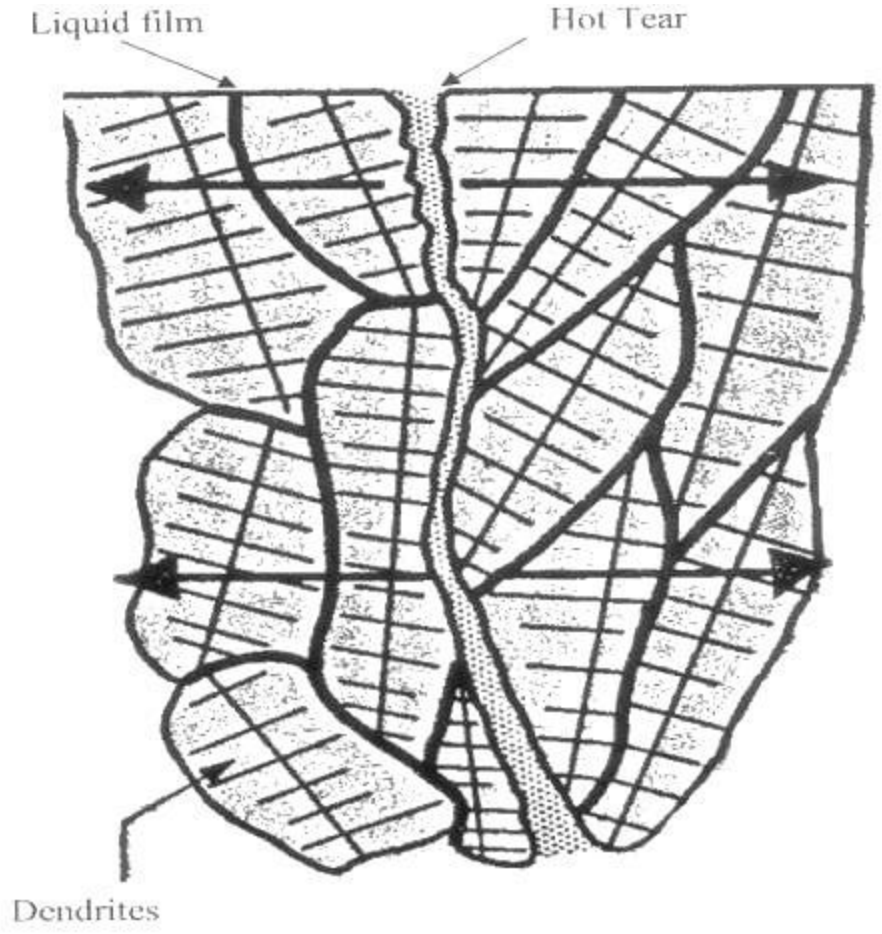

Figure 2-11: Hot cracking in castings by fracture through interdendritic liquid film existing near the solidus temperature [61]

Source: "Foundry" by W. S. Pellini. Reprinted with permission from the Penton Media Inc. (20th April, 2012)

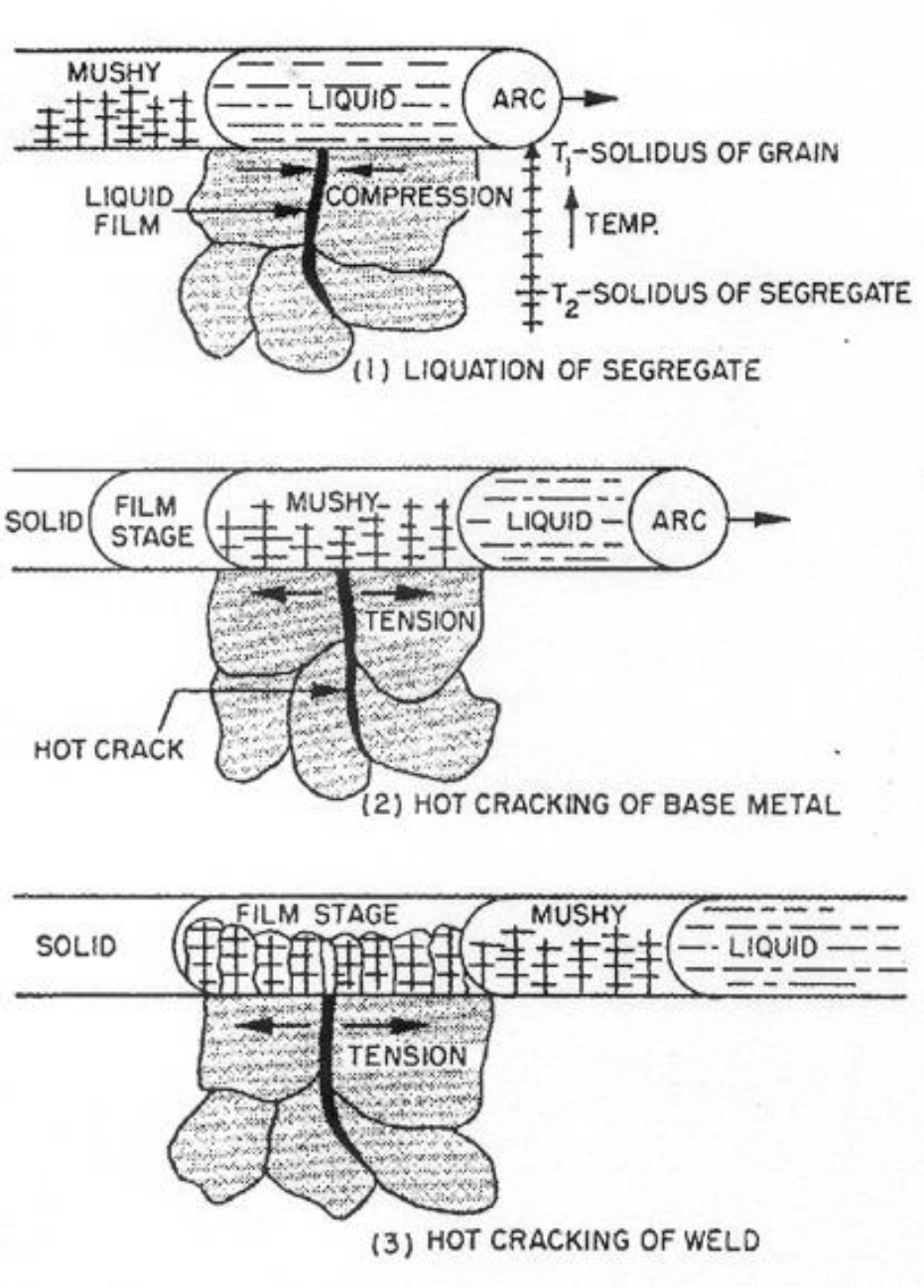

Figure 2-12: Schematic illustration of weld hot cracking process: a) liquation of segregates, b) hot cracking of base metal, c) hot cracking of weld [61]

Source: "Foundry" by W. S. Pellini. Reprinted with permission from the Penton Media Inc. (20th April, 2012)

as such influenced by heat input. At this stage the HAZ is put into a state of compression due to the thermal expansion of hot metal near the fusion line and the grain boundaries do not crack. As the torch moves on, cooling takes place, which results in the separation of the intergranular film region (fissures) because of tensile stresses that had developed in the HAZ as the HAZ contracted. At this stage, the weld metal is in a mushy condition and hot tearing (crack) will not be possible. However, as cooling continues, the weld metal reaches the liquid film stage and there is the development of strain concentration (notch-like-effect) in the HAZ crack position which leads to hot tears (cracks) in the weld. That is, the shrinkage strain generated by the cooling of the weld metal is concentrated at the HAZ crack point with consequential hot tearing in the weld metal which can also be described as continuation of the HAZ hot crack.

The theory further justifies why liquid film formed from segregant is much more effective in causing failure than that developed at the true solidus during solidification of an alloy. According to the theory, while liquid film provides a metallurgical condition that permits hot tearing, the actual occurrence of hot tearing is determined by the mechanical factors inherent in the rate of extension per unit time imposed in the short time before the liquid film solidifies. In essence, under non segregated or near pure metal conditions, the metal passes through the liquid film stage in a very short period of time which is comparable to a few seconds. However, under segregated species conditions the liquid film stage exists for a much longer period of time. As such, the rates of extension which did not develop sufficient separation of the film to cause fractures in the time of a few seconds may be fully effective in the time of several minutes. In summary, Pellini's strain theory attributes solidification cracking to the rifting apart of a solid-liquid mass in

a region where solid-solid bridges have not been established and the formation of solid-solid bonds will prevent cracking contrary to the concepts of the S.B.T.

2.6.1.1.3 Generalized Theory [49]

A generalized theory of solidification cracking was proposed by Borland in 1960 which incorporated some of the relevant aspects of shrinkage-brittleness and strain theories. In addition, the significance of wetting angles and how they influences interphase /grain boundary energies and the effect of solute addition were introduced. The theory sought to clarify the contention whether cracking normally takes place during the stage in which continuous films exist or during a period when some solid-solid bridging has occurred. To do this, Borland divided the solidification sequence of a molten alloy into four stages as shown in Figure 2-13 and described below:

Stage 1 – Primary dendrite formation. In this stage, the solid phase is dispersed while the liquid phase is continuous; both liquid and solid phases are capable of relative movement.

Stage 2 – Dendrite interlocking. Here, both liquid and solid phases are continuous, but only the liquid phase is capable of relative movement and able to freely move within the interlocking dendrites.

Stage 3 – Grain boundaries development. The solid crystals are in advanced stage of development and the semi-continuous network restricts the free passage of liquid. Relative movement of the two phases is difficult.

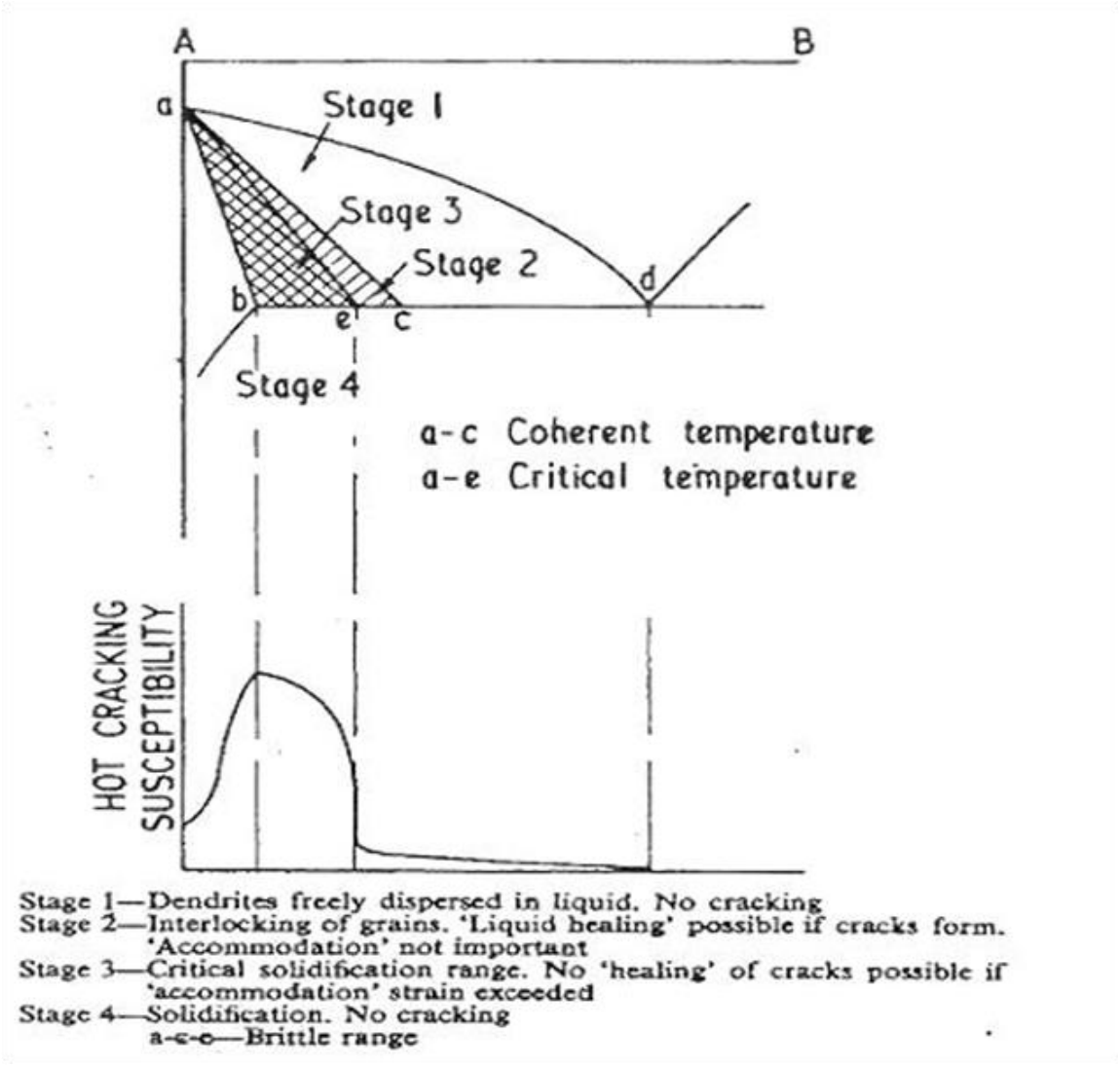

Figure 2-13: Schematic illustration of effect of constitutional features on cracking susceptibility in binary systems [49].

Source: "British Welding Journal" by J.C. Borland. Reproduced courtesy of TWI Ltd (22nd May, 2012)

Stage 4 – Solidification. The remaining liquid solidifies.

From this analogy, Borland believed that materials are susceptible to cracking in stage 2 once they have cooled to or below the coherent temperature, but only under non-equilibrium conditions, such as those experienced during welding, where the effective solidus is reduced due to the segregation of solute elements with partition coefficient $k < 1$. More so, he agreed with the strain theory as well, in that if a crack is initiated in stage 2, it is possible that it will be healed by the flow of liquid into the fissures formed, provided that a high volume of liquid is available. Stage 3 in the freezing sequence was identified as the 'critical solidification range' (CSR) and its commencement temperature is referred to as the critical temperature *Tc*. Here, the formations of grains or solid crystal have reached the advanced stage of solidification and the relative movement of liquid and solid is constrained; therefore, crack healing will be impossible if initiated.

The driving force for cracks is believed to be the result of the build-up of high stresses between grains or in the absence of significant constraint, a parting of the liquid phase that occurs as a result of the development of highly localized strains. Where the liquid phase covers almost all the grain faces during freezing (over a relatively wide temperature interval), high stresses will develop on narrow bridges that join adjacent grains, in contrast to when the liquid phase is confined to grain edges and corners. In essence, the generalized theory affirms that the existence of a wide freezing/solidification range, although necessary, is not a sufficient condition for cracking to occur, and that the alloy must not only pass through the solid-liquid stage, but the liquid must also be present in a form that allows the development of high stresses between grains. Furthermore, the

theory relates the dependency of liquid distribution along grain boundaries to the free energies of the grain boundaries (γ_{ss}) and solid-liquid interphase energy (γ_{sl}), which is related to the liquid - grain boundary dihedral angle θ as given by the expression:

$$\frac{\gamma_{sl}}{\gamma_{ss}} = \tau = \frac{1}{2Cos\left(\frac{\theta}{2}\right)} \text{ ---------- (2.12)}$$

At $\tau = 0.5$ ($\theta = 0$), there will be complete wetting, as the liquid remains at the grain faces as almost continuous films that prevent quick joining. If this condition exists over a relatively large temperature interval, which is the case for most highly alloyed materials, it will allow stresses to locally build up to a critical amount that will cause cracking between grains. For pure metals, $\tau \leq 0.5$ ($\theta = 0$), wetting will be complete, but the bridging between grains will not occur, because pure metal freezes at a constant temperature under equilibrium conditions. As such, stress build up will be minimal and CSR cannot be established. In the case of solid solution alloys under non equilibrium heating and rapid cooling conditions, τ will be slightly above 0.5 and wetting of the grain faces will be almost complete, making them inherently susceptible to cracking because only a small area of the grain surface is joined. A higher value of $\tau \geq 0.57 \leq 0.7$, would allow liquid to form at the grain edges and corners while grain faces join and provide a strong bond, and thus prevent cracking.

When metals are immiscible in the molten state and one metal solidifies, τ will be much greater than 0.5 and the susceptibility to cracking will be reduced. Figure 2-14 schematically illustrates the significance of dihedral angle θ and distribution of the liquid phase. The CSR of an alloy is also affected by its solute content. The critical temperature

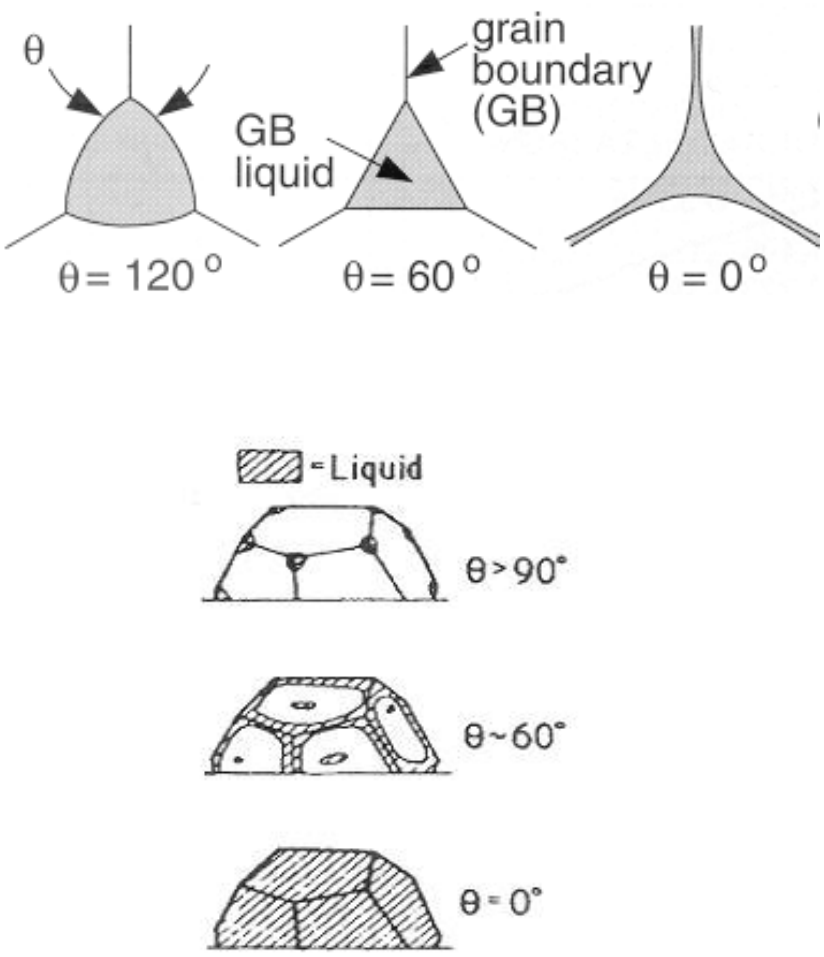

Figure 2-14: Effect of dihedral angle (θ) on the shape and distribution of liquid phase on grain corners, edges and faces [49].

Source: "British Welding Journal" by J.C. Borland. Reproduced courtesy of TWI Ltd (22nd May, 2012)

Tc is depressed with increases in solute concentration, which allows for a greater amount of liquid to persist to much lower temperatures. Also, the solidus will be lowered due to changes in solid solubility. As the extent of the non-equilibrium solidification range increases, so does the CSR which makes the alloy more susceptible to cracking. This will continue until the solidus is not further depressed (limit of solid solubility) and if at the same time *Tc* is further lowered, cracking susceptibility will decrease due to shortening of the CSR. Other investigators [62] modified the generalized theory in attempts to quantify the forces necessary to initiate cracking. Stage 3 in the solidification sequence was further divided into 2 parts; the liquid film stage that occurs early in the process and the liquid droplet stage after the dendrite link and liquid is dispersed. The modification suggests that crack initiation will occur in the liquid film stage while crack propagation alone will be possible in the liquid droplet stage. Based on currently available information and data in literature on the mechanism of solidification cracking in the FZ of welds, the various challenges posed have been largely mitigated through the use of appropriate welding procedures (processes) and proper selection of weld filler materials.

2.7 Liquation Cracking [34]

Liquation cracking in weldments is confined to the HAZ (comprising both the PMZ and the true HAZ), often with the presence of liquid phase at the intergranular fracture surface [34]. It is a general problem that limits the applications of a large number of highly alloyed cast and wrought nickel-base superalloys and stainless steel. Unlike solidification cracking that can be somehow managed, liquation cracking is more insidious and difficult to prevent because the factors responsible for its occurrence in a

material are more often related to the optimized chemistry and microstructure of the material. An established pre-condition required for liquation cracking to occur is the presence of threshold tensile welding stress and a crack susceptible microstructure such as that with liquated grain boundaries. The liquation of HAZ grain boundary during welding causes a solid-solid interfacial bond of the boundaries to be replaced by a weaker solid-liquid bond. Consequently, this reduces the threshold tensile welding stresses that the boundaries can withstand before decohesion occurs. HAZ grain boundary liquation is widely accepted to occur either by non-equilibrium phase transformation below an alloy bulk solidus or super-solidus melting above the equilibrium solidus of the alloy [63-64]. Subsolidus melting is particularly more harmful and detrimental due to its ability to extend the effective melting temperature range and increase the size of the crack susceptible region [65-66].

By following a wide range of investigation into a variety of austenitic alloys and nickel-base superalloys by several investigators [65, 67-69], two major mechanisms commonly used to explain the origin of liquid on HAZ grain boundaries below the bulk solidus of the alloy are grain boundary penetration and grain boundary segregation. The grain boundary penetration mechanism involves a phenomenon known as constitutional liquation of grain boundary second phase particles and the subsequent wetting of the grain boundaries with liquid produced from the liquation process, and/or the interaction of a migrating HAZ grain boundary with liquating particles within the matrix. The penetration of the grain boundary by the liquid at the particle/matrix interface consequently pins the boundary or slows down its rate of migration, allowing uniform wetting by the liquid. Grain boundary segregation on the other hand, involves the

segregation of surface-active elements and/or low melting point depressants, such as B, S and P during casting, thermo-mechanical processing and pre-weld heat treatment. The theories underlying the two mechanisms are further discussed in the next two sections.

2.7.1 Constitutional Liquation Theory [67]

The theory of constitutional liquation and experimental evidence to support the theory were first proposed and explained in the literature by Pepe and Salvage in 1967, in which they observed and reported liquation of titanium sulphide particles in 18-Ni maraging steel [67]. Subsequently, the concept has been observed by several researchers in different alloy systems, some of which are listed in Table 2-5. The theory was illustrated by using a hypothetical binary alloy system as shown in Figure 2-15. Alloy of nominal composition Co that consists of a α solid solution matrix and high melting point intermetallic particles of A_xB_y dispersed as second phase particles within the matrix exhibit different behavior when heated initially at an infinitely slow heating rate, and then at an extremely fast heating rate from temperatures T_1 to T_4.

Under equilibrium conditions that correspond to an infinitely slow heating rate, the solubility of 'B' in an α-matrix increases until the temperature reaches T_2, where the last remaining AxBy particles dissolve, converting the alloy to homogenous single phase solid solution of composition Co. Thereafter, continuous heating from T_2 (where complete dissolution of AxBy particles occurs) to a temperature just below T_5 or at T_4 results in no phase changes. At T_5, also known as the equilibrium solidus temperature, the

first infinitesimal amount of liquid of the composition that corresponds to point 'c' is

Table 2 - 5: Constitutional Liquation in Multi-component Systems

Alloy Systems	**Liquating Phases**
Udimet 700	M_3B_2 [65]
18 Ni Maraging Steel	Titanium Sulphide [67]
Hastelloy X	M_6C [65]
Incoloy 903	MC and MNP Phosphides [70]
Inconel 738	MC-type carbides, γ', M_3B_2, M_2SC [71]
Inconel 600	Ti (CN), Cr_7C_3 [72]
Inconel 718	NbC and Laves phases [73]
DS Rene 80	MC-type carbides, γ', M_5B_3 [32]
Austenitic alloy A286	TiC [70]
Allvac 718 Plus	MC-type carbides [76]

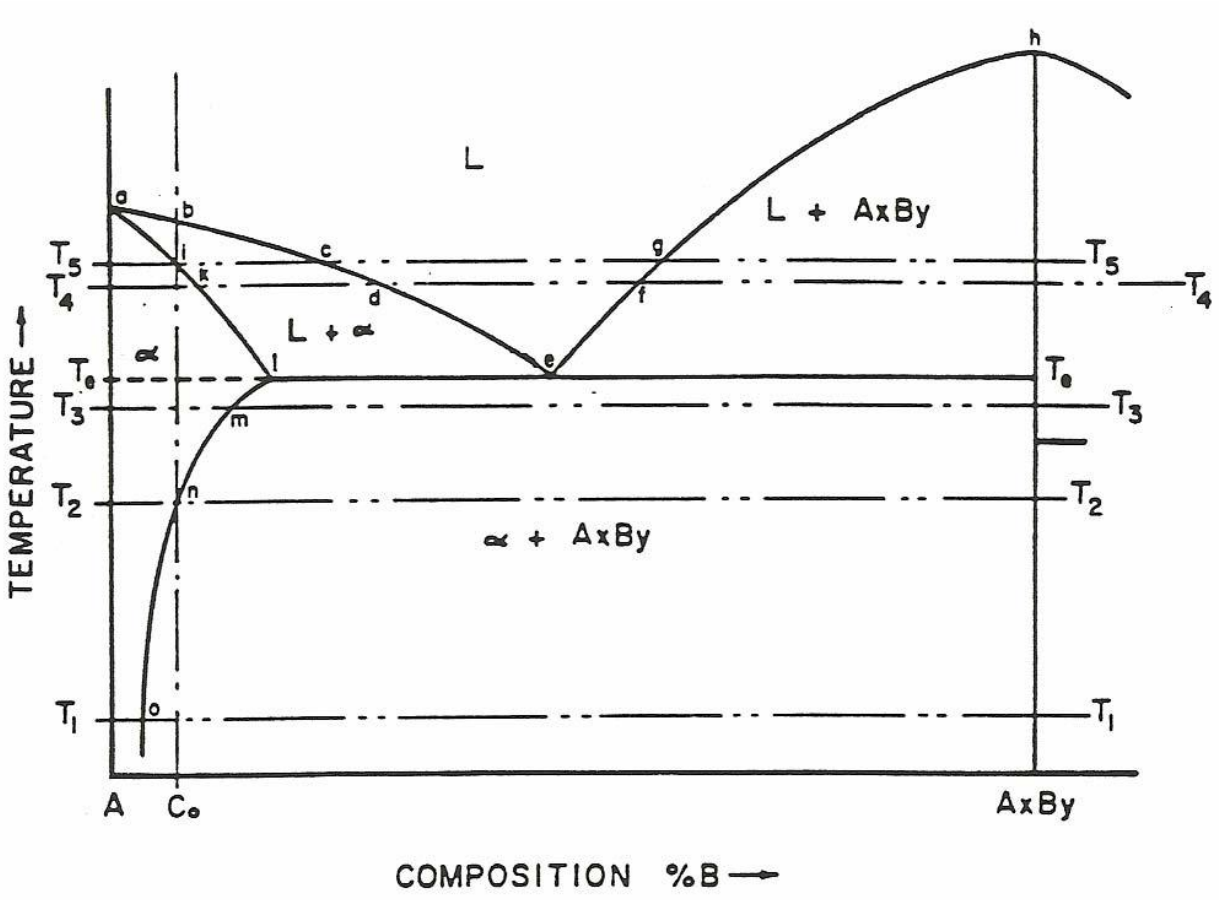

Figure 2-15: Schematic diagram of a portion of hypothetical phase diagram for an alloy system exhibiting constitutional liquation [67]

Source: Welding Journal. Reprinted with permission

formed. In essence, under equilibrium heating condition (extremely slow heating) second phase intermetallic particles with composition within the solubility limit of the alloy can dissolve by diffusional processes before they have the opportunity to react with the α matrix. The behavior of intermetallic particles A_xB_y under non-equilibrium fast heating rate, such as experienced during welding significantly differs from the above description.

The disappearance and/or transformation of a precipitate phase into a solid solution upon heating requires the dissociation of the precipitate phase first, followed by the subsequent accommodation of excess components of the precipitate phase liberated as additional solute within the surrounding matrix. Dissolution and accommodation are temperature dependent processes; hence, the rate at which the excess solute of a precipitate phase will disappear will be finite. Moreover, as the heating rate increases, a critical heating rate will be encountered above which the dissolution of the precipitate phase will be incomplete during the interval required to raise the temperature to the equilibrium solidus. An assumed spherical particle is used to represent precipitate phase A_xB_y for illustration and clarity of the dissolution process. Figure 2-16 schematically shows the changes in the concentration gradient within the surroundings of the particle during heating to temperatures of T_3, T_e, and T_4, respectively. The equilibrium structure of A_xB_y as a function of temperature is represented by the vertical line that emanates from the composition Co in Figure 2-15. In essence, any departure from this equilibrium structure due to rapid heating results in the redistribution of solute since the system would be striving to maintain equilibrium. During non-equilibrium heating to T_3, the A_xB_y particle begin to dissolve since it is unstable with respect to the α matrix at this solute atoms 'B' released from the AxBy particle should diffuse into the adjacent α matrix.

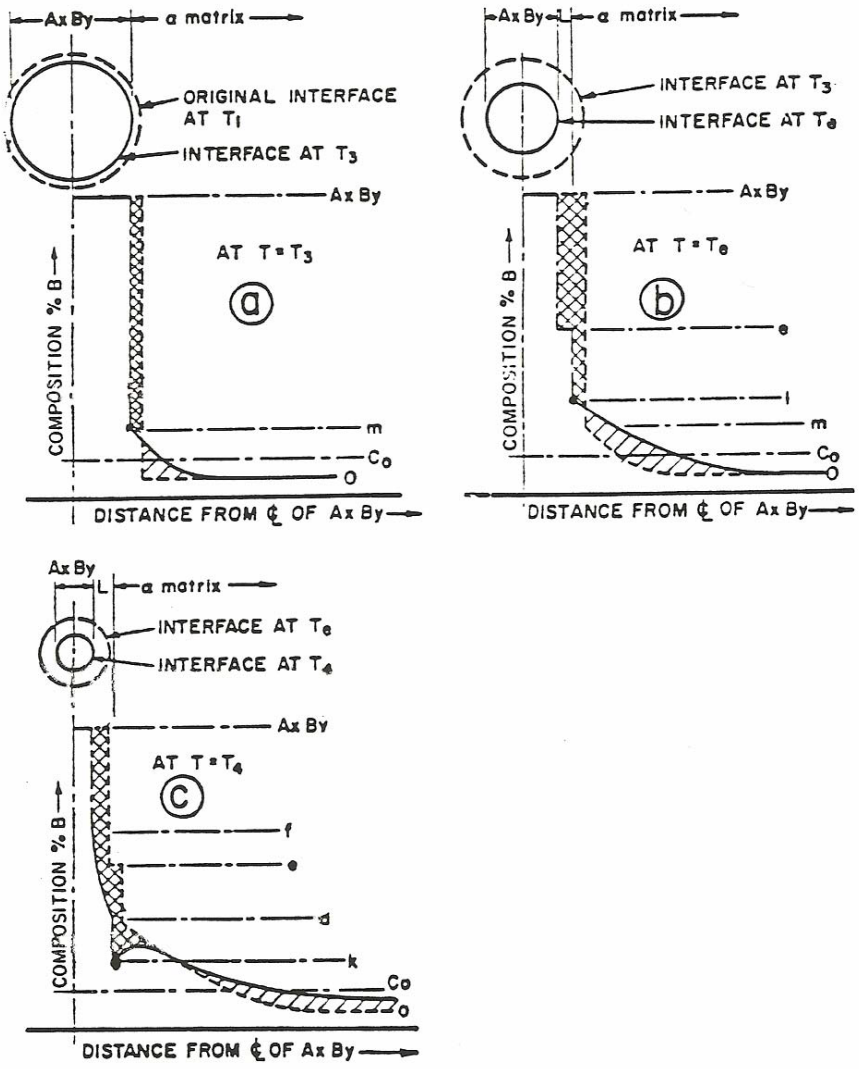

Figure 2-16: Schematic diagram of the concentration gradients at various temperatures during formation of constitutional liquation [67]

Source: Welding Journal. Reprinted with permission

temperature. As such, the AxBy particle will somewhat shrink from its original size to a smaller size, which is shown as dashed and solid circle, respectively, in Figure 2-16a. The

However, as shown in Fig.2-15, the particles must be in contact with the α phase of composition ‘m’ for the two phases to co-exist. Thus a concentration gradient is set up in the α matrix with a maximum of ‘m’ at the AxBy interface and decreases towards the original matrix composition ‘o’ further away into the α phase. To maintain material balance, the area of the double cross-hatched region in Figure 2-16a must be equal to the area of the single cross hatched-region. The concentration gradient slope produced in this way would depend on the following:

1. The heating rate - the faster the heating rate, the steeper the concentration gradient.

2. The diffusivity of solute - the faster the diffusivity of solute atom ‘B’, the shallower the concentration gradient.

3. Accommodation factor- the easier the solute atoms are accommodated within the α-matrix, the shallower the concentration gradient.

As heating continues, temperature increase from T_3 to Te leads to further dissociation and decrease in size of AxBy particles as represented in Figure 2-16b, where the dashed and solid circles represent the location of AxBy interface at T_3 and Te, respectively. At the eutectic temperature, Te, the composition that corresponds to point ‘e’ permits the formation of a single phase liquid at the AxBy interface, hence the undissolved portion of the AxBy particle is surrounded by a liquid of composition ‘e’, which in turn, is surrounded by the α matrix. Figure 2-16b also shows the distribution of solute atom ‘B’ in the three phases that coexist at T_e. Upon further heating to T_4,

additional time is allowed for the dissolution of A_xB_y particles and the expected solute distribution is represented by solid line in Figure 2-16c.

During heating above Te, the equilibrium solubility of α phase decreases along the solidus line 'akl'. Moreover, as the temperature rises above Te through to T_4, the concentrations of the solid solution and the liquid film in contact with one another correspond to 'k' and 'd', respectively (Figure 2-15). This readjustment in composition creates an inverted region in the concentration gradient similar to that shown in Figure 2-16c. The excess solute in the α phase would cause the α/liquid interface to epitaxially move into the α matrix until the excess solute is consumed by a forming liquid of composition 'd'. Therefore, each particle of A_xB_y which remains undissolved at T_4 is surrounded by a liquid film of variable composition that range from 'f' at the A_xB_y interface to 'd' at the matrix interface. As such, localized melting under non-equilibrium heating rates at temperatures below the equilibrium solidus temperature T_5 would be possible. This phenomenon, which is possible anywhere above Te, is referred to as "constitutional liquation". In essence, constitutional liquation is observable whenever an intermetallic compound and the surrounding matrix phase react to form a low melting liquid phase, provided that the heating rate is rapid enough to preclude complete dissolution of the compounds prior to reaching the minimum liquidus temperature.

An exception is however, possible, provided that the initial composition of the alloy is above the solubility limit point 'I', as shown in Figure 2-15. Here, the occurrence of eutectic type melting at A_xB_y/α interface would be independent of the heating rate as A_xB_y would be thermodynamically stable up to the eutectic temperature Te upon which it can form a liquid of composition 'e' [3]. Figures 2-17a-c show the changes in solute

redistribution that occur in a material which exhibits constitutional liquation when rapidly heated to temperature T_4 and then isothermally held for varying lengths of time. During holding, solute atom 'B' would diffuse from the liquid into the α-matrix which results in a gradual decrease in the width of the liquid phase. Eventually, nearly complete homogenization would occur, thereby permitting the liquid to completely solidify. After the solidification of the liquid, the composition gradient of solute atom 'B' in the α-matrix reaches a maximum that corresponds to composition 'k' (the maximum solubility of 'B' atom in the α phase at T_4) at the original centerline of A_xB_y and decreases towards the composition that corresponds to point 'O' at the interior of the α-matrix. Thus the liquid produced by constitutional liquation should experience a gradual modification in composition once the A_xB_y phase is completely dissolved and should ultimately disappear by solidification if subjected to a sufficiently long enough isothermal hold at any temperature below the equilibrium solidus.

Another notable influence on the occurrence of constitutional liquation in alloys is the solid-state dissolution behavior of their second phase precipitates. The ease of dissolution of interstitial compounds, like Fe_3C, and the rapid diffusion of their solute atom 'C' makes constitutional liquation less feasible, except where it involves an extremely rapid heating/cooling rate as verified ($625^oC/s$ for < 2 μm Fe_3C) by Aronson [76]. In contrast, less readily dissolvable alloy carbides/intermetallic compounds with substitutional type solute are readily more susceptible to liquation except for conditions where the heating rate during welding is extremely slow.

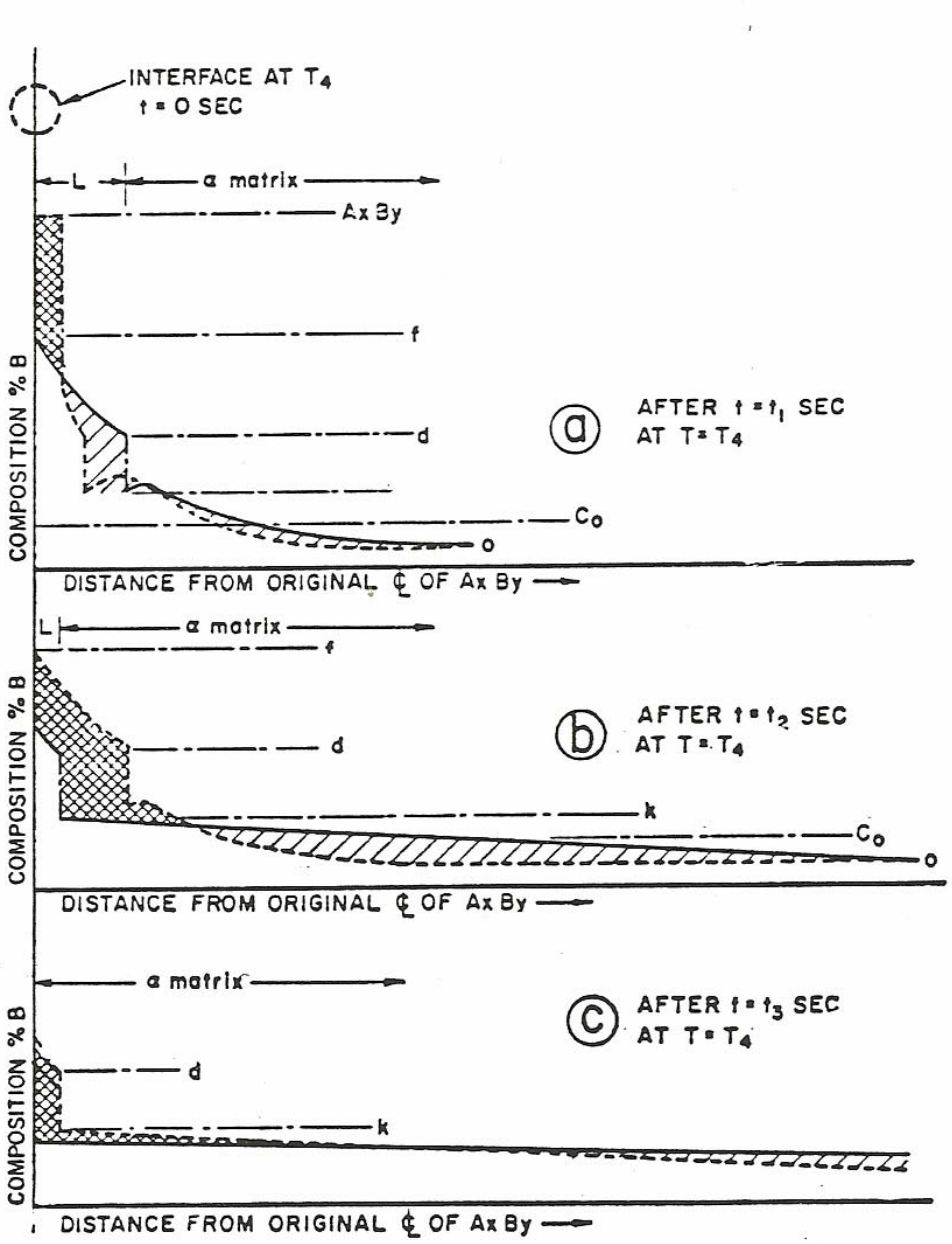

Figure 2-17: Schematic diagram of the effect of holding time on the stability of liquid film produced by constitutional liquation [67]

Source: Welding Journal. Reprinted with permission

2.7.2 Grain Boundary Segregation

Liquation cracking along boundaries can also occur as a result of segregation of surface active elements, most of which are also melting point depressant impurities, to the grain boundaries prior to welding. The segregants lower the liquating temperature of the boundaries relative to the surrounding matrix and cause preferential non-equilibrium subsolidus melting of the HAZ segregate region during the weld thermal cycle and subject the boundary to liquation cracking. This segregation mechanism has been used to rationalize the onset of grain boundary liquation in some alloys where constitutional liquation does not or cannot occur due to the absence of constituent particles/phases [77].

The metallurgical basis for preferential grain boundary segregation is the diffusion of solutes or impurity elements to loosely pack or disordered region such as grain boundary. Other loosely packed regions include: free surfaces, particle/matrix interfaces, stacking faults and phase boundaries. The tendency for segregation to grain boundaries is related to the solubility of a given elements in a given matrix phase. The degree of segregation can be quantified by using a grain boundary enrichment factor (β_b), defined as:

$$\beta_b = C_b/C_o \quad \text{..... (2.13)}$$

where C_b = the equilibrium concentration of the element at the boundary;

C_o= the equilibrium concentration in the matrix.

A higher β_b indicates a higher probability for the solutes or impurity elements to segregate to the boundaries. The enrichment of grain boundaries by solutes/impurity atoms prior to welding is a diffusion-controlled process and can occur by either

equilibrium segregation [78-80] or non-equilibrium segregation mechanism [81-87]. Equilibrium grain boundary segregation occurs when a material or alloy is isothermally held at a sufficiently high temperature to permit appreciable diffusion of the solute or impurity atoms from the bulk matrix to the grain boundary where it is absorbed to reduce the interfacial free energy and the segregated structure forming a stable equilibrium condition. Here, the driving force for equilibrium segregation of solute elements in a material is born out of the need to better satisfy atomic bonding requirement in the disordered structure of the interface and reduce the high free energy of the interface to the barest minimum.

The magnitude of equilibrium segregation increases as the temperature of isothermal treatment decreases as well as with an increase in the initial solute concentration in the matrix. The vibrational amplitude of lattice atoms increases with increasing temperature such that the driving force for solute atom migration from the grains to the interfaces is reduced, and also, the degree of equilibrium segregation. At lower annealing temperatures, the tendency for segregating atoms to diffuse to grain boundaries is high, but energetically difficult. Consequently, the rate of segregation progressively reduced beyond the initial increase which accompanies the decrease in temperature. Therefore, there is an optimum temperature at which the highest degree of equilibrium segregation occurs. A distinguishing feature of equilibrium segregation is that the segregated solute atoms are generally restricted to a few atomic layers because of limitations of the structural perturbation of the grain boundaries that do not extend beyond a few atom distances. The total amount of segregation is usually in the order of a few monolayers. Also, equilibrium segregation is a completely reversible process and as

such, the chemical enrichment at the grain boundaries and other interfaces can be reproduced by re-establishing the identical physiochemical conditions [79].

The phenomenon of non-equilibrium segregation was first characterized by Westbrook, and Aust and colleagues [81-86] when an unusual grain boundary hardening phenomenon could not be explained in term of equilibrium segregation. A mechanism was suggested in which the effect was accounted for by the abnormal generation and/or motion of some type of defect in the vicinity of the grain boundary which also required the presence of solute atoms [82]. A solute-clustering model was later proposed based on preferential solute-vacancy interactions and non-ideal thermodynamic behaviors of the binary system which is summarized as follows. In addition to the equilibrium vacancies concentration generated and distributed at the annealing temperature during thermal treatment, some vacancy-solute complexes can also form as a result of positive binding energy between the solute atom and vacancy [88], hence, migration/diffusion is energetically favored when the diffusion coefficient of the solute-vacancy complex exceeds that of the vacancies alone. As such, when materials are quenched from a high temperature annealing process, the equilibrium vacancy concentration, which is initially very high, falls and vacancy flows to interfaces such as grain boundaries where they can be readily annihilated.

The annihilation of vacancies at grain boundaries produces a concentration gradient of complexes, which drives the complexes (those with positive solute-vacancy binding energy) to diffuse from within the grain to the grain boundary regions where the vacancies are annihilated and the solute atoms occupy grain boundary position. This would eventually result in excessive concentration of solute atoms (segregant) at and

within the vicinity of grain boundaries. The effective uphill diffusion of solute atoms, which produces a solute-rich boundary region, is thermodynamically driven by the decrease in free energy associated with the annihilation of excess vacancies at the boundary sink. Therefore, non-equilibrium segregation is generally viewed from the concept of the formation of atom-vacancy complexes within the lattices of a polycrystalline material/alloy, and the presence of a gradient in the concentration of complexes between the grain interior and the grain boundaries. This type of segregation occurs during cooling from thermal treatment or during annealing following plastic deformation, and the extent of segregation is highly sensitive to cooling rate apart from the starting temperature, bulk concentration of solutes as well as the binding energy between the solute atoms and vacancies [88]. Since an increase in the peak annealing temperature increases the equilibrium concentration of vacancies as well as the tendency for segregation, insufficient time for diffusion of solute-vacancies complex to grain boundaries as a result of rapid cooling rates will lead to a drastic reduction in the extent of segregation.

In contrast, if the cooling rate is very slow, and causes a gradient in the concentration of solute atoms between the grain boundary and the grain interior, the segregated solute atoms may diffuse back to the grain interiors, thereby eliminating segregation [89]. In essence, intermediate cooling rates favors non-equilibrium segregations. For complex alloys, such as ternary system alloys, different solutes may interact at the grain boundaries and the synergetic effects can enhance or decrease segregation. Guttmann [90] proposed that the free energy of segregation of one species may be increased by the second if the interaction between the two species are negative,

that is, attractive. Grain boundary segregation can also take place during welding, depending on the peak temperature that the materials are exposed to and the diffusion time that is available [91]. To account for this, various mechanisms were proposed, some of which include:

1) Grain boundary sweeping of solute atom during grain growth due to their lower energy relative to the matrix,

2) Pipeline diffusion of solute atoms along grain boundaries that are continuous from the FZ to PMZ, providing conduits for elemental segregation and enrichment of the HAZ grain boundaries, because diffusion along grain boundaries is of a higher order of magnitude than in the bulk matrix [30] and

3) Gibbsian segregation mechanism which rationalizes segregation to a static HAZ grain boundary, in that, equilibrium diffusion is achieved by diffusion of low energy solute atoms in segregated region of the matrix localized within a few atom diameters on either side of the high energy grain boundary [79].

However, the principal source of segregation of surface active low melting point depressant (LMPD) elements in welded components is known to be as a result of pre-weld thermal treatment. A considerable amount of work has been carried out by researchers on the contribution of grain boundary segregation mechanisms to HAZ liquation cracking. Both equilibrium and non-equilibrium segregation were found to enhance liquid wettability of grain boundaries. The presence of LMPD elements or

impurity solutes atoms in grain boundary liquid lowers the solidification range of the liquid and contributes to HAZ microfissuring. Segregation of B [92-93], P, C [94] and S [95] in wrought and cast Inconel 718 has been extensively investigated. The findings showed that, boron segregation to grain boundaries either by equilibrium and/or non-equilibrium modes affect the on-heating and on-cooling hot ductility values. Sulphur, like B, also increases the solidification temperature range by increasing the nil-ductility range on cooling. In another study, the elemental segregation of B and the associated grain boundaries liquation were found to be dependent on both the grain size and the character of the grain boundary [96-97]. High angle grain boundaries have more segregation intensity and were more susceptible to liquation. Variations in intensity of B segregation with grain size and increase in the initial boron concentration have also been corroborated with susceptibility to HAZ liquation cracking in IN 718Plus superalloy [98-99].

2.8 Post-Weld Heat Treatment Cracking in Superalloys [100-105]

Post-weld heat treatment (PWHT) cracking is also referred to as strain age or reheat cracking. This type of cracking occurs during the PWHT cycle, which has been essentially developed to optimize mechanical properties and relax residual stresses due to welding while homogenizing the microstructure of precipitation strengthened nickel-base alloys. PWHT cracking may also occur during repair welding, where the weld is given a complete heat treatment that involves standard solution heat treatment followed by aging. The PWHT cycle usually involves a solution anneal followed by a period of aging at about 650-850^{o}C. Cracks that form during the cycle often commence in the HAZ but can

extend to the base metal and/or the FZ. The cracks are also intergranular in nature and range in size from microscopic to a few centimeters in length. The origin of this type of cracking in nickel-base γ' strengthened superalloys has been attributed to the coincidence in the temperature range at which stress relief and γ' phase precipitation begin to occur [10, 100, 102 -105].

During welding, the peak temperature attained by the FZ and HAZ alters their microstructure and results in high residual stresses being retained after the weld has cooled and solidified. The subsequent PWHT cycles to restore the properties more often involve heating the alloy to a temperature range, whereby it passes through the γ' precipitation temperature range T_1 through to T_2 as depicted in Figure 2-18. As such, two processes occur simultaneously for an alloy with fast γ' precipitation kinetics; the residual welding stress tends to be relaxed while the alloy undergoes a rapid stiffening of its grain interior due to the γ' precipitation (with consequential loss of ductility). The inability of the alloy to adequately stress relief coupled with the fact that it is rather gaining strength by rapid γ' precipitation at the same time can lead to PWHT cracking, more so especially in regions that had liquated during welding operations. Also, if there is a significant difference in the lattice parameter of γ' and that of the γ matrix, precipitation of significant volume fraction of γ' during aging may result in shrinkage contraction of an alloy with consequent initiation of cracks in restrained or welds made of thicker section.

Therefore, the generalized view is that PWHT cracking occurs due to the cumulative effects of residual welding and aging contraction stresses that act on the HAZ which has been embrittled by various metallurgical reactions. Various factors that influence the occurrence of PWHT cracking as reported by various investigators in the

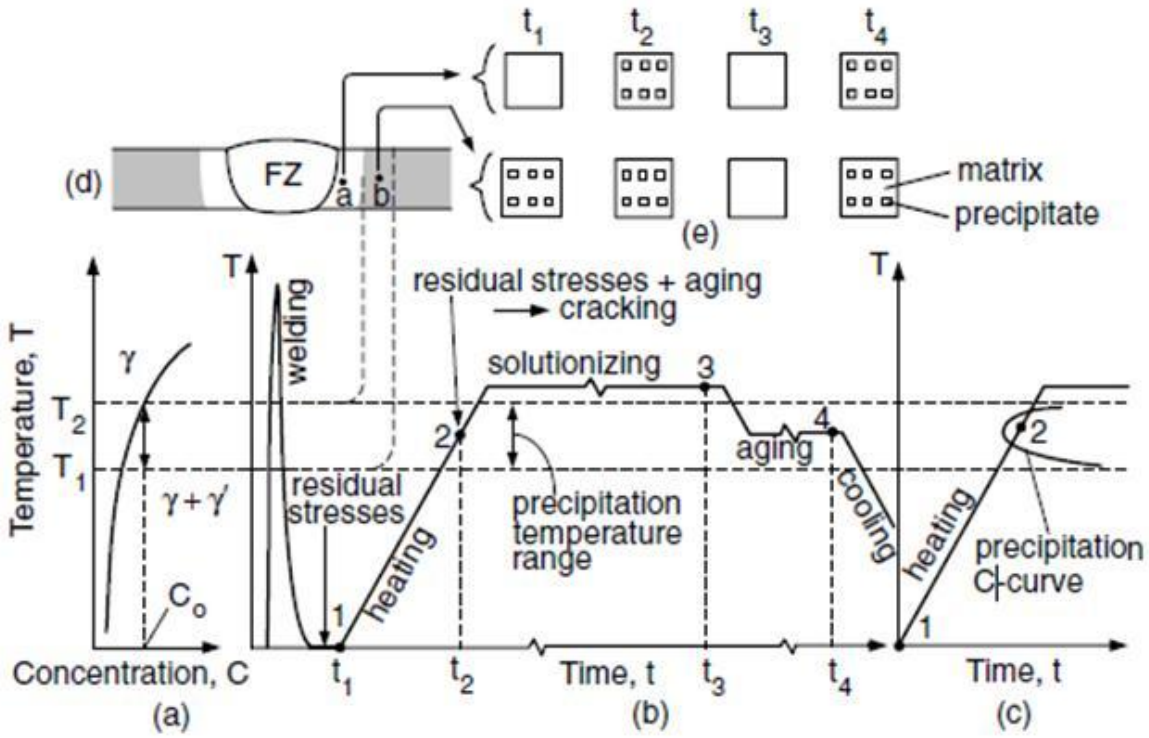

Figure 2-18: Schematic of Post-weld heat treatment cracking sequence: a) phase diagram, b) thermal cycles during welding and heat treating, c) precipitation C curve, d) weld cross-section, e) changes in microstructure [34].

Source: "Welding Metallurgy" (2nd Ed) by Sindo Kuo. Reprinted with permission from the Global Rights Department, John Wiley & Sons, Inc. (28th October, 2011)

literature are summarized as follows.

1. Chemical composition: Figure 2-19 shows the influence of Ti and Al content on the susceptibility of nickel-base alloy to strain-age cracking. Alloys above the dashed line (with Al + Ti content > 6 wt %) are highly susceptible to cracking during welding and PWHT while alloys below the dashed line, which have a lower content of Ti and Al are readily weldable. This variation in cracking with Al + Ti content has been attributed to the fact that the two elements are the major γ' forming elements. As such, the rate of precipitation and volume fraction of γ' are expected to increase with an increase in Al + Ti concentration. Consequently, such alloys will age harden rapidly with the attendant rapid stiffening of their matrix and formation of aging contraction stresses, which could promote cracking of weak HAZ grain boundaries.

   Alloys, like Rene 41 and Waspaloy which are in the same class as Haynes alloy 282, fall on the borderline as depicted in Figure 2-19. They are reported as readily weldable with some difficulty, but often crack during PWHT [11-12, 27]. The addition of Nb as one of the primary alloying elements in some alloys, such as IN 718, promotes the formation of γ'' precipitates instead of γ'. The γ'' has a sluggish aging response, such that alloys that are predominantly strengthened by γ'' are generally more resistant to PWHT cracking. The influence of minor alloying elements is however a major research interest. Low level of C content has been reported to enhance resistance to PWHT [103]. Another investigator [102] however, found that low C content is detrimental to PWHT resistance and attributed this to the tendency of the low C alloys to undergo grain coarsening in the absence of a large volume fraction carbides along grain boundaries. A statistical correlation has been observed

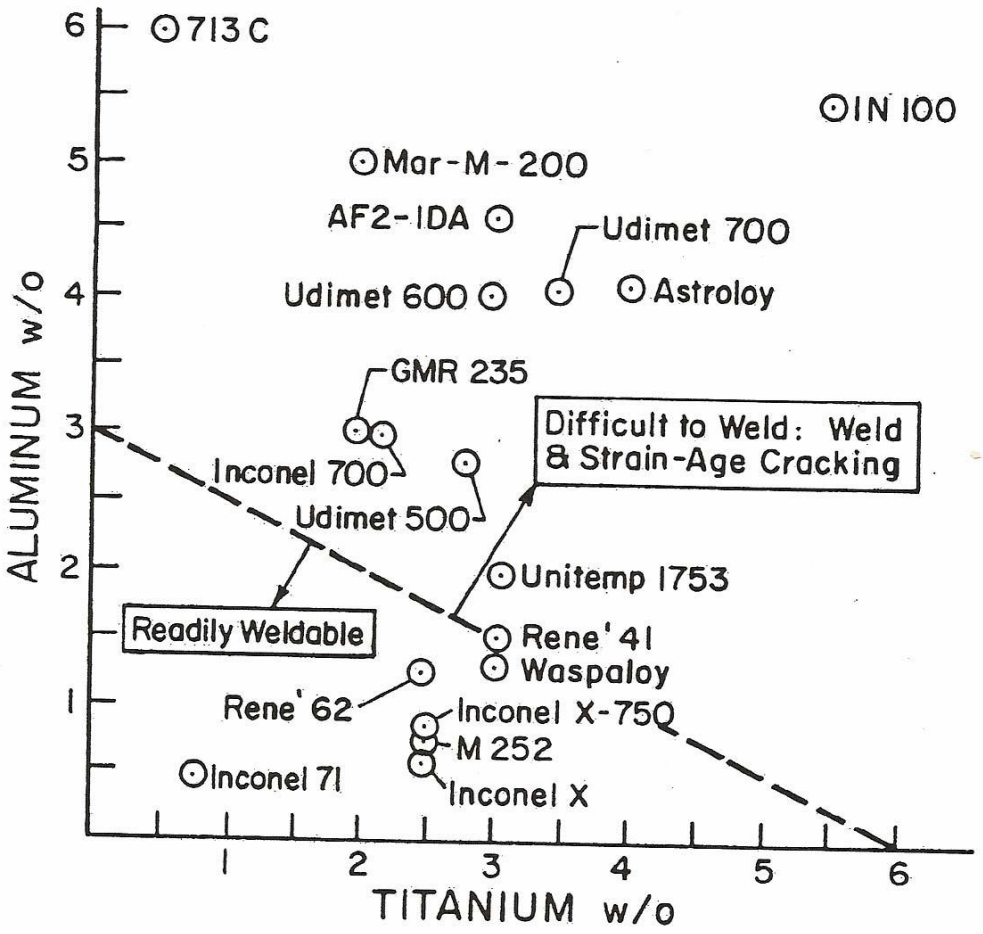

Figure 2-19: Relationship between estimated weldability and Aluminum + Titanium content [34]

Source: "Welding Metallurgy" (2nd Ed) by Sindo Kuo. Reprinted with permission from the Global Rights Department, John Wiley & Sons, Inc. (28th October, 2011)

for SAC resistance and B content, with higher B content significantly improving resistance to this type of failure [100].

2. Prior grain boundary liquation: It is acknowledged that PWHT cracks preferentially initiate on HAZ grain boundaries which have been embrittled/weakened by prior liquation reactions that had occurred on the grain boundaries during welding. As such, any microstructural modification capable of controlling metallurgical reactions like grain boundary liquation during welding can significantly reduce the susceptibility of an alloy to PWHT cracking.

3. Grain size: Reports from investigators [102, 106] have shown that fine-grained alloys are more resistant to PWHT cracking than those that are relatively coarse. This has been attributed to the relative ease of stress relaxation by grain boundary sliding in fine-grained alloys. Grain boundary sliding is one means through which the high strains/stresses associated with a steep thermal gradient can be accommodated. However, large amounts of sliding can increase the stress on grain boundary facets and lead to initiation of cracks, especially in a coarse grain structure. In contrast, a higher number of grain boundary triple points in fine-grained alloys can slow down the linking up of voids which are formed at individual grain boundary facets.

4. Pre-weld heat treatment: The pre-weld microstructural condition of an alloy is a critical factor that influences its susceptibility to cracking during welding as well as during PWHT. In some precipitation hardened nickel-base alloys, welding in

overaged conditions tends to reduce the occurrence of SAC. In these cases, the reduction in SAC is attributed to the fact that the overaged base metal remains soft and ductile while the HAZ becomes comparatively stronger and less ductile, due to aging during PWHT. As such, stress relaxation could then be forced on the weaker, more ductile and voluminous base metal than the HAZ, which has relatively little capacity to accommodate strain [10, 98, 107]. In Rene 41, slow cooling from pre-weld solution annealing temperature was observed to induce superior resistance to SAC, but solution heat treatment at 1080^{o}C for 25 minutes followed by water quenching has also been reported to improve SAC resistance relative to base metal overaging treatments [12].

5. Post-weld heat treatment cycle: Normal PWHT cycle consist of solution annealing at pre-weld solution treatment temperature followed by aging. Rapid heating to post-weld solution annealing temperature has been shown to reduce the occurrence of SAC in Rene 41 [106]. Rapid heating allows for sufficient stress relief and reduces residual stress to the barest minimum level before the grain boundaries are embrittled by the aging reaction. This procedure is reported to be satisfactory in reducing the occurrence of SAC in some nickel-base superalloys with an Al + Ti content of about 4% [108], however, it is not successful with alloys of significantly higher Al + Ti content. Moreover, achieving a uniform heating rate in a massively welded assembly that has varying thick sections may be difficult, and may even induce a higher level of detrimental thermal stresses. A solution proposed for this problem [109] is a stepped-heating technique in which the component is slowly heated to about 500^{o}C, soaked at

this temperature to minimize thermal gradient within the components, and then rapidly heated through the mid-range ductility dip (precipitation range of γ') to the solution treatment temperature.

6. Heat treating environment: A study by Thompson et al. [110] showed that PWHT cycle performed in a dry and inert atmosphere can reduce the occurrence of SAC cracking as little or no oxygen is available to embrittle grain boundaries. Their findings showed that severe SAC occurs only in an oxygen containing atmosphere. Further, the severe detrimental effect of oxygen was found occur at a low concentration of 2 vol. %. The detrimental effects of an oxygen-rich atmosphere was rationalized to be due to the rapid diffusion of oxygen along grain boundaries and the consequent formation of oxides, which are not able to resist plastic deformation.

2.9 Weldability and Weldability Testing Techniques

Weldability is the capacity of a metal or combination of metals to be welded under fabrication condition into a specific suitable designed structure and to perform satisfactorily in intended services [111]. Weldability in itself is a qualitative term that is affected by other measurable factors which are encountered during fabrication and in service. Superalloys in general can be readily melted and re-solidified into weldments by using any common welding process. However, the weldability of superalloys extends beyond melting and resolidification as it primarily depends on microstructural and mechanical property considerations. Weldability can be broadly classified into two types, namely fabrication and service weldability. Service weldability views weldability from

the perception of strength, toughness and creep resistance of the FZ and HAZ, matching that of the base metal. Fabrication weldability, on the other hand, assesses the susceptibility of weldment to hot, cold and stress relief cracking that must be avoided along with other weld defects. Fabrication weldability or susceptibility to cracking can be quantified by the threshold stress or strain to induce a crack, or the degree of cracking under a specific level of stress or strain.

Baeslack and Lippold [112] classified weldability testing techniques into representative and simulative tests depending on the manner in which the strain and stress are applied. Wang [69], however, classified the test into three categories with the addition of high temperature mechanical tests and other commonly used techniques as shown in Figure 2-20. A numbers of weldability assessment techniques are available to check the integrity of welded joints. One of the most widely used of all the weldability testing techniques is the Gleeble hot ductility test. Another commonly used method to determine the quantitative index of the cracking susceptibility is total crack length (TCL) measurement in both the HAZ and FZ of welds, especially for experimental purposes. A brief review of some of the various weldability testing methods are provided in the next section.

2.9.1 The Varestraint Test.

The original Varestraint test was developed by Savage et.al [113] in mid 1960s as a technique to assess base metal weldability and the influence of welding processes and parameters on solidification and HAZ liquation cracking. Over the years different and modified versions have been developed, namely, the mini-Varestraint, spot-Varestraint

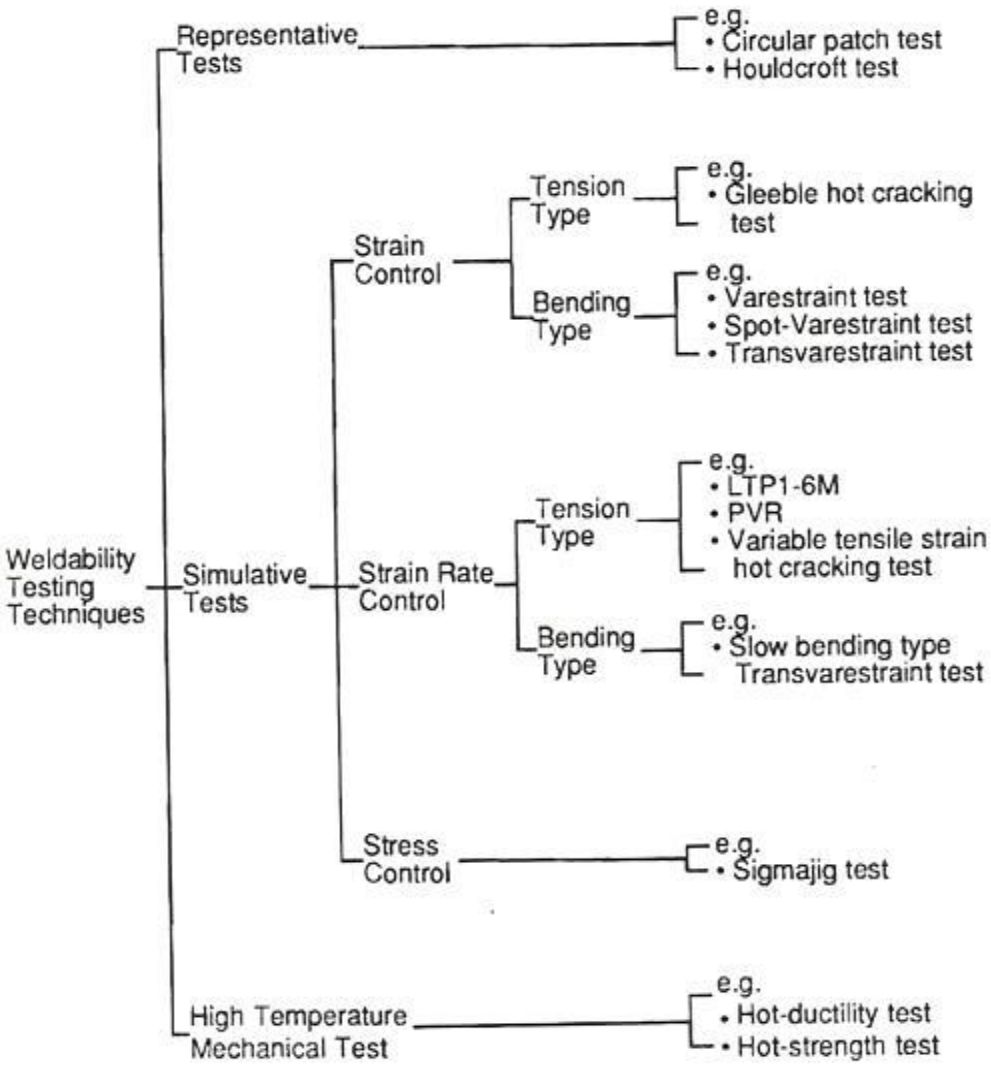

Figure 2 - 20: Classification of the various weldability testing techniques [69]

Source: "PhD Thesis 1991" by Lin Wangen. Reprinted with permission from the Author (17th April, 2012)

and transvarestraint test. The mini-Varestraint test uses a test sample that is smaller in size, nominally 163 x 25 x 6.4 mm as compared to the original varestraint test sample with 300 x 50 x 13 mm. It is also referred to as the longitudinal-Varestraint test because the welding is performed longitudinally to the direction of welding.

Figure 2-21 shows a schematic representation of the longitudinal-varestraint test with the specimen supported as a cantilever beam at one end and a gas tungsten-arc weld (GTAW) is produced in the centre section of the specimen. As the arc approaches the centre of a removable die block with a known radius attached to the cantilever beam (marked A in Fig. 2-21), a pneumatically operated ram is triggered and forces the specimen to conform to the surface of the die block. The applied augmented strain (ε) at the top surface of the specimen can be varied by adjusting the radius of the die block (R) by following the equation;

$$\varepsilon = t/ (2R + t), \text{ ---------- (2.14)}$$

where t is the specimen thickness and R is the radius of the die block. As such, both weld solidification cracks and HAZ liquation cracks are produced. Susceptibility to cracking is quantified by measuring the cracked HAZ length (CHL), maximum crack length (MCL) or total crack length (TCL) on the tested specimen surface. The threshold strain to cause cracks and the degree of cracking at a specific strain level or welding variable and the extent of microstructural changes have been widely evaluated as the cracking threshold [105, 107-108]. After testing, as-welded specimens are examined under a microscope at 50 X magnification.

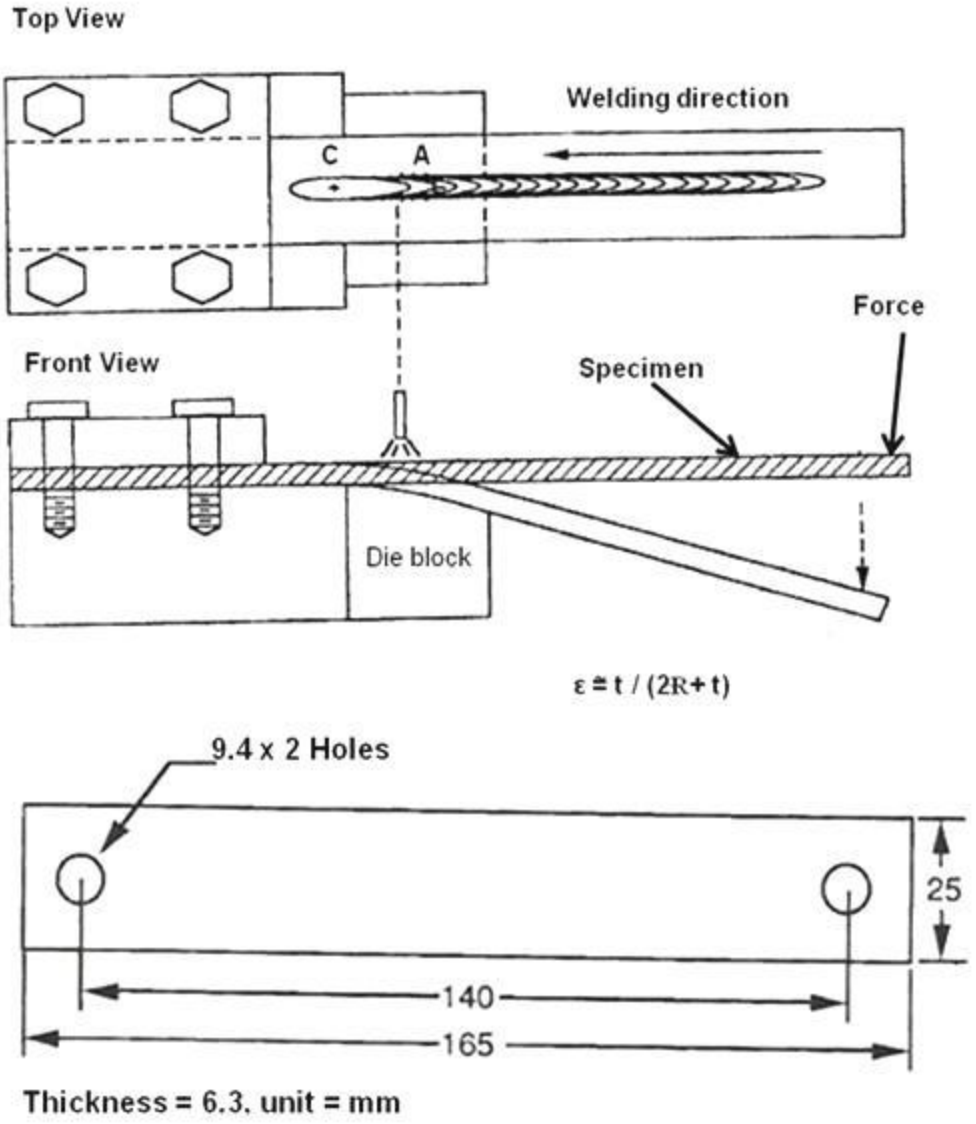

Figure 2-21: Schematic representation of longitudinal varestraint test [69]

Source: "PhD Thesis 1991" by Lin Wang. Reprinted with permission from the Author (17th April, 2012)

2.9.2 Spot - Varestraint Test

This version of the Varestraint test utilizes a gas tungsten-arc spot weld generated at the centre of a test sample rather than a continuous longitudinal weld. In order to evaluate the cracking susceptibility of a material, augmented strain is applied at a time when the material has a crack susceptible microstructure which is created by producing a spot weld. Figure 2-22 shows a schematic of the test apparatus, and the specimen dimensions are 150 x 25 x 6.4 mm. After a predetermined weld time, the arc is extinguished and the specimen is forced to conform to the radius of the die-block. In this manner, HAZ liquation cracks can be generated on the specimen adjacent to the GTA spot weld. The relationship in Equation 2.14 is used to determine the threshold strain/stress that causes cracks while the degree of cracking is determined by using similar quantification parameters for the mini-Varestraint test.

2.9.3 Gleeble Hot Ductility Test

Gleeble thermo-mechanical simulator equipment consists of a time-temperature control device for evaluating the effect of thermal cycle on the hot ductility of materials. A typical hot ductility test utilizes a sample gripped between water-cooled copper jaws through which an electric current is passed, and uses a thermocouple attached to the mid section of the specimen to provide feedback to control the system. The sample is rapidly heated by electric resistance heating, and at an appropriate time in the thermal cycle, a high strain rate load, which simulates the force experienced by the HAZ, is applied to fracture the specimen at the desired temperature on-heating or on-cooling. The thermal cycle, which the specimen had experienced, the ultimate tensile load for fracture and the

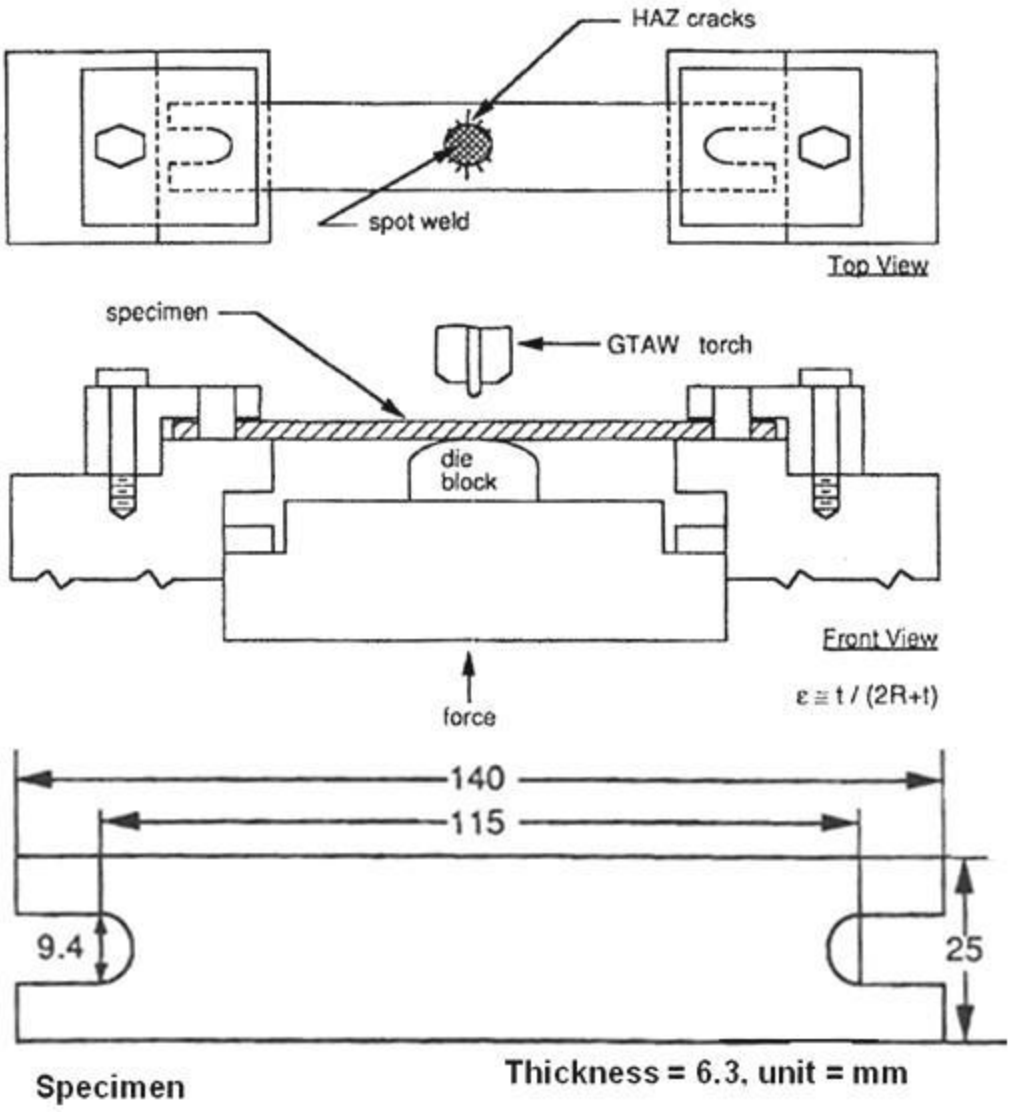

Figure 2-22: Schematic representation of spot-varestraint test [69].

Source: "PhD Thesis 1991" by Lin Wang. Reprinted with permission from the Author (17th April, 2012)

amount of elongation or reduction in area to failure can be recorded by appropriate instrumentation attached to the equipment. Alloys ductility as a function of temperature varies on-heating and on-cooling and this is measured by pulling the specimen to failure and measuring the elongation or reduction in the area at the fracture region.

During on-heating, at a particular temperature, the ductility of the alloy drops to zero. This temperature is known as the Nil Ductility Temperature (NDT). Upon further heating, the alloy loses all its strength along with the ductility at a temperature referred to as the Nil Strength Temperature (NST). During on-cooling, from above the NDT or NST, the alloy will begin to recover some level of ductility at a specific temperature called the Ductility Recovery Temperature (DRT). The detection of these three main types of temperatures, the reduction in area measurement of the sample and the ultimate tensile stress constitute the Gleeble hot ductility test and these data have been used to evaluate the susceptibility of alloys to HAZ liquation cracking. Hot ductility data have been interpreted in various ways by investigators in the bid to ensure proper correlation with HAZ liquation cracking susceptibility.

The importance of the ductility recovery temperature and the rate of recovery on-cooling from elevated temperatures were proposed as a measure of HAZ liquation cracking susceptibility by Nipples et al. [117]. Other investigators suggested that the extent of the zero ductility range (ZDR) during heating, that is, the temperature range between NDT and NST (also taken as the liquidus temperature T_L – DRT and called ZDTR) as well as the amount and rate of recovery are equally important [115]. A larger ZDR indicates a greater sensitivity to HAZ liquation cracking. A cracking factor, (NST – DRT) / NST X 100, based on the temperature range between NST and DRT was

proposed by Muesch [118], similar to that utilized by Donati et al [116] to predict cracking tendency in 18Cr-10Ni austenitic steels. Williams [119] proposed that hot strength in addition to ductility behavior is an important parameter in determining cracking susceptibility since a material can either elastically or plastically accommodate strain. For materials with similar on-cooling hot ductility behavior, those with higher hot strength recovery rate were adjudged to be less susceptible to cracking. Figures 2-23a and b are typical hot ductility curves for materials that,

(a) have good resistance to cracking and

(b) are highly susceptible to cracking.

The behavior of the material in Figure 2-23a indicate that it has good ductility when tested on-heating close to the NDT and the ductility curve obtained on-cooling is also essentially comparable to the on-heating curve. In Figure 2-23b, although the material shows good ductility on-heating, but the on-cooling curve from the NDT shows a marked difference; it exhibits poor ductility by remaining at the nil-ductility level for a considerable amount of time or shows limited insignificant recovery. This delay in ductility recovery of the simulated materials during the on-cooling portion of the weld thermal cycle has been considered to be partly responsible for the HAZ cracking during welding. The relationship between partial or bulk melting to the three critical temperature parameters determined by hot ductility testing is another factor that has received considerable attention in the literature. Some reports have suggested that liquation (partial melting) occurs at the NDT [121] while others are of the opinion that it occurs when the ductility begins to drop on-heating, that is, below the NDT [116]. A counter argument

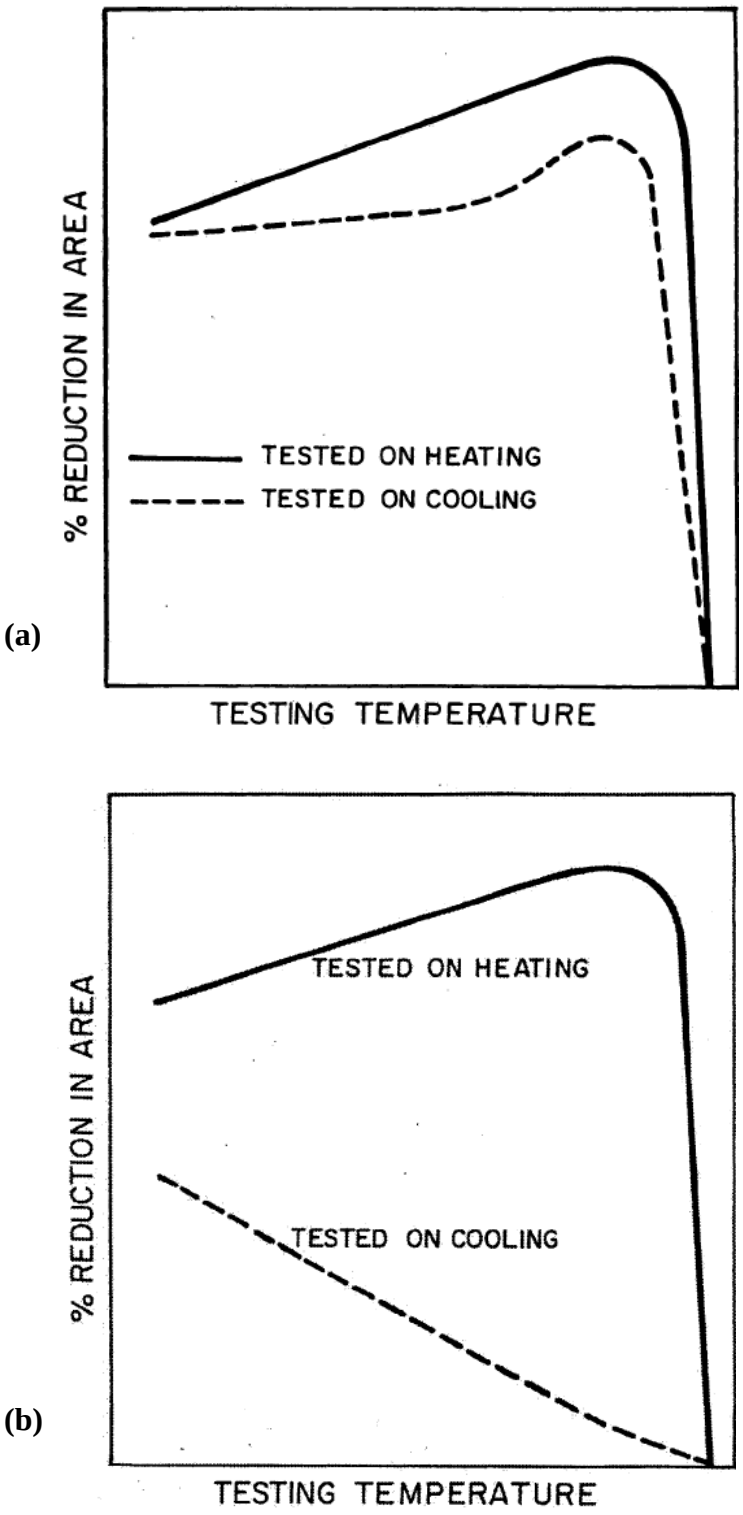

Figure 2-23: Schematic representation of the typical behavior of (a) highly crack resistant materials and (b) cracks susceptible materials [118].

Source: Welding Journal [118]. Reprinted with permission

claims that changes in the fracture mode from transgranular to intergranular occur when ductility drops and that liquation only starts at a temperature in excess of the NDT [120]. It was suggested that data obtained during on-cooling test from NST or above are more appropriate data than the test data obtained with NDT as the peak temperature especially when discriminating cracking resistance between different materials.

Important testing parameters during the Gleeble hot ductility test recognized by Lundin et al. [115] include: peak temperature, crosshead speed or stroke rate, holding time at the testing temperature, holding time at the peak temperature, thermocouple attachment techniques and thermal cycle in the case of SMAW. The fracture surface of hot-ductility samples have also been examined for information about the mechanism involved in ductility loss and liquation cracking. Liquation of carbides and grain boundary liquation due to segregation of surface active elements, like boron, in some nickel-base alloy have been observed on fracture surface [121-122]. Qian et al. [122] observed that complete intergranular fracture occurred in Waspaloy bar and disk samples at temperature above the NST and DRT, which indicates that a high temperature grain boundary weakening phenomenon is the major contribution to failure.

Apart from performing high speed hot tensile tests, Gleeble equipment is also instrumented such that the heating and cooling of the specimens can be accurately programmed to reproduce the rapid temperature changes that occur during welding. Since the HAZ of weldment is often narrow, the microstructure as well as the peak temperature attained within this narrow region varies considerably from the fusion boundary to the unaffected base metal, owing to the temperature gradient. Gleeble simulation is therefore often employed to reproduce in a test bar the time-temperature cycle experienced by the

metal adjacent to the weld zone during the welding operation. As such, a sufficient volume of HAZ is obtained which enable proper characterization of the metallurgical and mechanical changes during weld thermal cycles.

2.9.4 Total Crack Length (TCL) Measurements

The weldability tendency of a material has also been assessed by measuring the TCL in weldment, especially those made for experimental and/or material selection purposes. Materials are welded in the desirable heat treatment condition by using actual welding techniques and parameters that are to be used to make the actual weld. The welded specimens are then cut into sections perpendicular to the welding direction. A cracking index which is a measure of the cracking tendency is then evaluated by normalizing the TCL with area of the HAZ, which varies/depends on heat input (parameters), using the relationship utilized by [54] and defined below as,

$$CI = (l1 + l2 + l3 + \cdots)/(Area\ of\ HAZ) \quad \text{..... (2.15)}$$

where CI is the cracking index, and l_1, l_2 and l_3 are individual crack length measured from one section of each welded specimen. The CI, which is a quantitative assessment of the length of crack per unit area, provides a meaningful comparison of the susceptibility of the alloy to HAZ cracking. Where similar alloys are joined using identical welding parameter, the 'Area of HAZ' may be comparable since the welding parameters used are the same. As such, the CI can be substituted with the value of the 'total crack length' (TCL') which is now determined by;

$$TCL' = \sum (l1 + l2 + l3 + \cdots) \quad \text{(2.16)}$$

TCL' is the sum of the individual crack length measured over a constant area of HAZ in welded sample. In order to statistically increase the reliabilities of the TCL' value, the number of section measure for each weld specimen is usually ten (10) or more and the sum of the *TCL'* value and the standard deviation are used for subsequent analyses, that is,

$$TCL = \sum_{n=1}^{10} [TCL'1 + TCL'2 + TCL'3 + \cdots + TCL'10] \quad \text{(2.17)}$$

Some other parameters that can be derived from this method include the number of cracks, maximum crack length (MCL) and average total crack length (ATCL).

2.10 Objectives and Scope of the current research

As previously mentioned, Haynes alloy 282 is a new **γ'** precipitation strengthened nickel-base superalloy, developed to meet the challenges of higher turbine engines service temperature, encountered in power generation and aviation industries. Since its development in 2005, this new alloy has been undergoing evaluation for potential applications in the manufacturing of turbine engine components [2]. Welding as a form of joining technique, plays a crucial role during the fabrication and repair of in-service damaged components of turbine engines. Like other precipitation strengthened nickel-base alloys, Haynes alloy 282 is susceptible to weld cracking, which predominantly occurs in the HAZ. Although some research have been carried out on GTAW, friction stir welding and mechanical properties of Haynes 282 [123 - 126], the factors responsible for

cracking in this new alloy during fusion welding were yet to be reportedly identified prior to the present study. Therefore the present study was initiated with the following two major objectives.

1. to perform a comprehensive and systematic study, involving careful and detailed microstructural examination, analyses and physical simulations, to determine the causes of cracking in the Haynes alloy 282 during LBW.

2. to use the understanding of causes of cracking to develop suitable procedure for preventing or minimizing cracking in the newly developed Haynes alloy 282 during LBW.

Investigations were carried out to

a) characterize the pre-weld microstructure of Haynes alloy 282 in as-received and standard heat treatment (STHT) condition.
b) study the primary cause and factors that aid susceptibility to cracking in this alloy.
c) study the effect of welding heat input on weld cracking in Haynes alloy 282.
d) develop an effective approach for preventing cracking in the alloy through pre-weld microstructural modification; and
e) evaluate the susceptibility of Haynes alloy 282 to cracking during post-weld heat treatment.

CHAPTER 3

EXPERIMENTAL PROCEDURES

3.1 Materials and Processing

3.1.1 As-Received and Pre-weld Heat Treated Haynes Alloy 282.

Wrought Haynes alloy 282 used in this study was supplied by HAYNES International Inc. Kokomo USA in the form of mill bright-annealed plates with dimensions of 610 x 120 x 11.5 mm. The alloy is produced by using a vacuum induction melting and electroslag remelting process to prevent contamination from impurities [9]. The nominal chemical composition of the material (weight %) is 1.5Al, 2.1Ti, 10Co, 20Cr, 8.5Mo, 1.5Fe, 0.3Mn, 0.15Si, 0.06C, 0.005B and balance nickel.

Welding test coupons with a dimension of 65 x 15 x 5 mm were machined by numerically controlled wire electro-discharge machine (EDM). The coupons were then subjected to carefully selected heat treatment cycles as summarized in Table 3-1, by using a Marshal tube furnace connected to a digital programmer. The cooling method used after heating in the furnace varied from water quenching (~ 400^{o}C/s), air cooling (~ 25^{o}C/s) to furnace cooling (~ 0.27^{o}C/s). The heat treatment cycles were performed to aid investigation on various aspects of microstructural variables known to characteristically affect the susceptibility of nickel-base superalloys to weld cracking. Prior to welding, the heat treated welding test coupons were surface ground and polished to remove surface oxide followed by solvent cleaning in an ultrasonic bath.

Table 3 - 1: List of Pre-weld Heat Treatments

Heat Treatment
$1050^{o}C$ - $1150^{o}C$ / 2 hour / WQ $1050^{o}C$ - $1150^{o}C$ / 2 hour / AC $1050^{o}C$ - $1150^{o}C$ / 2 hour / FC $1150^{o}C$/ 2 hour / WQ + $1010^{o}C$/ 2 hour AC + $788^{o}C$/ 8 hour AC (Standard Heat Treatment) Material with refined grain size - $1080^{o}C$/ 2 hour/ FC
AC – Air-Cooled, **WQ** – Water-quenched, and **FC** – Furnace-Cooled.

3.1.2 Laser Beam Welding

Pre-weld heat treated test coupons were welded by bead - on - plate autogenous CO_2 laser beam welding at the Standard Aero Ltd., Winnipeg, by using the parameters shown in Table 3-2. To investigate the effect of laser welding heat input on the extent of HAZ cracking in the new Haynes alloy 282, test coupons were welded using a laser power of 2 kW at welding speed of 1000 mm/min and 2000 mm/min, which correspond to 60 J/mm and 120 J/mm of heat input, respectively, and also referred to as low and high heat input in this dissertation. All laser beam welded coupons were transversely cut to the welding direction into ten sections at intervals of 3 mm by using an EDM.

3.1.3 Hardness Test

The hardness of the as-received and all heat treated samples was determined by using a 10 Kg load on a Vickers hardness testing machine. An average of ten (10) hardness values (VHN) was recorded for each specimen along with the standard deviation. All specimens were properly ground and polished by using standard metallographic techniques before testing.

3.1.4 Gleeble HAZ Simulation and Hot Ductility Test

In order to carefully study non-equilibrium microstructural changes in the HAZ during welding, physical simulation was performed by using a Gleeble 1500-D thermo-mechanical simulator (Figure 3-1) at the University of Manitoba. This was done to enable the examination of a wider HAZ area with a view to understanding the evolution of HAZ microstructure.

Table 3 - 2 Laser Beam Welding Parameters

Heat Input J/mm	Power (kW)	Speed (mm/min)	Beam Focus (mm)	Argon Shielding Gas Flow rate. Litre/min	Helium Welding Gas Flow Rate. Litre/min
80	2	1500	-2	30	25

(a)

(b)

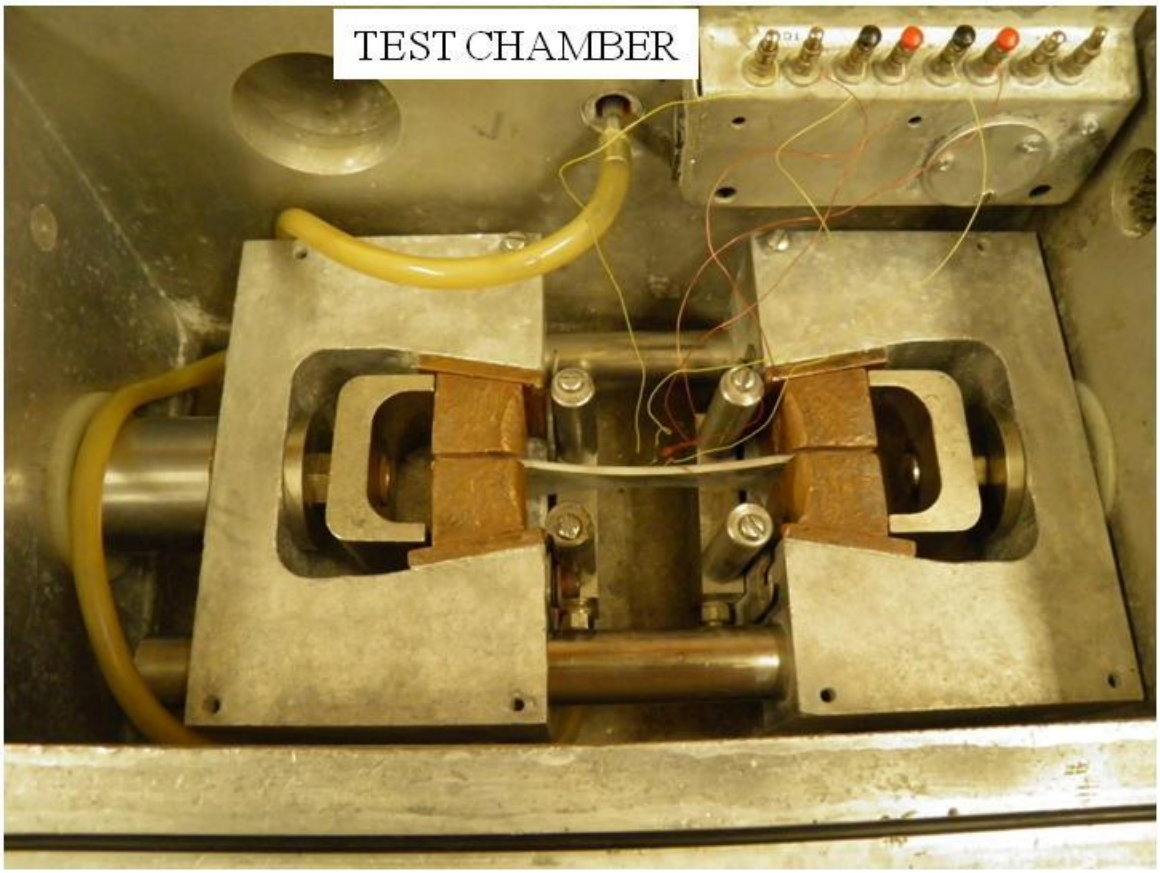

Figure 3-1: (a) Overview of the Gleeble 1500-D test machine at University of Manitoba, (b) Test specimen held between two water cooled cooper jaws and resistance heated by electric current passing through Al-Cr thermocouple wire spot-welded to the specimen.

The simulation was performed in air on test specimens with a dimension of 3 x 3 x 55 mm. A rapid heating rate of 150^{o}C/sec was used to heat the specimens to peak temperatures that ranged from 1050^{o}C to 1200^{o}C and the specimens were held at the peak temperatures for different holding times, followed by water quenching to preserve the microstructural changes that developed at the peak temperatures as much as possible. Specimen temperature was controlled with a chromel-alumel thermocouple that was spot-welded onto the specimen at the mid-section. Furthermore, some Gleeble specimens were pulled to failure at a stroke rate of 50 mm per second to evaluate the hot ductility of the alloy at various peak temperatures and varying holding times. The hot ductility of the alloy at different test temperatures was determined from the reduction in area by measuring the initial and final gauge lengths in regions around the fractured surface with Vernier calipers.

3.1.5 Metallographic Sample Preparation

As-received, pre-weld heat treated, welded and Gleeble simulated specimens were mounted in bakelite, ground and polished by using standard metallographic techniques for microstructural study. The metallographic specimens were chemically etched with modified Kalling's reagent - 40 ml distilled water + 480 ml HCl + 48 gm $CuCl_2$ and electrolytically etched with 10 % Oxalic Acid at 6 V for 3-5 seconds. In addition, specimens used in the electron back scattered diffraction (EBSD) analysis were further polished with 0.5 µm colloidal silica gel in order to produce a smooth surface adequate enough to generate high quality diffraction patterns. The EBSD technique is known to be generally sensitive to surface irregularities.

3.1.6 Optical and Scanning Electron Microscopy (SEM)

The microstructures of as-received, pre-weld heat treated and Gleeble simulated specimens were first examined by using a ZIESS Axiovert 25 inverted-reflected light microscope, equipped with CLEMEX Vision 3.0 image analysis software. A more detailed microstructural study, spectroscopy analysis and fractography examination were carried out by using a JEOL 5900 scanning electron microscope (SEM) equipped with an Oxford (Oxford Instruments, Oxford, United Kingdom) ultra-thin window energy dispersive spectrometer (EDS). The extent of HAZ cracking was determined by measuring the total crack length in ten sections of each welded specimen by using the SEM (operated in both secondary (SE) and backscattered (BSC) imaging modes). The measurement of HAZ and FZ areas were carried out by the optical microscope equipped with Clemex Vision 3.0 image analysis software. Also, the average grain size of the alloy in the as-received and heat treated conditions was measured by using linear intercept method. Optical micrographs were digitally recorded of each specimen at magnifications between 50 X - 200 X on eight to ten areas.

3.1.7 Electron Microprobe Analysis (EPMA)

A Cameca MBX electron microprobe analyzer (EPMA) was used to determine the chemical composition of the dendritic core in the FZ of the welded specimens. The EPMA was equipped with ϕ (p,z) correction algorithm and operated at 15 keV with a beam current of $\leq$ 20 nA, which enabled a good resolution of the dendritic and interdendritic regions from the as-polished specimens. The unique characteristic of the EPMA is its capabilities to determine the composition of particles as small as 1 μm in

diameter within a bulk sample with sufficient accuracy by using the smallest probe size, such that, the volume of the X-ray generation would be slightly less than 1 μm in diameter [127].

3.1.8 Electron Back Scattered Diffraction (EBSD) Analysis

The character of grain boundaries in as-received and solution heat treated conditions was examined by carrying out electron backscatter diffraction (EBSD) based orientation mapping by using an HKL Nordlys EBSD detector (developed by Oxford Instruments), which was attached to a Philips XL 30 SEM. The EBSD detector was equipped with the Oxford Instrument HKL Technology Channel 5 suite of programs. Orientation mapping is a versatile technique for analyzing the grain boundary structures of polycrystalline materials by producing orientation measurements that link local lattice orientation with grain boundary morphology.

The misorientation angle between two grains is usually characterized by the reciprocal of the proportion of shared lattices sites between the adjacent grains, which is called, 'Coincident site Lattice' (CSL). CSL as defined by Kronberg and Wilson [128] is a three-dimensional lattice points created in a region of interpenetration of lattices of two adjoining grains (i.e., crystals) with lattice points common to both. The ratio of the volume of CSL to that of the crystal is designated by the parameter Σ, which can also be considered as the reciprocal density of coincident sites. That is, in a Σ3 grain boundary which is a coherent twin boundary, one-third of the lattice points of inter-penetrating lattice point are coincident. Special boundaries, including twins, are classified as those

within $3 \leq \Sigma \leq 29$ while 'random' high angle boundaries are those with misorientation angles > 10^{o} and CSL boundaries $\Sigma > 29$.

3.1.9 Differential Scanning Calorimetry (DSC)

A DSC study of the new Haynes alloy 282 was performed in argon filled atmosphere by using a NETZCH-404 DSC thermoanalyzer to determine the main equilibrium phase transformation temperatures in this new alloy. EDM sectioned cylindrical specimens with dimensions of 3 x 1 mm and weight of ~ 0.248 g were placed into a pure alumina crucible. The heating and cooling rates used in this study are 1.5 K per minute. Reaction temperatures were determined by finding the temperature at which the DSC curve deviated from the local baseline. The setup was calibrated with pure aluminum, indium, tin, bismuth and gold before the actual test to corroborate sensitivity and deviation from the calibrated temperature profile.

3.1.10 Secondary Ion Mass Spectroscopy (SIMS)

The SIMS technique was used to analyze grain boundary distribution of boron in this study. In SIMS, a solid sample is bombarded with primary ions of a few keV energy. This results in the sputtering of atomic species from the surface of the sample. Fractions of the species are emitted as negative, neutral or positive secondary ions and their mass is analyzed by a mass spectrometer to determine the elemental, molecular or isotopic composition of the surface. Due to the extremely high signal to background ratio of the mass spectrometer, SIMS can detect trace amounts of elements on a surface. It provides

ion images with spatial resolution of a few μm and elemental resolution to a few ppm. The primary ion beam species used in SIMS include Cs+, O2+, O-, Ar+, Ga+ and Xe+. Electronegative elements such as O, S, and P are most sensitive to Cs+ beam, while O2+ is used for most other elements.

In preparation for the SIMS analysis in this study, EDM machined specimens that were 3 mm x 12 mm diameter were heat treated and air-cooled. Thereafter, the heat treated specimens were mounted in bakelite and polished to 0.5 μm finish by using standard metallographic techniques in order to reveal the grain boundaries in an as-polished condition. Figure 3-2 shows a typical as-polished surface of SIMS specimen. The specimens were then carefully removed from the bakelite in which they were mounted followed by solvent cleaning in an ultrasonic bath. The specimens were then sent to Surface Science Western (SSW) at the University of Western Ontario for the grain boundary segregation analysis of B by using a Cameca IMS-3f magnetic sector secondary ion mass spectrometer. The equipment was operated in an ion-microscope mode. A primary ion beam of O2 + with an impact energy of 12.5 kV and 400 nA beam current was rastered over an approximate surface area of 150 μm of the specimen diameter. Mass resolved images of B were obtained by imaging positive secondary ions of 11B+ (mass 43).

3.1.11 Transmission Electron Microscopy (TEM)

Analytical transmission electron microscopy analysis was carried out on thin foils from heat treated and welded specimens by using a field emission gun transmission electron microscope (TEM). The microscope is equipped with an Oxford ultra-thin

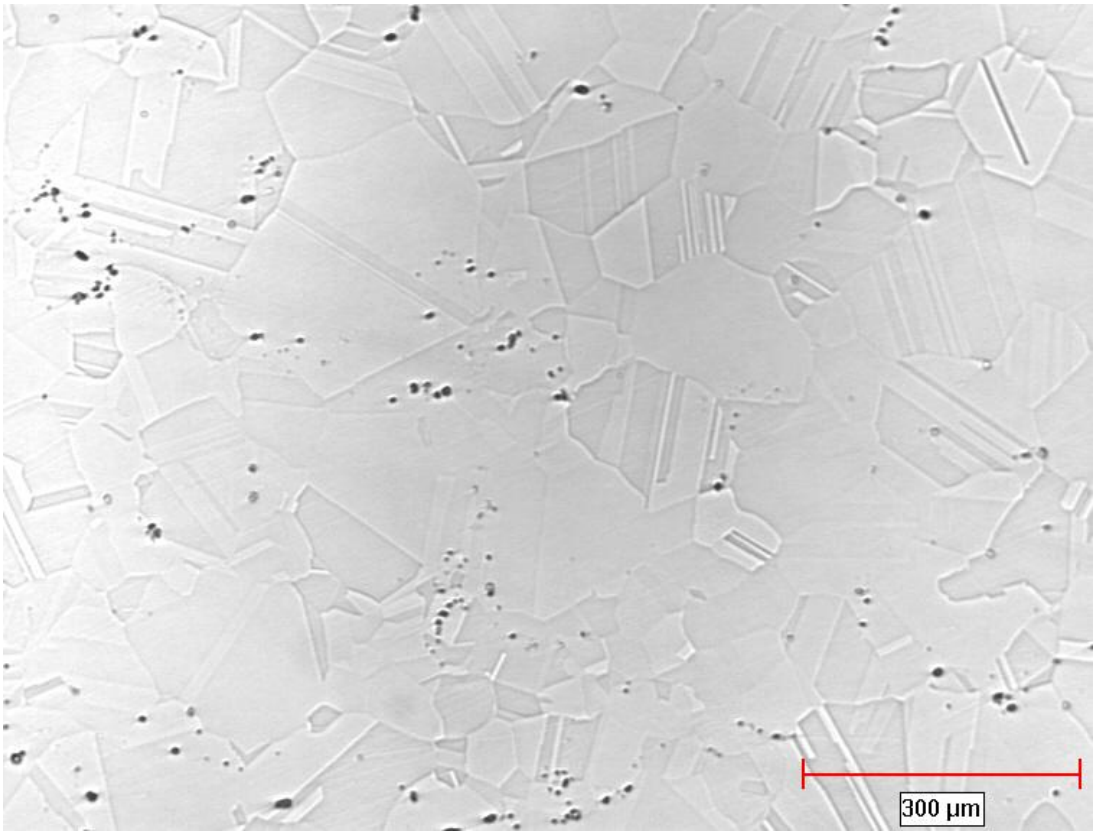

Figure 3-2: A typical as-polished Haynes alloy 282 SIMS specimen

window energy dispersive spectrometer (EDS) and X-Max silicon drift detector. TEM specimens were prepared by electrodischarge machining of 3 mm diameter discs from areas of interest followed by mechanical grinding of the 3 mm diameter discs to ~ 150 μm and then twin-jet electropolishing them in solution of 10% perchloric acid, 30% butanol and 60% methanol at 243 K and 25 V. The electropolishing produced a very thin foil with perforation suitable for transmission electron microscopy examination and analysis.

Selected area diffraction pattern analysis was used to identify the crystal structure of various phases present in the areas of interest on the thin foil. The lattice parameters of the phases were accordingly determined from reflections obtained from the selected area diffraction patterns (SADPs). Semi-quantitative chemical microanalyses were performed with the ultra-thin window Oxford energy dispersive spectrometer (EDS). Raw X-ray data were converted into weight percentages by using theoretical Cliff-Lorimer independent sensitivity factor K_{AB}, which is given by:

$$k_{AB} = (C_A / C_B) \times I_A / I_B \quad \text{.....3.1}$$

where C_A and C_B are the weight percentages of A and B respectively. I_A and I_B are the characteristic X-ray intensities. A major limitation of the EDS system is its reliability in quantifying light elements, and as such, the EDS analyses carried out in the current work are semi-quantitative in nature.

CHAPTER 4

RESULTS AND DISCUSSION

Introduction

The properties and performance of materials depend on their microstructure. The pre-weld microstructures of superalloys are known to play a vital role in determining their performance during fusion welding. In this chapter, the results of the microstructural characterization of the Haynes alloy 282 before welding are presented and discussed in sections 4.1 - 4.3. The results of the study on the cause of weld cracking and development of solution to the cracking problem are presented and discussed in sections 4.4 - 4.5.5.

4.1 Microstructure of As-Received Haynes Alloy 282

Haynes alloy 282 is commercially available in wrought bright mill anneal condition. Figures 4-1a and b show the optical and SEM micrographs of the as-received alloy, respectively. The microstructure consists of gamma (γ) solid solution matrix and MC carbide (M mostly being Ti and Mo) with an average grain size of ~ 140 μm. SEM-EDS semi-quantitative analysis of the MC carbides in the as-received alloy is shown in Table 4-1. The carbide particles present in the alloy have sizes that range from about 2 μm to 15 μm and are randomly dispersed as intergranular and intragranular particles within the γ matrix. MC-type carbides usually form by crystallizing from liquid melt during solidification of the cast ingot [1]. The MC-type carbides have been reported to be metastable in nature with tendency towards dissolution or dissociation during high temperature thermal treatment [1, 27]. The average Vicker hardness of the as-received

(a)

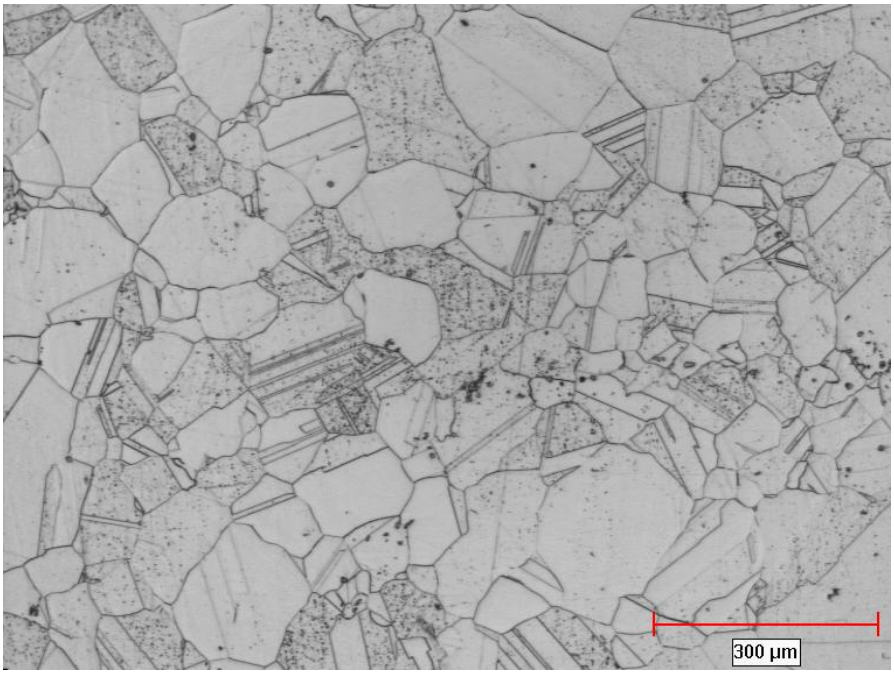

(b)

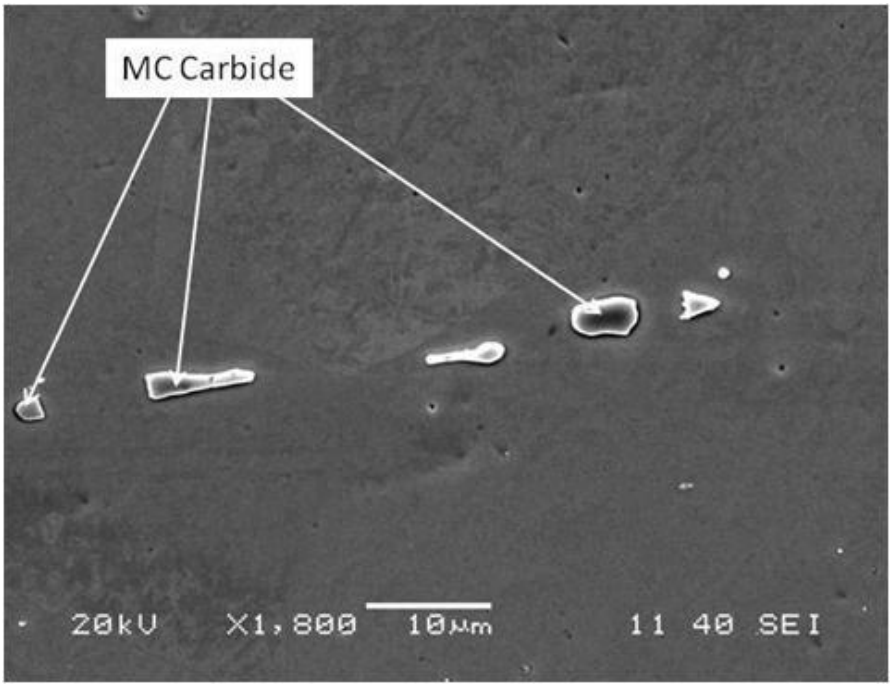

Figure 4-1: (a) Optical micrograph, and (b) SEM micrograph of the as-received alloy showing the MC-carbide particles in b.

alloy is ~ 215 VHN. Nevertheless, the main strengthening phase of the alloy, γ' precipitates, was not observed on the SEM.

4.2 Microstructure of Haynes Alloy 282 in Standard Heat Treated Condition

Figure 4-2a shows a SEM micrograph of the Haynes alloy 282 after being subjected to the recommended standard heat treatment (STHT) for the alloy at 1150^{o}C for 2 hrs + water-quenching followed by aging at 1010^{o}C for 2 hrs + air-cooled + 788^{o}C for 8 hrs + air-cooled. The heat treatment resulted in coarsening of the grains to produce an average grain size of ~ 300 μm (Figure 4-2b). The STHT microstructure consists of intergranular and intragranular primary MC-type carbides that were observed in the as-received material. Fine sub-micron size precipitates were also observed along the grain boundaries and at the phase boundary between the MC carbides and the γ matrix. The principal strengthening phase of the alloy, the γ' precipitates, however, were also not observed by the SEM in the STHTed condition.

The nature of the fine precipitates at the MC/γ interface and along the grain boundaries could not be identified by using the SEM, because of the inherent limitation of the SEM-EDS to reliably analyze sub-micron particles. Therefore, transmission electron microscope (TEM) was used to further study and identify the nature of the intergranular sub-micron particles. Figure 4-3a shows a TEM high angle annular dark field (HAADF) image of the STHT sample and Figure 4-3b presents the results of the TEM-EDS line-scans across the matrix and the intergranular particles as shown in Figure 4-3a.

(a)

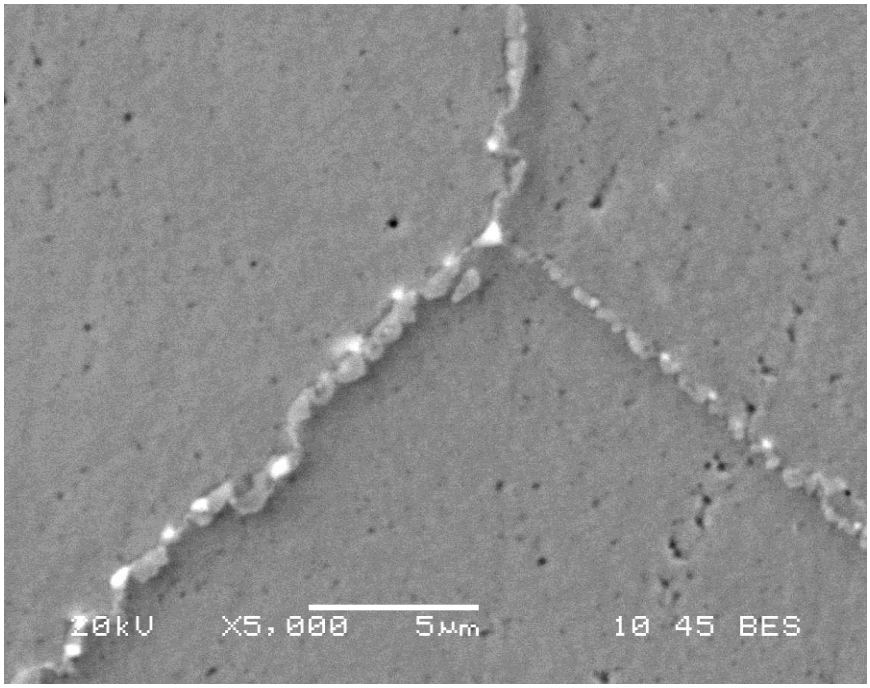

(b)

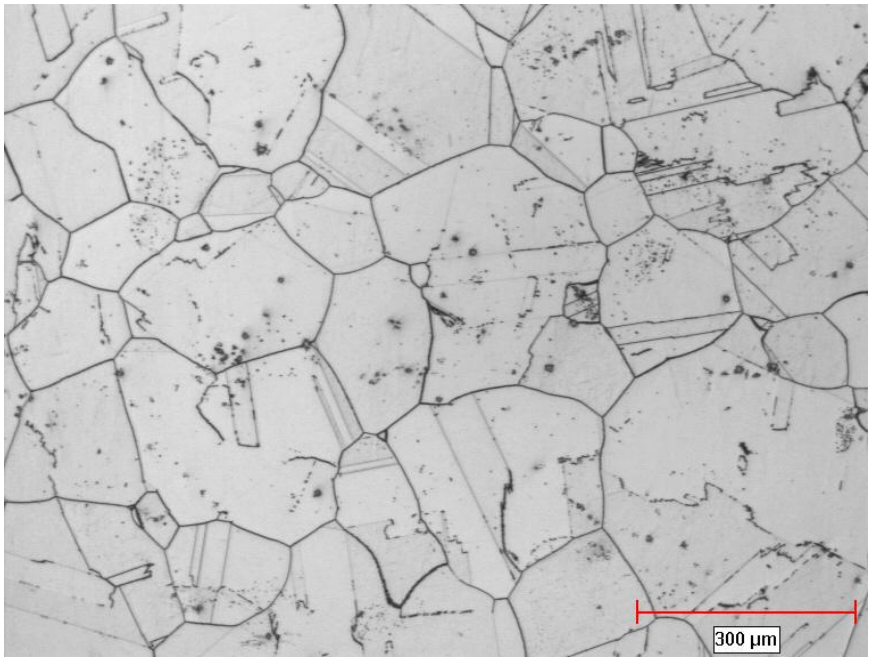

Figure 4-2: (a) SEM micrograph of Haynes Alloy 282 in Standard Heat Treatment (SHTH) condition showing sub-micron intergranular precipitates, and (b) Optical micrograph with an average grain size of ~ 300 µm.

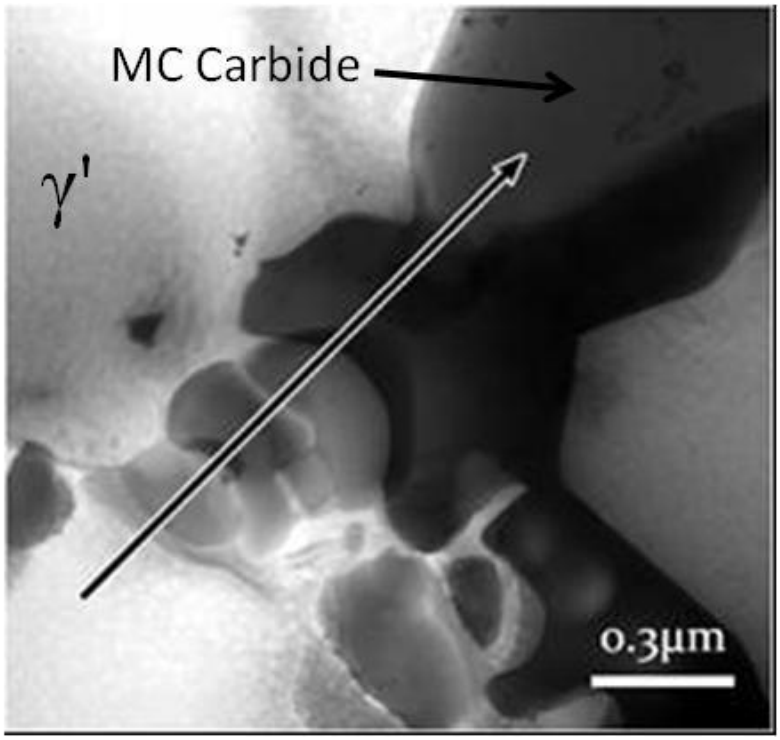

(a)

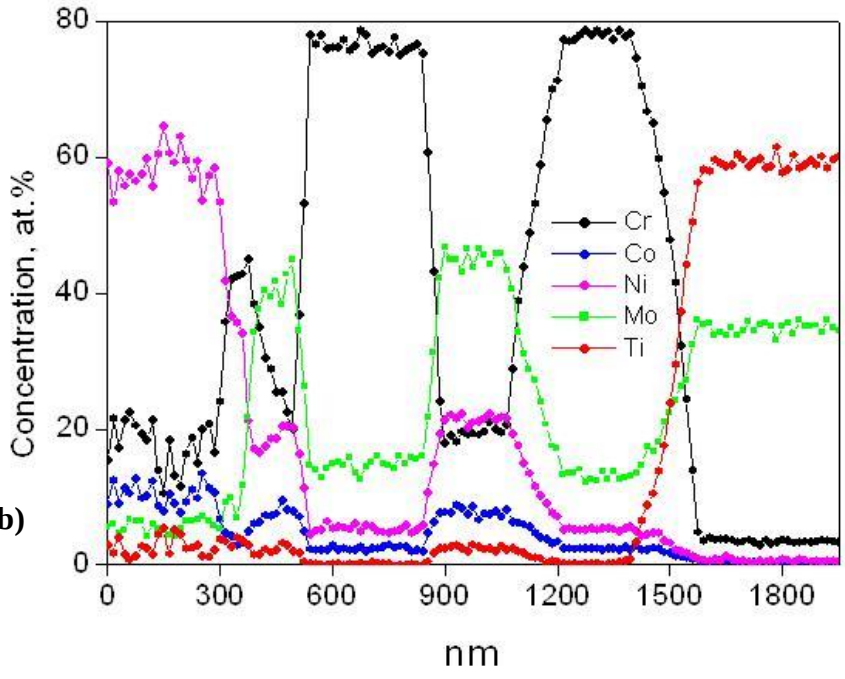

(b)

Figures 4-3: (a) STEM-HAADF image of the intergranular precipitates in standard heat treated Haynes alloy 282, and (b) Results of TEM-EDS line-scans of the intergranular precipitates in Figure 4-3a.

The EDS line-scan results indicate that there are sub-micron microconstituents along the grain boundary, which consist of Cr-rich and Mo-rich particles (Figure 4-3b and Table 4-1). An electron diffraction analysis was performed to determine the crystal structure of the Cr-rich and Mo-rich particles. Analysis of the selected area diffraction patterns (SADPs) obtained from different zone axes of the Cr-rich phase (Figures 4-4) indicate that the particles are FCC $M_{23}C_6$ carbides with a lattice parameter a = 1.06 nm. This type of carbides has been reported in nickel-base superalloys and are known to form by precipitation reaction from carbon-supersaturated γ matrix during the aging heat treatment (750^{o}C - 1055^{o}C) that normally follows solution treatment [1, 21, 27] i.e.,

$$\gamma \Longleftrightarrow M_{23}C_6 + \gamma \quad \text{..... (4.1)}$$

It has been also reported that they could likewise form by a phase reaction between MC-type carbides and the γ matrix [1] via the following type of phase transformation reaction;

$$\gamma + MC \Longleftrightarrow M_{23}C_6 + \gamma' \quad \text{..... (4.2)}$$

The $M_{23}C_6$ particles formed by this second reaction are located in the vicinity of degenerated MC particles. A typical TEM-EDS spectrum from Mo-rich particles (Figure 4-5) shows boron peak, which suggest that the Mo-rich particles could be borides. Figures 4-6 show SADPs obtained from different zone axes of the Mo-B rich particles. The analysis of the diffraction patterns showed that the particles are tetragonal (BCT) M_5B_3 boride with lattice parameters a = 0.56 nm, c = 1.01 nm and c/a = 1.83. This type of phase, M_5B_3 boride, has not been previously reported in Haynes alloy 282.

It has been proposed that the addition of boron to nickel-base superalloys can

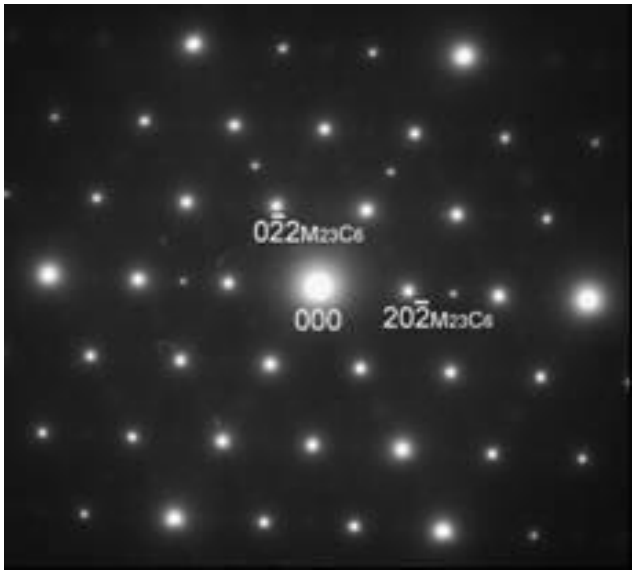

(a)

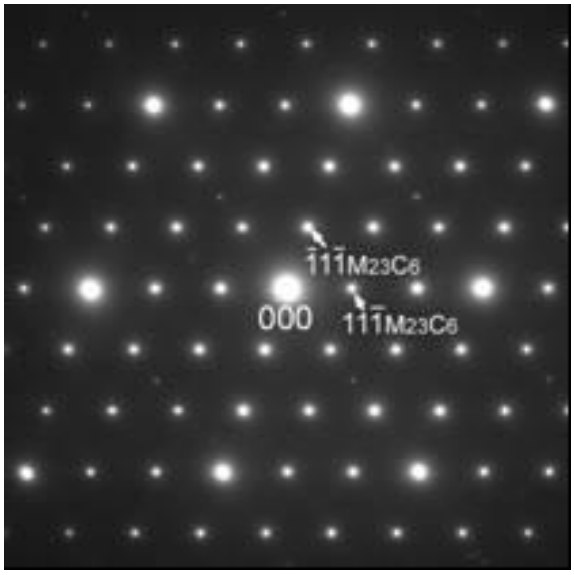

(b)

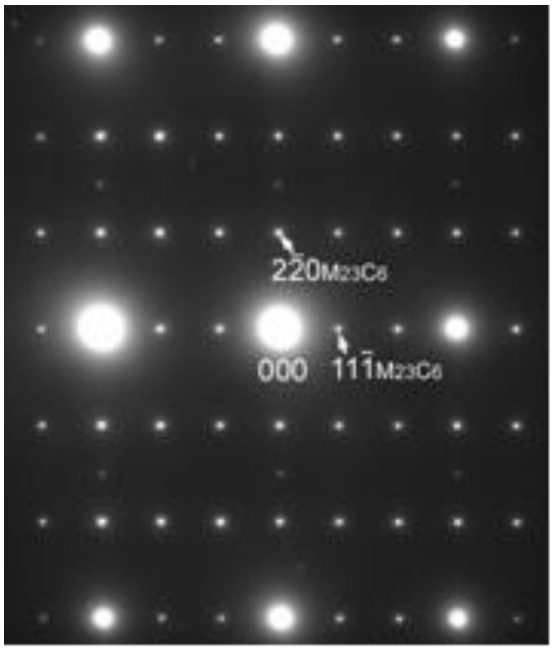

(c)

Figure 4-4: SADP from (a) [111], (b) [011] and (c) [112] zone axes of the $M_{23}C_6$ carbide in STHTed Haynes alloy 282.

Table 4-1: EDS semi-quantitative chemical composition analysis (wt. %) of metallic element in phases present in the as-received and standard heat treated Haynes alloy 282.

Secondary Phases	Elements								
	Ti	Mo	Cr	Al	Co	Mn	Si	Fe	Ni
*MC Carbide	63.13	29.25	2.31	-	0.29	-	0.05	0.04	1.93
MC Carbide	60	34.87	2.95	-	0.43	0.03	0.51	0.46	0.60
Cr-rich Phase	-	15.01	76.26	0.11	2.49	0.19	0.29	0.52	5.14
Mo- rich phase	2.86	42.95	22.65	1.22	7.44	-	1.64	0.41	20.83

* As-Received

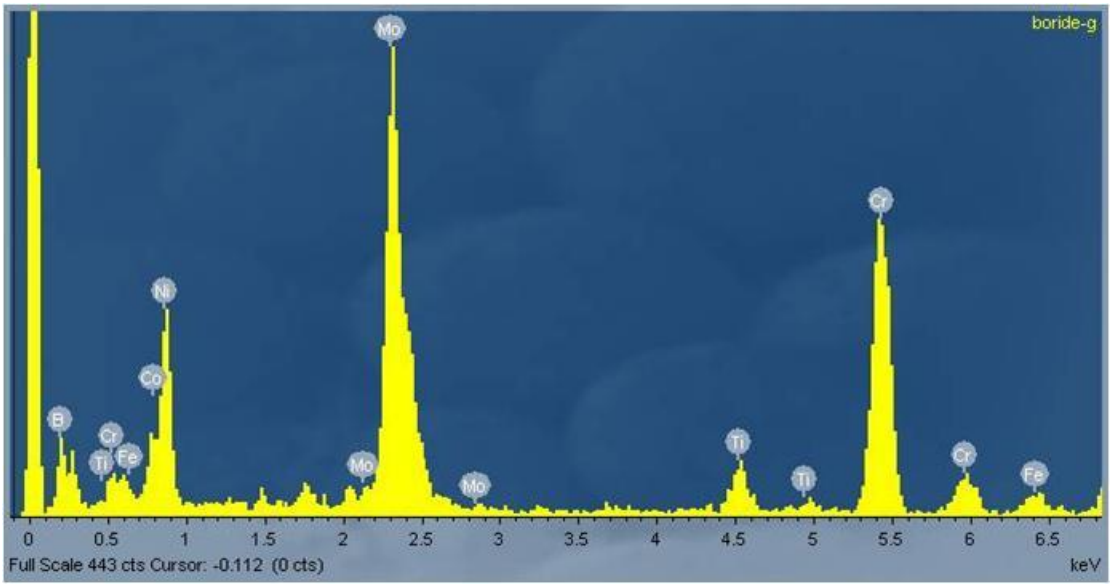

Figure 4-5: TEM-EDS spectrum of the Mo- rich phase, which also shows boron peak.

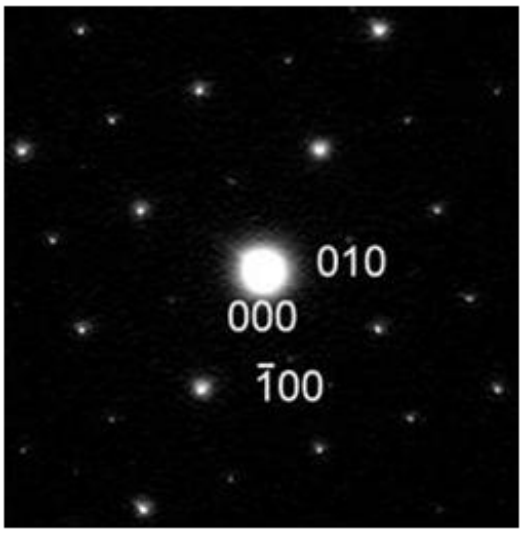

(a)

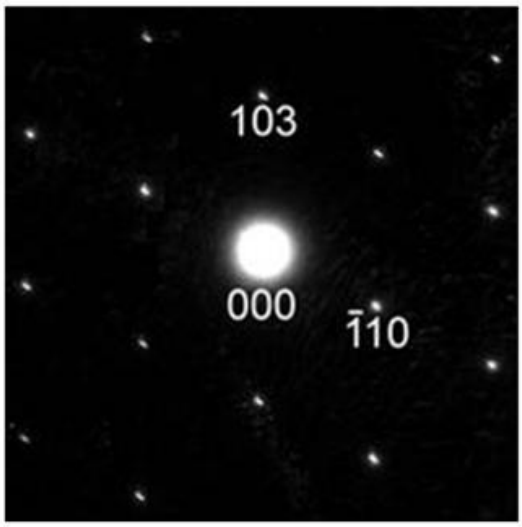

(b)

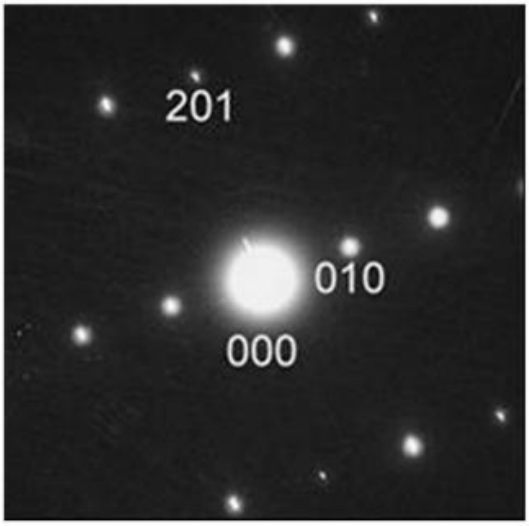

(c)

Figure 4-6: SADP from (a) [001], (b) [$\bar{3}$ $\bar{3}$1] and (c) [$\bar{1}$02] zone axes of the M_5B_3 boride in STHTed Haynes alloy 282.

influence the structure and chemistry of grain boundary precipitates [129-130]. The solid solubility of boron in austenitic (γ) alloys is very low. For example, Goldschmidt [131] reported a maximum solubility of 97 ppm of B at 1125^{o}C in 18% Cr – 15% Ni stainless steel. The solubility decreases rapidly with decreasing temperature and becomes less than 30 ppm at 900^{o}C. Furthermore, the size of boron atom is larger than the common interstitial elements in nickel (e.g. C) and smaller than substitutional elements, such as Co and Cr. The size misfit of boron atoms for both the substitutional and interstitial sites in austenitic lattice implies that it would be energetically favorable for boron atoms to segregate to loosely packed regions like grain boundaries and other incoherent phase boundaries. Interfacial segregation of boron has been experimentally observed in a number of superalloys and austenitic alloys [93, 96, 132].

A grain boundary characterization study of boron segregation in an austenitic alloy by secondary ion mass spectroscopy, has, however, indicated that during heat treatment, boron tends to have stronger affinity for partitioning into second phase particles rather than remaining in solid solution form on grain boundaries [31, 93, 96, 98, 129, 131]. This may explain the formation of M_3B_5 boride particles observed in the standard heat treated Haynes alloy 282. Furthermore, the analysis of diffraction patterns obtained from the Ti-rich particles observed along the grain boundary in Figure 4-3a shows that the particles are FCC MC - carbide with lattice parameter a = 0.428 nm (Figure 4-7).

The γ’ precipitates, which could not be observed by the SEM, were revealed by the TEM (HAADF image in Figure 4-3a and dark field image in Figure 4-8a). An SADP taken from the [112] zone axis of the γ matrix (Figure 4-8b) shows strong superlattice

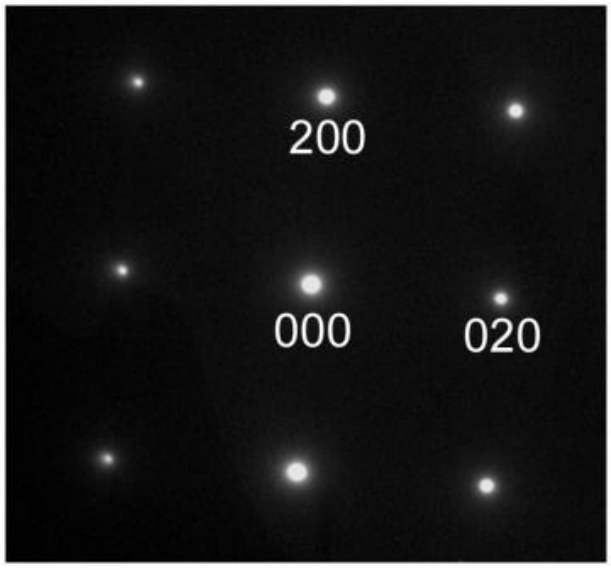

(a)

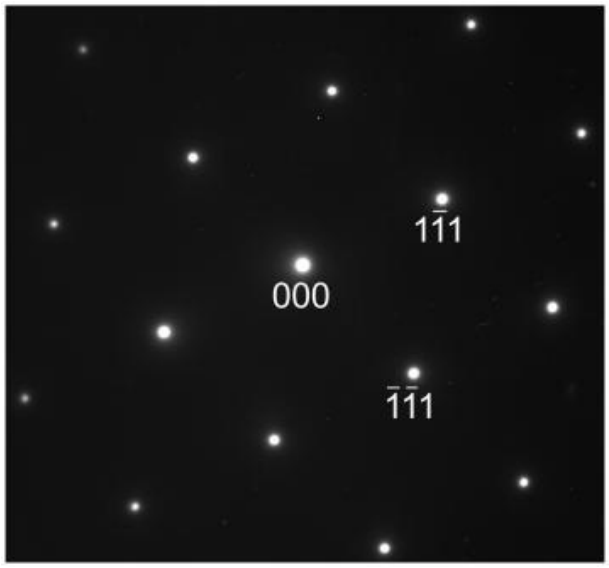

(b)

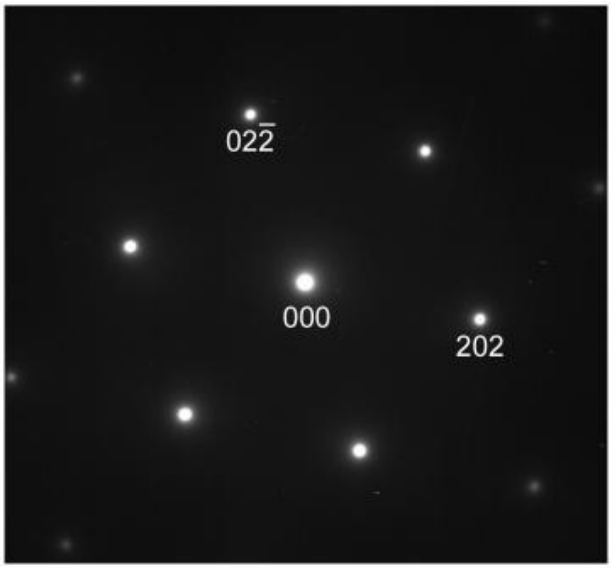

(c)

Figure 4-7: SADP from (a) [001], (b) [011] and (c) [$\bar{1}$11] zone axes of the MC carbide in STHTed Haynes alloy 282.

(a)

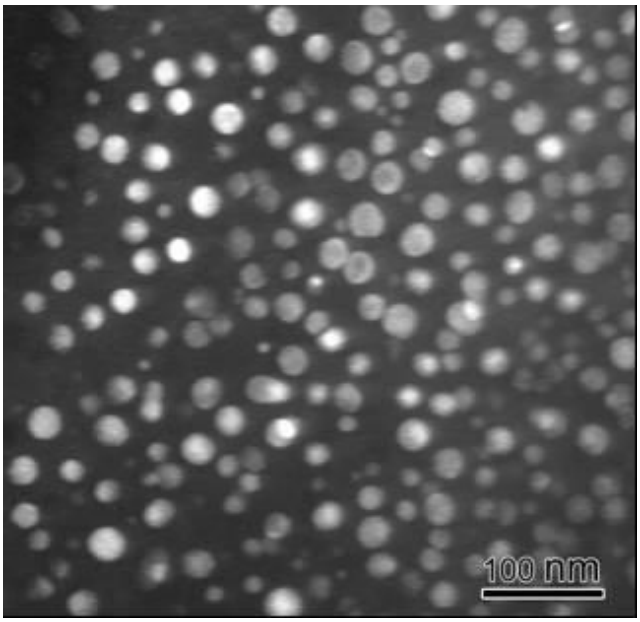

(b)

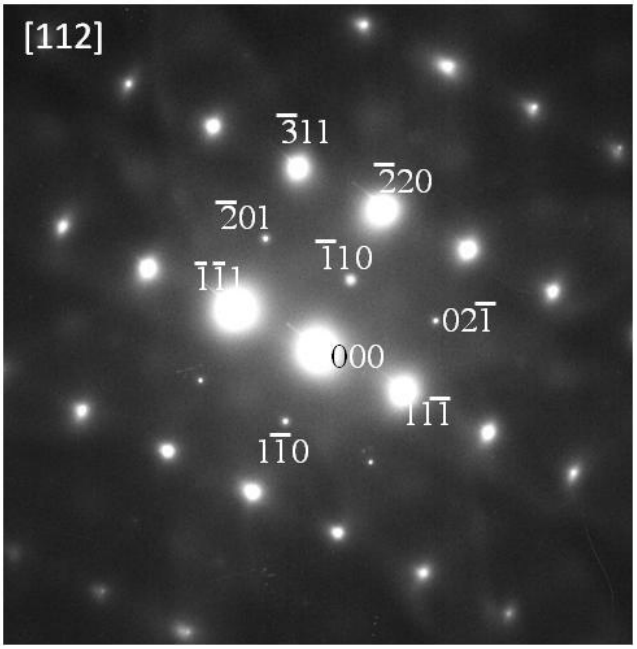

Figure 4-8: TEM (a) Dark field image of γ' particles obtained using $(\bar{1}10)$ superlattice reflection, and (b) [112] SADP showing the presence of superlattice reflections typical to $L1_2$ ordered lattice of γ' phase in STHTed Haynes alloy 282.

reflection of the γ' phase. Although the γ' precipitates could not be observed in the standard heat treated condition (involving rapid-cooling) by using the SEM, when the alloy was furnace (slow) cooled from the heat treatment temperatures, the γ' precipitates coarsened, and were conspicuously revealed by the SEM (Figure 4–9a and b). The γ' precipitates, observed in the furnace cool specimen, are spherical in shape and were uniformly distributed in the gamma (γ) matrix with an average particle size of ~ 160 nm.

4.3 Differential Scanning Calorimetry (DSC) Analysis

The dissolution temperature of the main strengthening phase of the alloy, γ' precipitates as well as the equilibrium solidus and liquidus temperature of the alloy were determined by DSC. Figure 4-10 shows a typical DSC curves obtained from the heating and cooling cycles of Haynes alloy 282. Major equilibrium phase transformation temperatures in the alloy were determined by the deviation (inflection) point from calibrated baseline. The results of the DSC study, as determined by using the average from three different test specimen conditions and 1.5 K/minute heating/cooling rate are summarized in Table 4-2. The γ' phase solvus temperature was determined from the analysis to be ~1000^{o}C. This is consistent with the value reported by others, 997^{o}C [2].

Further metallographic study, on the effect of heat treatment temperature on the dissolution behavior of the γ' particles showed that the particles completely dissolve after 1 hour holding at 1000^{o}C. TEM examination of the specimens air-cooled after heat treatment at 1000^{o}C for 1 hour revealed that the γ' particles re-precipitate (Figure 4-11) during air-cooling from the heat treatment temperature. This result indicates that the rate

(a)

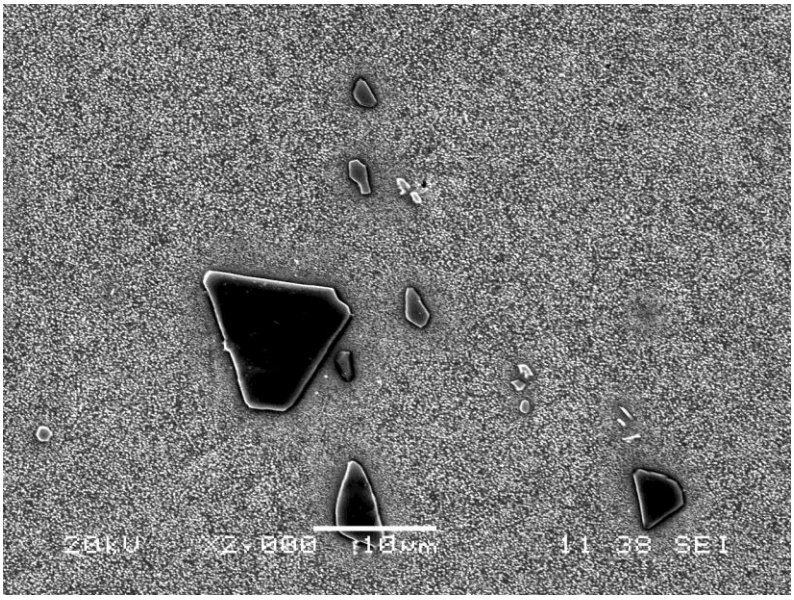

(b)

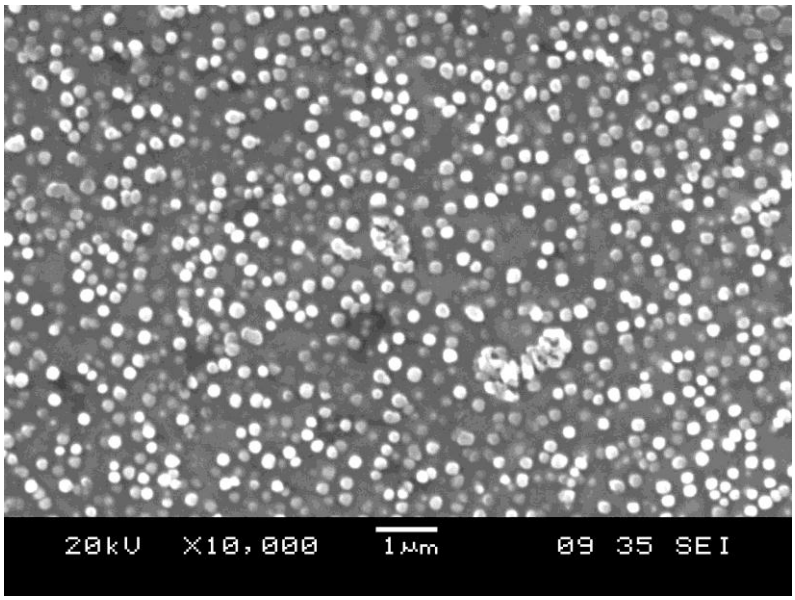

Figure 4-9: SEM micrographs of furnace cooled Haynes alloy 282 (a) at low magnification and (b) at higher magnification showing the spherical shaped γ' precipitates.

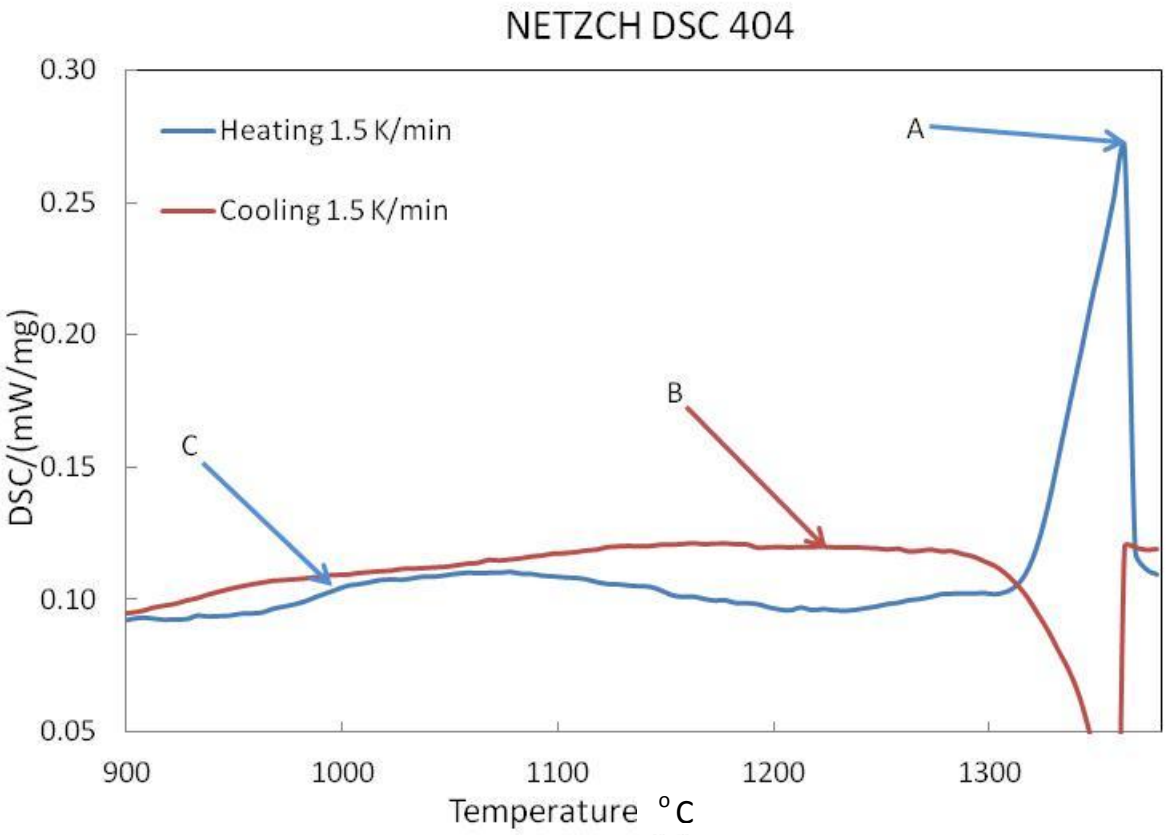

Figure 4-10: Typical DSC curves of on-heating and on-cooling thermo-gram of Haynes alloy 282 showing transformation temperatures, A - Liquidus, B - Solidus and C - γ' solvus.

Table 4 - 2: DSC Phase Transformation Temperatures in Haynes alloy 282.

Reaction	Transformation temperature +/-5 ^{o}C
Liquidus	1360^{o}C
Solidus	1244^{o}C
γ' Solvus	1000^{o}C

(a)

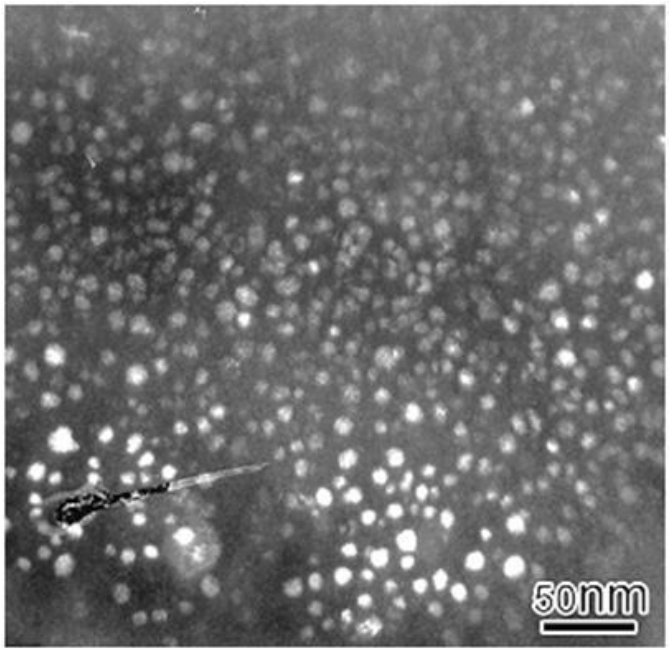

(b)

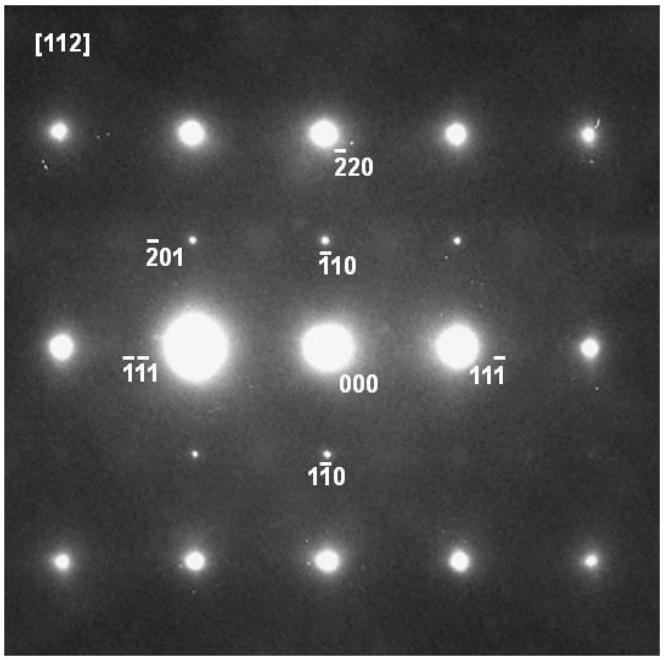

Figure 4-11: TEM (a) Dark field image of γ' particles obtained using $(\bar{1}10)$ superlattice reflection, and (b) [112] SADP showing the presence of superlattice reflections typical to $L1_2$ ordered lattice of γ' phase in SHT material.

of precipitation of γ' precipitates in the alloy is quite rapid.

4.4 General Microstructure of the Laser Weld Region

Low magnification optical and SEM micrographs of a typical autogenous laser beam weld region that show the FZ and HAZ are presented in Figures 4-12a and b, respectively. No exclusive FZ crack can be observed in all of the weldments and this is typical of welded specimens examined in the current work irrespective of heat input parameters and pre-weld heat treatment condition. Detailed analyses of the FZ and HAZ are presented and discussed in the following sections.

4.4.1 Weld Fusion Zone Microstructure

A study of the microstructural development within the FZ during weld solidification is paramount to a proper understanding of the cause of defects formation or their absence and the consequent weld-metal properties. Dendritic microsegregation is known to often result in the formation of intermetallic secondary solidification constituents along dendrite interstices as well as inhomogeneous distribution of second phase precipitate particles [133-134]. In some cases, important strengthening elements may be tied up in the resultant non-equilibrium intermetallic particles, which could also exhibit other damaging effects on high temperature performance [134]. Therefore, an investigation was carried out to determine elemental microsegregation patterns and ensuing solidification reaction microconstituents within the FZ of Haynes alloy 282 laser weld with a view to understand why there is no FZ cracking in this new alloy despite its

(a)

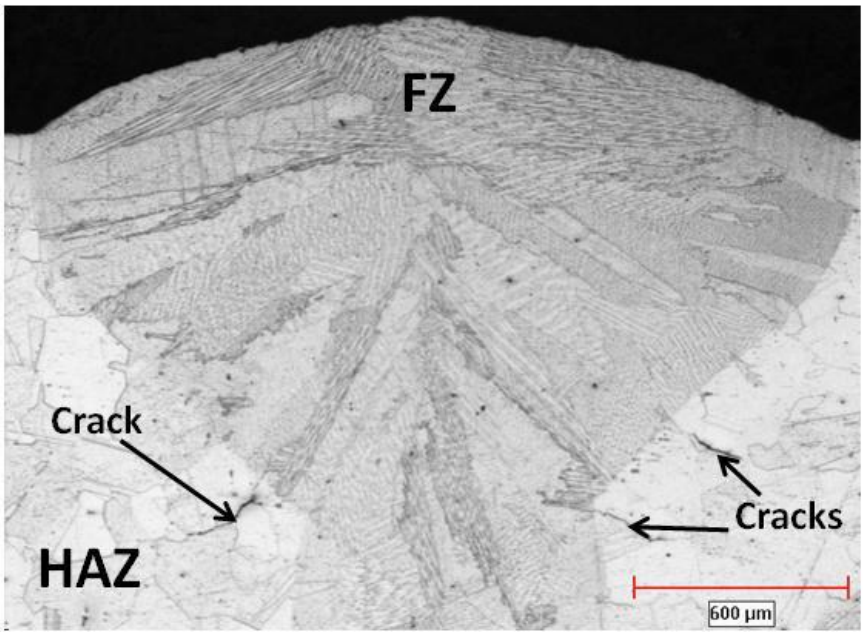

(b)

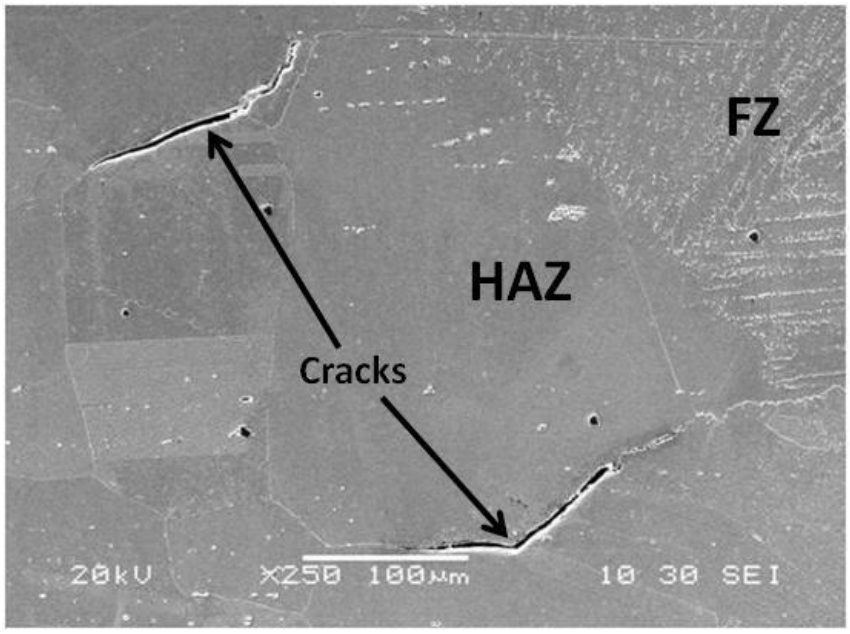

Figure 4-12: Low magnification micrographs showing FZ and HAZ with cracks in the HAZ in (a) optical and (b) SEM.

common occurrence during welding of many other precipitation strengthened nickel-base alloys.

Figure 4-13a shows a high magnification optical image of the FZ that consists of cellular dendritic microstructure formed by epitaxial growth from the fusion boundary. An SEM micrograph (Figure 4-13b) of the FZ showed that the FZ consist of γ dendrites and solidification products along the interdendritic regions with very few large primary MC carbides that appear to have survived above liquidus temperature without melting. The surviving large carbides are few in number, and can be easily distinguished from solidification microconstituents.

According to Liu et al. [135], primary MC type carbides can survive in molten weld metal pool for up to 5-10 minutes during the heating portion of the welding thermal cycle. The epitaxial growth from the fusion boundary and the fine cellular dendritic microstructure observed in Figure 4-17 can thus be rationalized on the basis of the thermal gradient (G) and the cooling rate during weld solidification. It is widely accepted that the thermal gradient (G) in a weld pool is steeper at regions close to the fusion boundary than in the weld interior and as such, the degree of undercooling in a solidifying melt has been estimated to be inversely proportional to the growth rate, i.e. G/R [37, 39] where R is the growth rate of solidification. Therefore, cellular dendritic growth, in the direction opposite to the heat extraction is favored because of steep thermal gradient close to the fusion boundary.

(a)

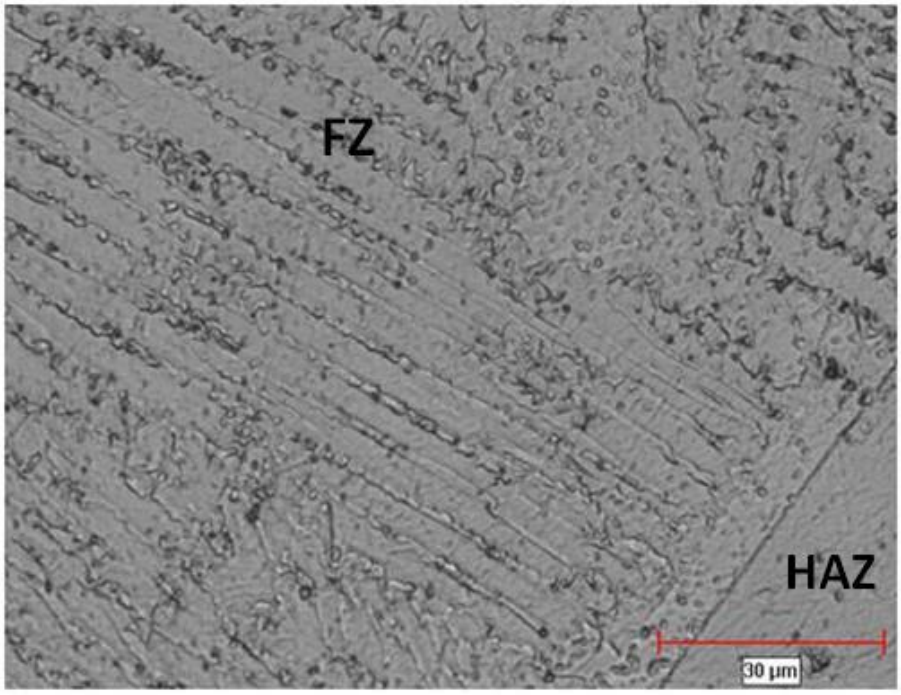

(b)

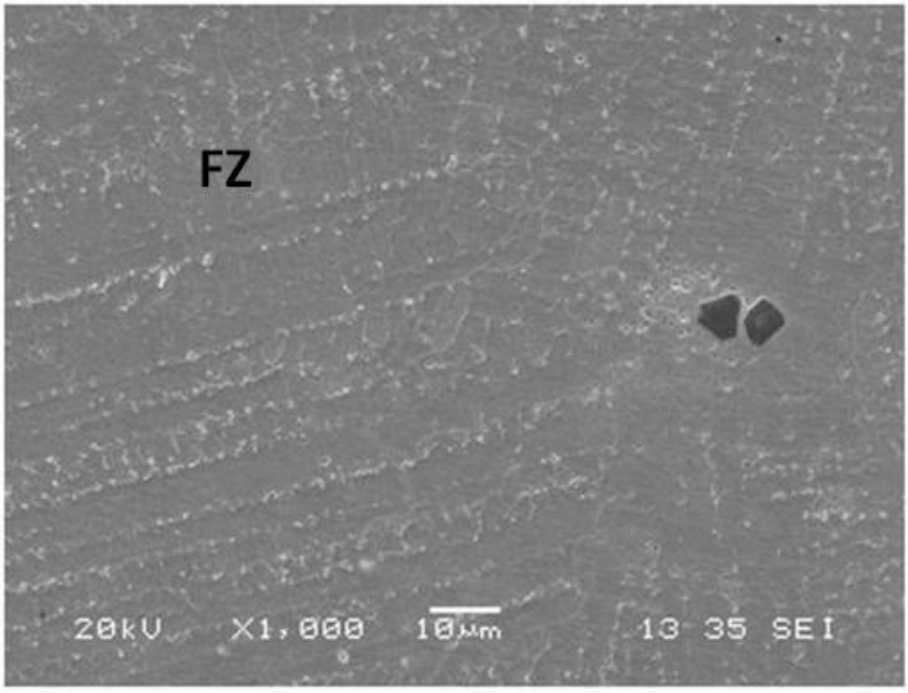

Figure 4-13a and b: High magnification micrographs of FZ in a) optical and b) SEM showing surviving MC carbide in b.

4.4.2 Electron Microprobe Analysis of Fusion Zone Microstructure

As earlier mentioned and shown in Figure 4-13, no evidence of FZ solidification cracking was observed in any of the laser beam welded specimens. The FZ consists of a cellular-dendritic microstructure with an average secondary dendrite arm spacing, λs, of about ~ 3.1 +/- 0.6 μm. Secondary dendrite arm spacing is known to generally follow an equation of the type [136]

$$\lambda s = k_s \Theta^n \quad \ldots\ldots\ldots\ldots\ldots\ldots\ldots\ldots\ldots\ldots\ldots\ldots\ldots\ldots\ldots\ldots\ldots\ldots \quad (4.3)$$

where Θ is the cooling rate, and k_s and n are constants. Using the values of $k_s = 4.7 \times 10^{-2}$ $mmK^{1/3}s^{-1/3}$ and n = -0.4, as experimentally determined by another researcher in a nickel-base superalloy [136], the cooling rate within the FZ in the Haynes alloy 282 is computed to be ~ 1168 K/s, which falls within the range of 573 – 1273^{o}C/s that is reported for 12% Cr steel welds by solving Rosenthal's heat conduction equation [36]. The chemical composition within the dendrite core regions as determined by X-ray microanalysis by using EPMA/WDS is given in Table 4-3. According to the solute redistribution model developed by Brody and Flemings [137], solute concentration in the solid at the solid-liquid interface (C_s) for a parabolic dendritic growth rate is given by:

$$C_s = k\,(Co\,[1 - (1-2\alpha k)\, f_s]^{(k-1)/(1-2\alpha k)} \quad \ldots\ldots\ldots\ldots\ldots\ldots\ldots \quad (4.4)$$

$$\alpha = D_s t_f \,/\, L^2 \quad \ldots\ldots\ldots\ldots\ldots\ldots\ldots\ldots\ldots\ldots\ldots\ldots\ldots\ldots \quad (4.5)$$

where k is the equilibrium solute distribution coefficient, Co is the nominal solute concentration, f_s is the fraction of the solid, Ds is the diffusivity of the solute in the solid (assumed to be constant), t_f is the local solidification time, L is half the dendrite arm

Table 4-3: Chemical composition (wt %) of dendrite core and calculated equilibrium partition coefficient (*k*)

Elements	**Al**	**Cr**	**Mo**	**Ti**	**Co**	**Ni**
Dendrite Core	1.47	19.89	7.90	1.71	10.58	58.59
$\boldsymbol{k} = C_s / C_o$	0.98	0.99	0.92	0.82	1.05	1.03
Note: a) C_s – Dendrite core composition b) C_o – Nominal solute concentration						

spacing and α is a dimensionless back-diffusion parameter. If solid-state solute diffusion is negligible, such that $\alpha << 1$, Brody and Fleming's equation reduces to the well known Scheil equation [138], i.e.:

$$C_s = k\, C_o\, [1- f_s]^{(k-1)} \quad \ldots\ldots (4.6)$$

As stated earlier, estimated cooling rate within the FZ in the present work was about 1168 K/s. Such a rapid cooling rate could appreciably limit the extent of solute back-diffusion during the weld-metal solidification. Moreover, it has been also reported that the diffusion of substitutional alloying elements in γ austenite during solidification conditions typical of fusion welding is negligible [139]. Therefore, equation (4.6) can be reasonably used to estimate the solute distribution coefficient, k. Neglecting undercooling at the dendrite tips under local equilibrium condition at the start of solidification when $f_s = 0$, the first solid to form from the liquid, which is the dendrite, will have a composition of kC_o. The ratio of the dendrite core composition to the nominal composition, C_s/C_o, will thus yield the distribution coefficient of an element at the beginning of the weld solidification process.

The initial partition coefficients at the start of solidification of the major metallic alloying elements in Haynes alloy 282; Ti, Co, Cr, Mo, and Al were computed and are listed in Table 4-3. The results show that only Ti, and to a lesser extent, Mo, exhibited appreciable micro-segregation into the interdendritic region, while Co, Cr and Al are distributed in a nearly uniform fashion between the dendrite core and interdendritic regions. The partition coefficient of boron and carbon could not be determined in the present work due to the difficulty in quantifying these light elements with sufficient

accuracy, and the fact that the effect of back-diffusion of interstitial elements can be significant during solidification. The binary Ni-C phase diagram indicates that the value of k for C and B in nickel is less than one [140]. It has been suggested by Knorovsky et al [141] that the distribution coefficient of carbon in alloys similar to a nickel-base superalloy IN 625 is approximately 0.2. Also, Thompson et al [142] in their study on another nickel-base superalloy, IN 718, experimentally confirmed by Auger electron spectroscopy that carbon segregates into interdendritic liquid during solidification. Therefore, it is reasonable to assume that during weld solidification of Haynes alloy 282, an extensive segregation of C atoms would occur into the interdendritic liquid. It is, nonetheless, worthwhile to note that the partition coefficients are not necessarily constant during the solidification process, but they explain well the formation of interdendritic microconstituents, as would be discussed in the next section. In addition, in the case of solute build-up at the dendrite tips, the initial solid to form will have a higher concentration of solutes (compared to the case of no solute build-up as assumed in the present approach), which could lead to a higher value of k. Hence, the k values reported in this work provide an upper bound when $k < 1$.

4.4.3 Secondary Solidification Microconstituents in the Fusion Zone

As previously discussed in section 4.4.1, a higher magnification SEM micrograph of the laser weld FZ microstructure is shown in Figure 4-14. The interdendritic region of the laser weld fusion zone microstructure consists of discrete irregular shaped second phase particles. A preliminary SEM/EDS micro-chemical line scan analysis of the interdendritic particles showed that they are rich in Ti, Mo and C (Figure 4-15a). In order

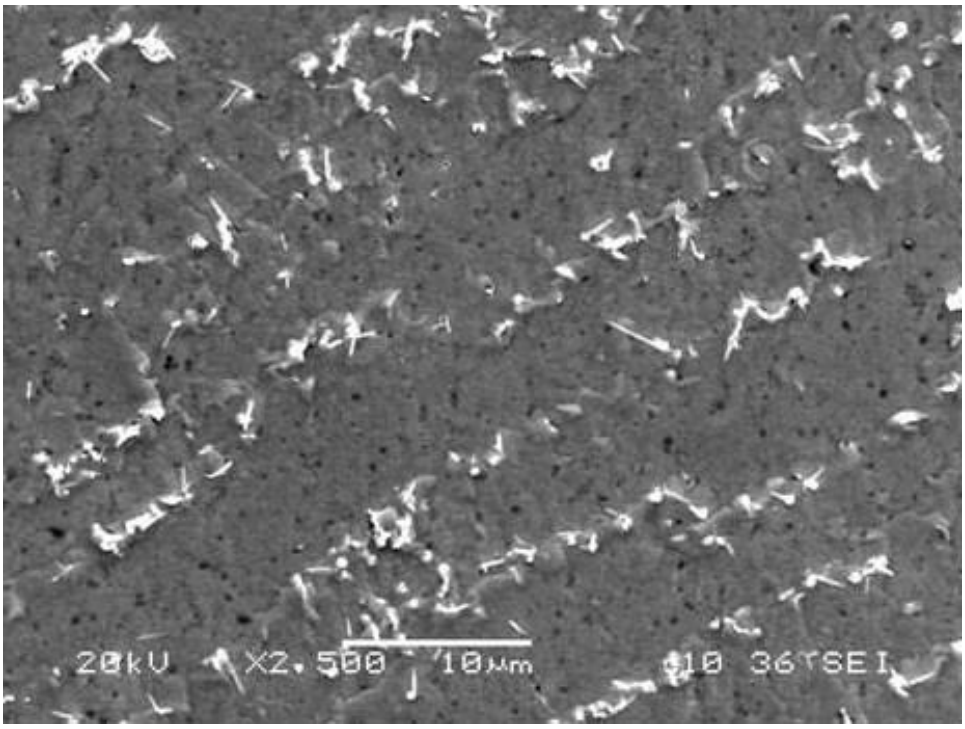

Figure 4-14: High magnification SEM micrograph of the FZ microstructure

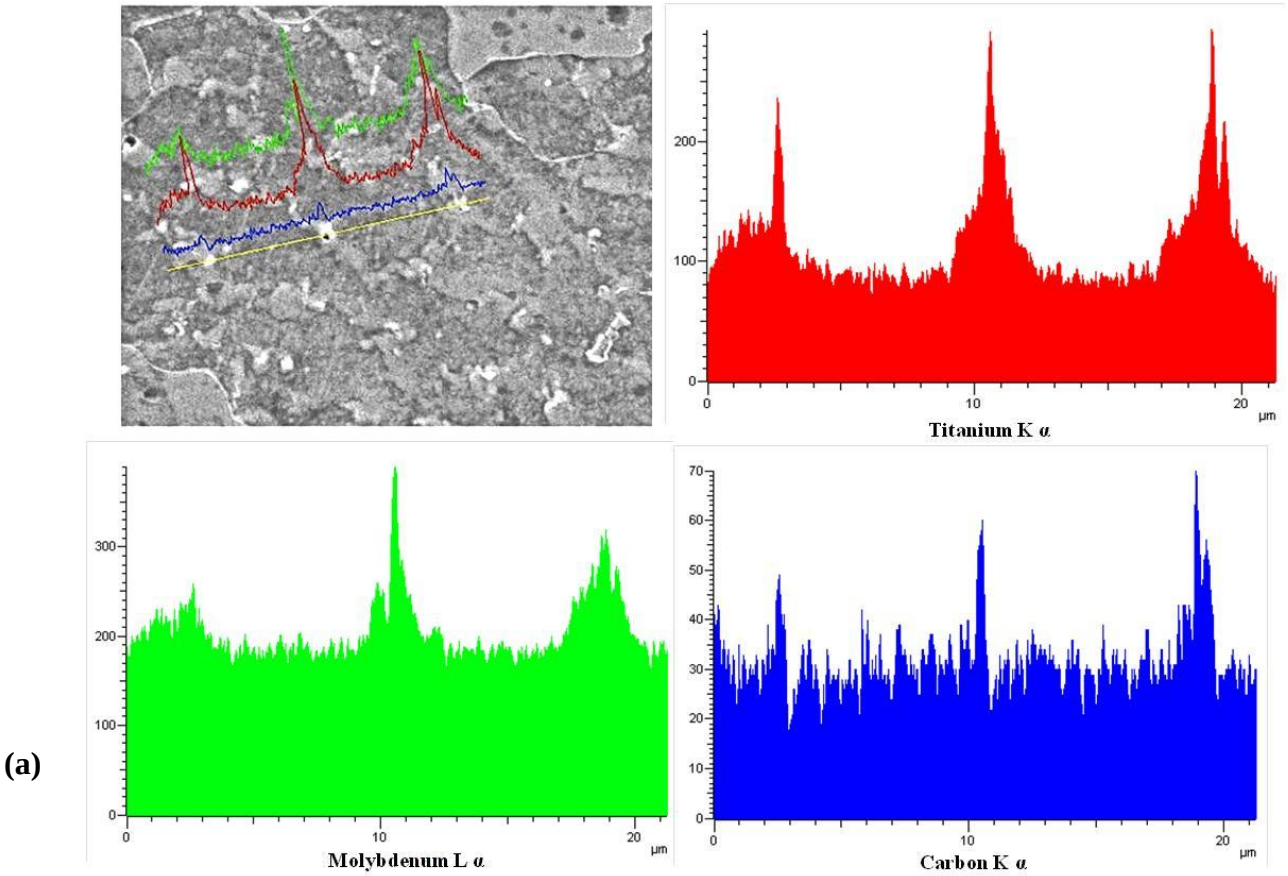

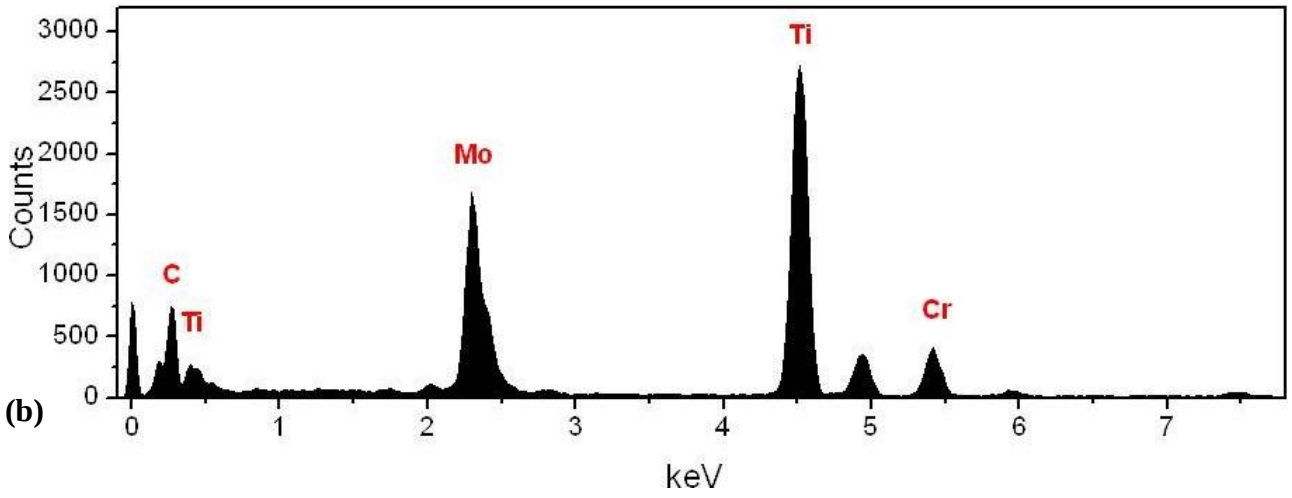

Figure 4-15: (a) SEM-EDS line-scans analyses across the fusion zone interdendritic particles, and (b) TEM-EDS X-ray spectrum of the interdendritic particles

to positively identify the particles, which could not be achieved by using the SEM. Transmission electron microscopy (TEM) analysis of the particles, was performed. The TEM/EDS X-ray microanalysis of the FZ interdendritic region confirmed that they are rich in Ti, Mo and C as shown in Figure 4-15b. Selected area diffraction patterns (SADPs) were obtained from different zone axes of the particles (Figure 4-16) in order to determine and analyze their crystallographic structure. Careful analysis of the SADPs showed that the particles are Ti-Mo based MC-type carbides with an FCC crystal structure and a lattice parameter of 0.436 nm. The TEM study did not reveal formation of γ' precipitates within the FZ microstructure and SADPs did not show any superlattice reflection of the γ' phase. A typical example is shown in Figure 4-17, where SADP from [101] zone axis does not contain γ' superlattice reflections. Likewise, γ-γ' eutectic microconstituents, which have been reported to form in the interdendritic regions of γ' precipitation nickel-base superalloys and sometimes associated with solidification cracking in these materials, were also not observed in the weld FZ microstructure of Haynes alloy 282.

4.4.4 Discussion on Microstructural Development in the Weld Fusion Zone.

Radhakrishnan et al. [63] and Dupont et al. [143] have used the liquidus projection of the nickel-rich region of Ni-Nb-C ternary system to describe solidification sequence in Nb-bearing nickel-base superalloys. Ojo et al. [71] likewise adapted the liquidus projection of the nickel- rich region of the Ni-Ti-C ternary system, as estimated by Backerud et al [144], to describe solidification microstructures in γ' precipitation strengthened nickel-base superalloys. A schematic of the pseudo-ternary solidification

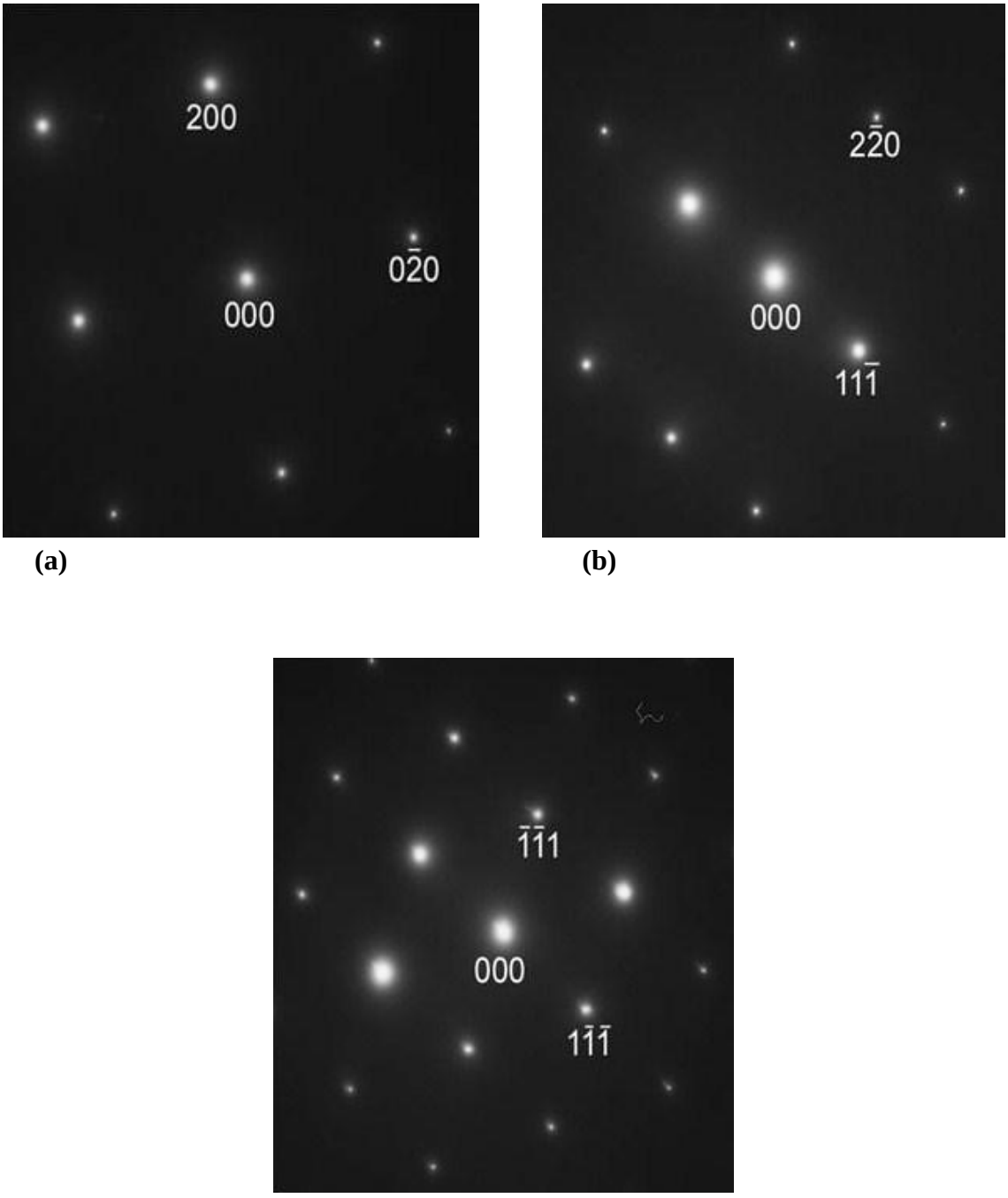

(a) **(b)**

(c)

Figure 4-16: Selected area diffraction patterns from (a) [001], (b) [112] and (c) [101] zone axes of the MC carbide in the weld FZ of Haynes alloy 282.

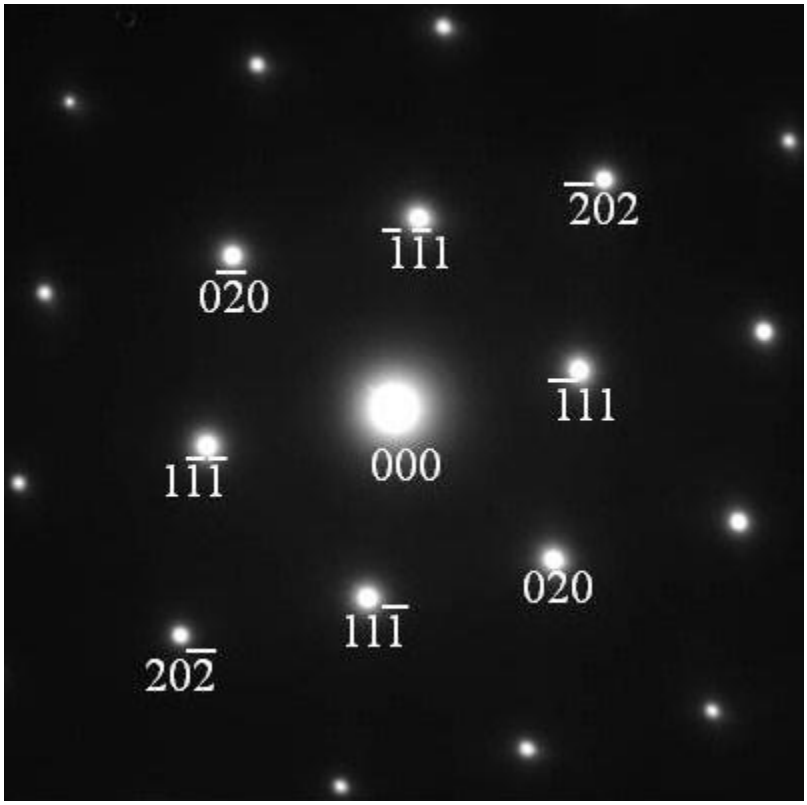

Figure 4-17: Selected area diffraction pattern from [101] zone axis of γ matrix.

diagram adapted by Ojo et al. is re-drawn in Figure 4-18 for the purpose of this discussion and consists of three main phase fields, namely, (i) γ, an FCC solid solution of substitutional alloying elements (ii) MC carbide and (iii) γ′. Point J (Figure 4-18) represents an invariant peritectic point while lines AJ, BJ and CJ represent monovariant lines of two-fold saturation between γ-γ′, γ-MC and γ′-MC. At the initiation of solidification, the first solid to form will be γ dendrites. During their continued formation, the liquid will be enriched in Ti and other carbide forming elements, like Mo, which exhibit partition coefficient k<1, together with C atoms.

Experimental results in the present work confirmed that Ti and Mo segregated into interdendritic regions during solidification in the weld FZ. This enrichment would continue during cooling until the composition of the interdendritic liquid reaches the line that represents equilibrium between γ, MC and liquid. At this stage, the solubility limit of the primary solidification phase γ, would be exceeded such that MC carbide and γ would form and continue to form over a range of temperatures, that is, the following reaction would occur:

$$L \Longleftrightarrow \gamma + MC \quad \text{..... (4.7)}$$

This would explain the formation of MC-type carbides observed in interdendritic regions of the laser weld FZ of Haynes alloy 282. MC carbides are known to form by eutectic-type reactions during solidification of nickel-base superalloys [71,143]. The γ phase that forms with MC carbides during the eutectic transformation could form epitaxially on prior γ matrix, leaving the MC carbides to exist as almost isolated particles, similar to what is observed in the FZ in the present study. This is sometimes referred to as

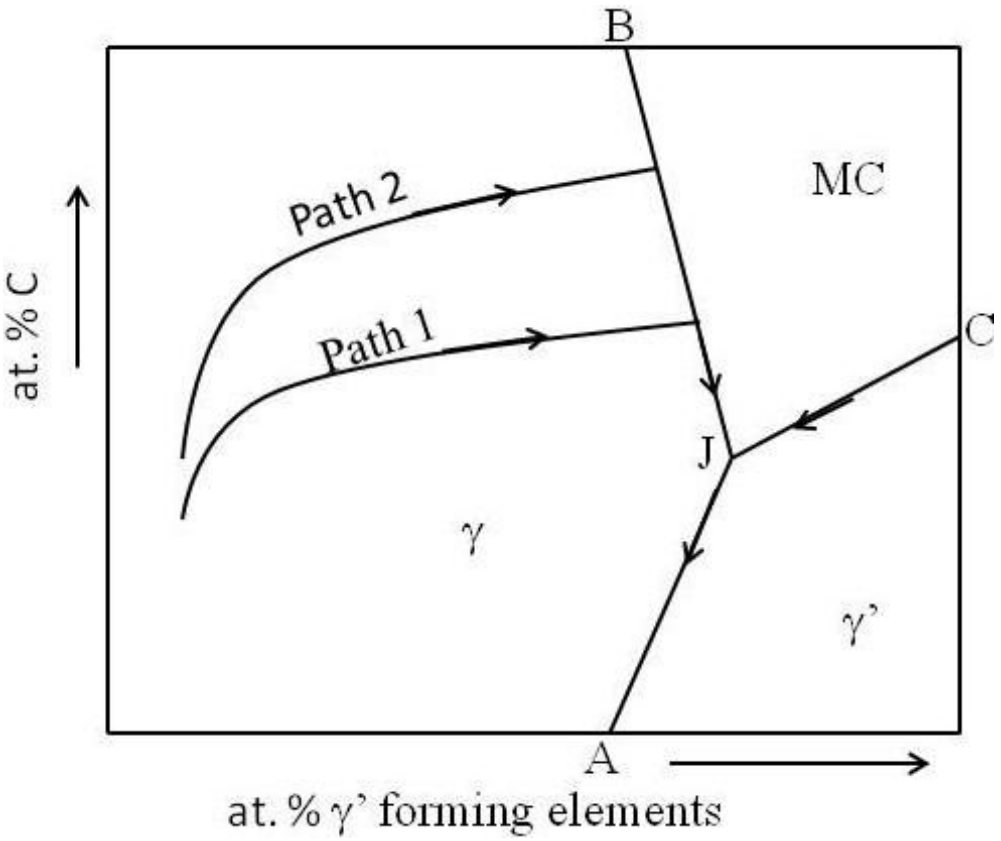

Figure 4-18: Adapted solidification diagram showing influence of carbon (C) content on solidification behavior [71].

Source – Metall. Mater. Trans. A., Reprinted with permission from RightsLink / Springer (23rd July, 2012).

a divorced eutectic morphology. The formation of the MC carbides by an eutectic-type reaction would necessarily occur over a range of temperatures in a multi-components alloy like Haynes alloy 282. Dupont et al [143] have used the liquidus projection surface of the Ni-Nb-C ternary system to show that carbon addition can significantly influence the nature of microconstituents that form during terminal solidification reactions in Nb bearing nickel-based superalloys. Following their illustration, but in this case for γ' precipitation hardened nickel-base superalloys, when the nominal carbon content of an alloy is low, the primary solidification path (path 1 in Figure 4-18) would intersect the γ-MC two-fold saturation line at a point that is close to the peritectic point J. Under this condition, a relatively small amount of liquid is consumed and converted into γ and MC as composition of the liquid only varies to a small extent along the two-fold saturation line before reaching point J, where the composition conditions required for the start of γ-γ′ eutectic are satisfied. The remaining liquid would then form γ-γ' eutectics over a range of temperatures, along the interdendritic region, until solidification is completed.

In contrast, however, when the carbon content is increased, the interdendritic liquid becomes increasingly enriched in carbon and the intersection point occurs at a higher C content (path 2 in Figure 4-18). Consequently, the liquid composition will significantly change along the L $\Leftrightarrow$ γ + MC line of two-fold saturation, forming γ and MC over a range of temperatures before reaching point J, subsequent to which γ-γ′ eutectic transformation starts. In this case (path 2), a larger portion of the liquid is consumed and converted into γ and MC, thus reducing the amount of residual liquid available for γ-γ′ eutectic transformation during the final stages of solidification. In this process, much of the γ′ forming element, Ti, will be consumed by the formation of MC-

type carbides. In alloys with significant amounts of carbon addition, it is possible for almost all, if not all, of the liquid to be consumed by the L $\Leftrightarrow$ γ + MC monovariant reaction such that little or no γ-γ' eutectic forms, as was observed in the present work. As discussed earlier, when the carbon content is low or if the alloy is carbon-free, low enrichment of the interdendritic liquid in C would cause the primary solidification reaction path to shift very close to J (path 1 in Figure 4-18). Under this condition, very little liquid is consumed and converted to γ and MC constituents and there will still be a relatively large amount of liquid available at the peritectic isotherm for γ-γ' eutectic transformation as the solidification progresses. Formation of the γ-γ' eutectic is accompanied by further solute micro-segregation, which enlarges the solidification temperature range, ΔT. The ΔT and the amount and distribution of interdendritic liquid during the last stage of solidification are important factors that affect the susceptibility of nickel-base superalloys to solidification cracking.

Generally, a wider solidification temperature range means a higher propensity to weld cracking. Weld solidification cracking in carbon-free PW1480 single crystal has been related to the formation of γ-γ' eutectic during the last stages of solidification [145]. Also, it has been experimentally observed that the addition of carbon to γ' precipitation strengthened superalloys suppresses the formation of γ-γ' eutectic [146-148]. Therefore, carbon additions in the Haynes alloy 282, which conceivably aided the preclusion of the deleterious γ-γ' eutectic formation and its associated enlarged ΔT, appear to have contributed to the resistance of this newly developed superalloy to solidification cracking in the weld fusion zone.

4.5 Microstructure of Heat Affected Zone (HAZ)

The HAZ around laser beam welds made after pre-weld heat treatment suffers from varying degrees of intergranular cracking (Figures 4-19a and b). Most of the cracks are concentrated in the neck region of the keyhole shaped weld, in HAZs that are slightly away from the FZ. Some of the main features of the cracks include an irregular zigzag morphology of the fracture path and close association with widened grain boundaries, which are typical features that depict intergranular liquation cracking [67-68].

The HAZ of a weldment is made up of the partially melted zone located adjacent to the weld fusion line wherein the extent of melting that occurs ranges from 0 to 100%. Previous investigations of the weld HAZ in fully austenitic Fe and nickel-base superalloys have shown that HAZ that experience peak temperature below the solidus temperature are highly susceptible to liquation cracking [149]. HAZ cracks are known to occur by the formation and persistence of liquid films at the HAZ grain boundaries and the inability of the grain boundary liquid film to sustain thermal stresses and strains caused by the welding cycles.

4.5.1 The Cause of Intergranular HAZ Liquation Cracking in Haynes Alloy 282

HAZ grain boundary liquation is widely believed to occur either by non-equilibrium subsolidus melting or equilibrium super-solidus melting [63-64]. Although supersolidus melting is expected to occur in all weldments due to heating above the equilibrium solidus temperature in certain regions, subsolidus grain boundary melting is, however, more insidious and detrimental, as it extends both the effective melting

(a)

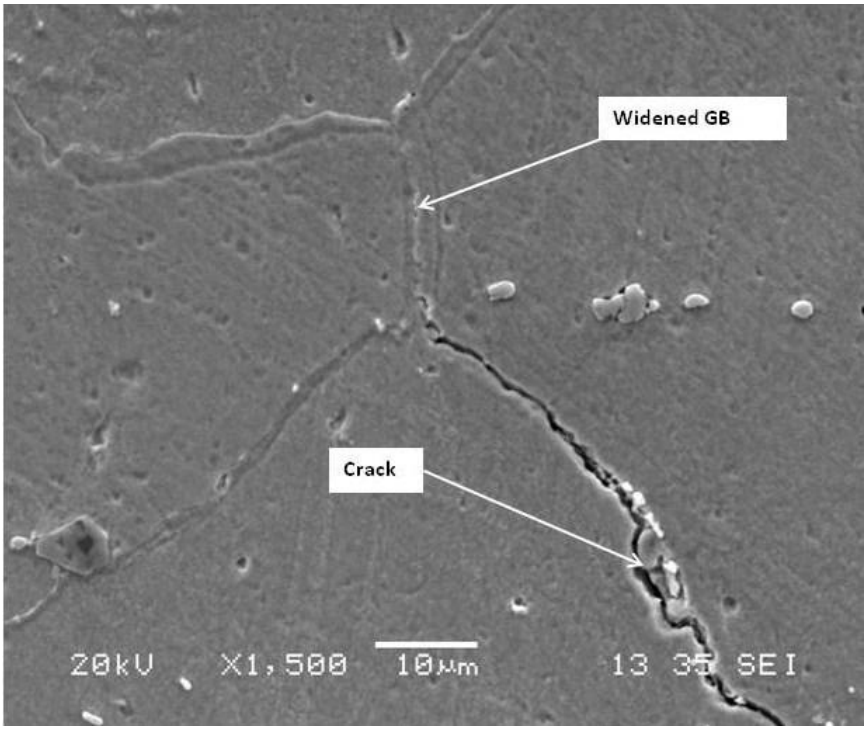

(b)

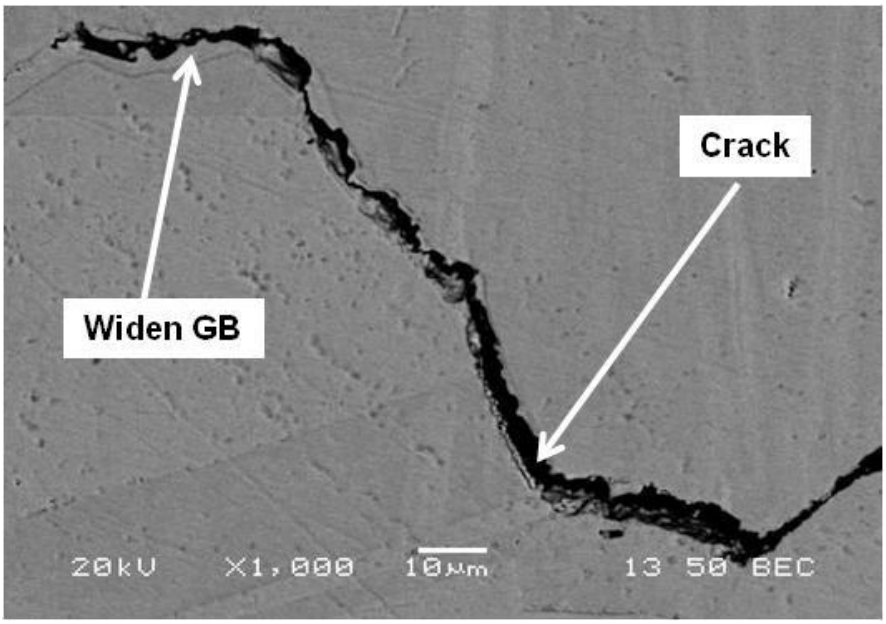

Figure 4-19: SEM micrograph of HAZ showing cracks and associated features.

temperature range and the size of the crack susceptible region in the HAZ [65-66]. Besides that, subsolidus melting is also known to influence the nature of melting at supersolidus temperatures by pre-establishing local heterogeneities that are capable of altering the kinetics of reaction during subsequent heating [65]. One of the mechanisms used to explain the subsolidus formation of liquid film along grain boundaries is the constitutional liquation of second phase particles present in pre-weld material due to non-equilibrium reactions between the particles and the surrounding matrix [67, 150-152].

The short integrated time and steep temperature gradient during welding thermal cycle induces microstructural variation over a relatively short distance in HAZ of weldments. This makes detailed microstructural analysis and relations between phase transition and peak temperature difficult to ascertain. The grain boundary liquation features observed in the present work suggest that the HAZ liquation involves significant subsolidus liquation. To enable a reliable verification of subsolidus liquation occurrence in the Haynes alloy 282 during welding, Gleeble thermo-mechanical simulation system was used to physically simulate its HAZ microstructure. Meanwhile, the main equilibrium phase transformation temperatures in this new alloy, as determined by a differential scanning calorimetry (DSC) study, have indicated that the solidus is ~1244^{o}C (Table 4-3). Haynes alloy 282 specimens were rapidly heated by the Gleeble system to peak temperatures below the equilibrium solidus temperature of the alloy, from 1050^{o}C to 1200^{o}C, to evaluate the response of the alloy to rapid welding thermal cycles.

Microstructural examination of the Gleeble specimens simulated at peak temperatures up to 1120^{o}C showed that the second phase precipitates along the grain boundaries in the alloy remained largely unaffected by the Gleeble simulation thermal

cycle (Figure 4-20a and b). However, in specimens rapidly heated to 1150^{o}C and 1170^{o}C and held for 1 second, complete dissolution of the intergranular particles occurred and the widening of grain boundary regions was observed (Figure 4-21a). An increase of the holding time at the peak temperatures to 3 seconds resulted in reduction in the occurrence of widened grain boundaries (Figure 21b). This behavior is consistent with grain boundary liquation caused by constitutional liquation of second phase particles [67].

A major consequence of intergranular liquation in nickel-base superalloys is poor hot ductility under tensile loading. In order to further confirm the occurrence of liquation on widened grain boundaries observed at 1150^{o}C and 1170^{o}C, the hot ductility of the alloy was evaluated by subjecting Gleeble specimens to tensile loading, first, after holding for 0.1 seconds at various peak temperatures and the results are presented in Figure 4-22. The alloy initially exhibited high hot ductility, but the ductility dropped to a significantly low level at 1150^{o}C and approached zero at around 1170^{o}C. As stated earlier, widened grain boundaries were observed at peak temperatures of 1150^{o}C and 1170^{o}C, at which the alloy exhibits considerably poor ductility. On increasing the holding time from 0.1 seconds to 3 seconds during the hot ductility test at 1170^{o}C, an improvement in ductility from 3% to 26% was notably observed. The increase in ductility with holding time correlates with the observed reduction in thickness of widened grain boundaries with increase in holding time, which can be attributed to the re-solidification of intergranular metastable liquid, since the liquid phase reduces hot ductility [67].

Previous studies have shown that another verifiable way of confirming grain boundary liquation is by fractography study of crack surfaces [69, 121-122]. SEM study of fractured surface of Gleeble hot ductility specimens confirmed brittle intergranular

(a)

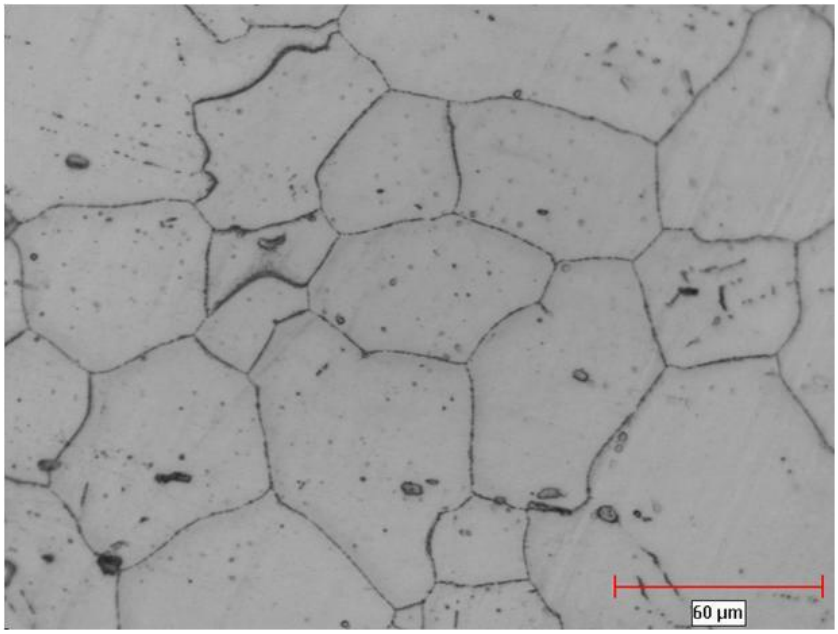

(b)

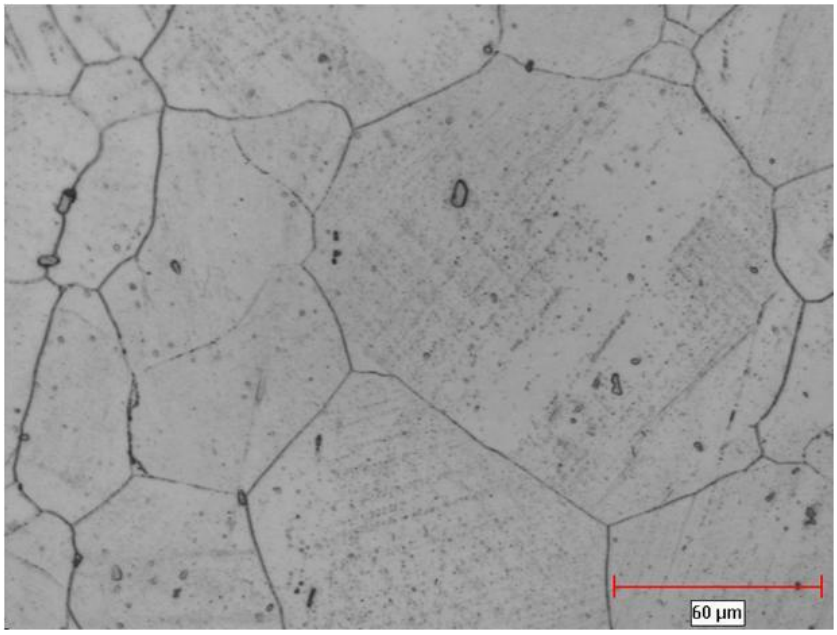

Figure 4-20: Optical micrograph of (a) solution heat treated Haynes alloy 282 and (b) Gleeble simulation specimen that was rapidly heated to 1120^{o}C and held for 1 second.

(a)

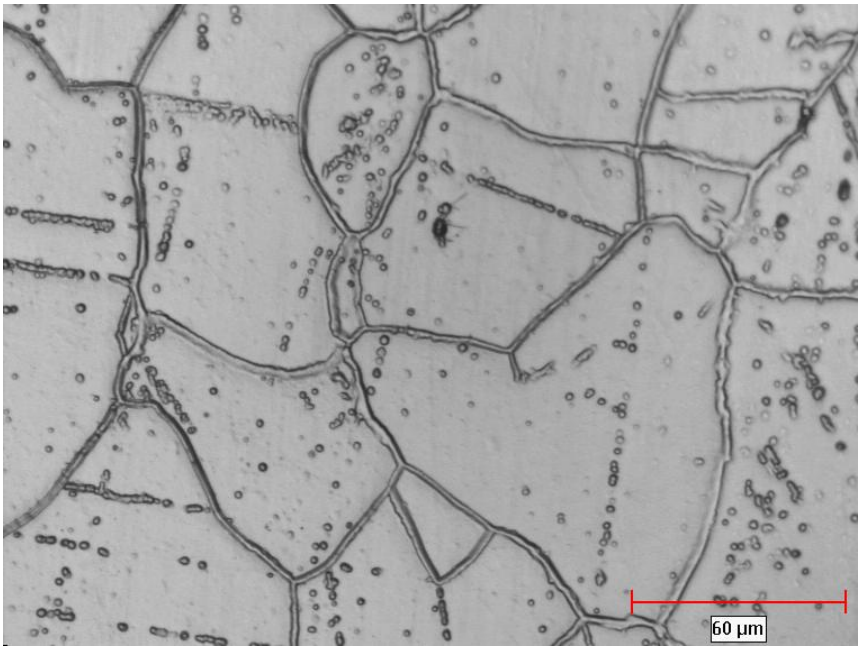

(b)

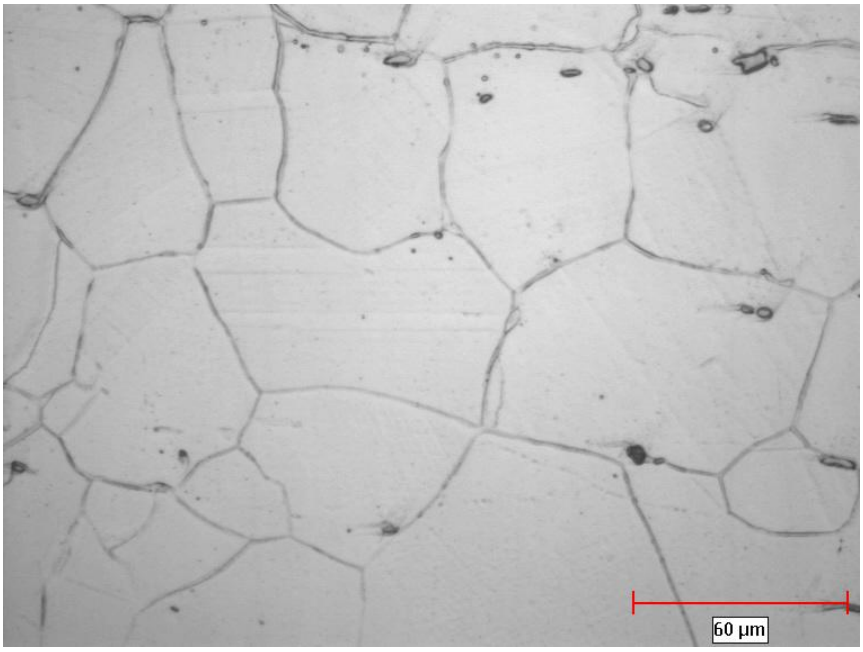

Figure 4-21: Optical micrographs of Gleeble simulation specimen (a) at 1170^{o}C held for 1 second showing widened grain boundaries and (b) 1170^{o}C held for 3 seconds showing reduction in the occurrence of widened liquated grain boundaries.

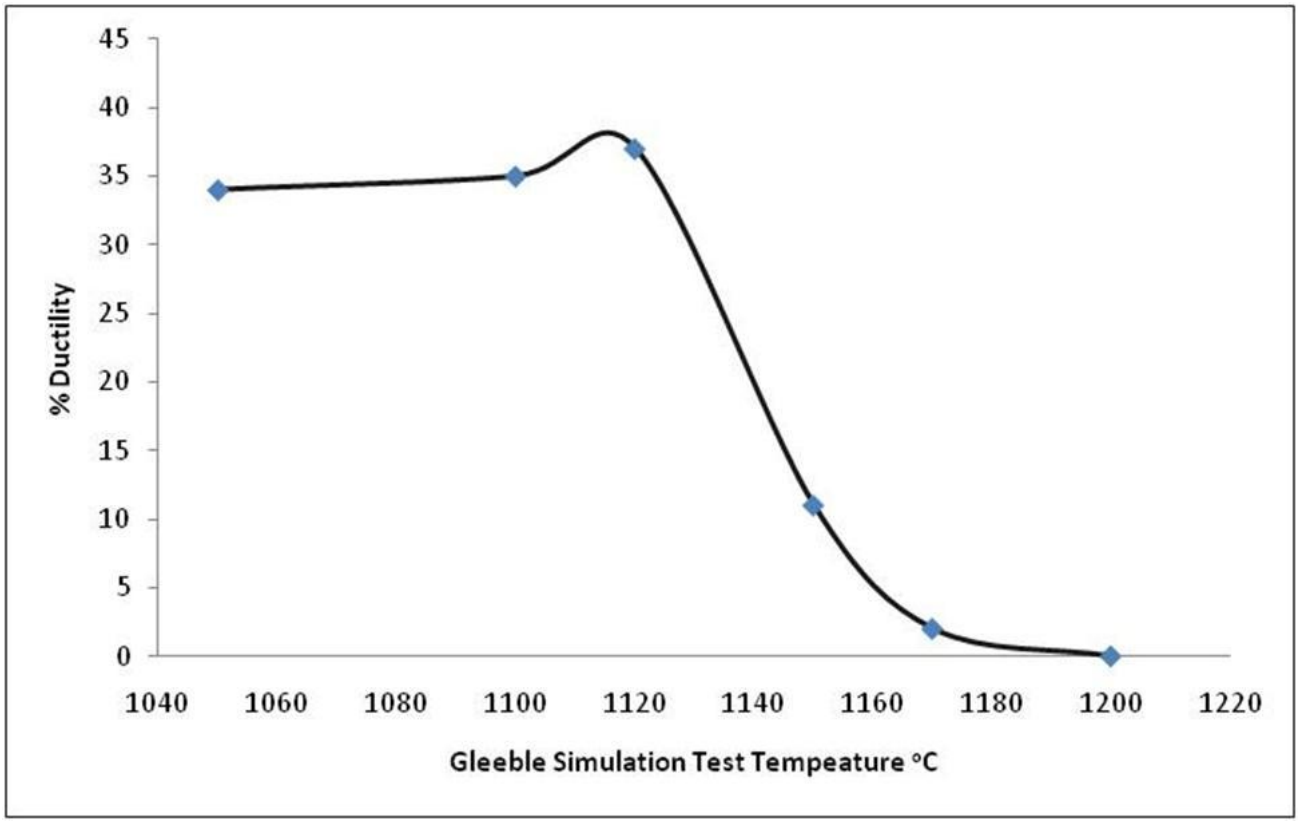

Figure 4-22: Variation in hot ductility of Haynes alloy 282 with peak temperature after holding for 0.1 seconds.

failure in specimens tested at 1150^{o}C and 1170^{o}C with 0.1 second of holding time, which correlates with the loss of ductility observed at these temperatures (Figure 4-23a). A higher magnification examination of the grain surfaces revealed regular roundish surface features all over the grain facets (insert in Figure 4-23a), which have been reported to be an indication of re-solidified intergranular liquid phase [69]. For the sake of clarity and comparison, Figure 23b shows the fractured surface of a hot ductility test specimen tested at 1120^{o}C, where the alloy exhibits high ductility. The specimen exhibits a ductile transgranular failure mode in contrast to the brittle intergranular fracture observed in the specimens tested at 1150^{o}C and 1170^{o}C.

Therefore, degradation of the capability of Haynes alloy 282 to accommodate welding stresses, due to the embrittling effect of intergranular liquation caused by liquation of second phase precipitates, is an important factor that contributes to the susceptibility of the material to HAZ cracking during laser welding. A careful analysis of the Gleeble simulated specimens did not show any evidence of constitutional liquation of MC carbides at the peak temperatures of 1150^{o}C and 1170^{o}C, which is consistent with the reported liquation behavior of the carbides in nickel-base superalloys [152]. Also, Owczarski et al. [153] in their study of the weldability of nickel base superalloys indicated that $M_{23}C_6$ particles would undergo a solid-state reaction well below the solidus temperature and would not constitutionally liquate during welding.

It is, thus, possible that the subsolidus intergranular liquation observed at 1150^{o}C and 1170^{o}C is mainly caused by the constitutional liquation reaction of the M_5B_3 borides as identified for the first time during the course of this research. In order to verify this

(a)

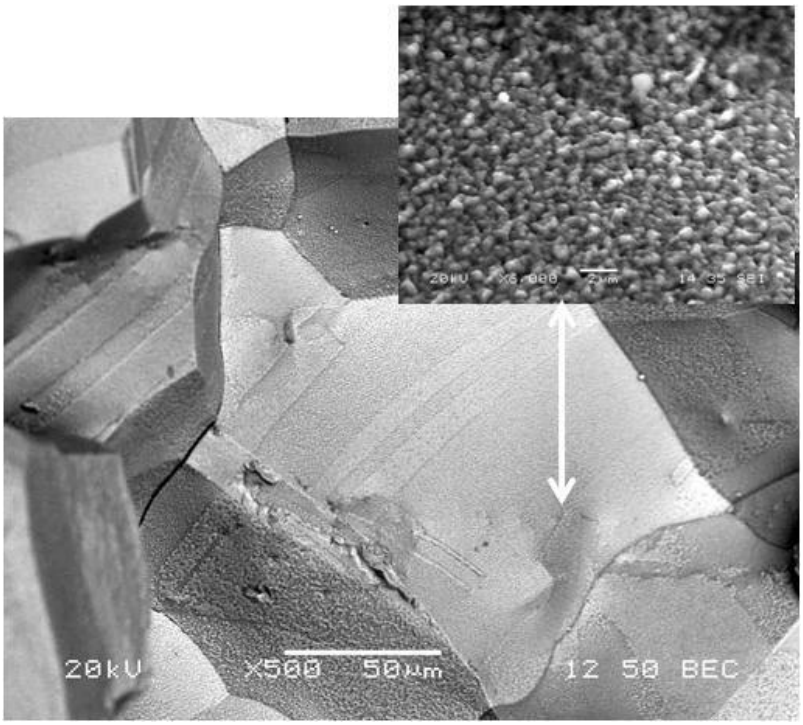

(b)

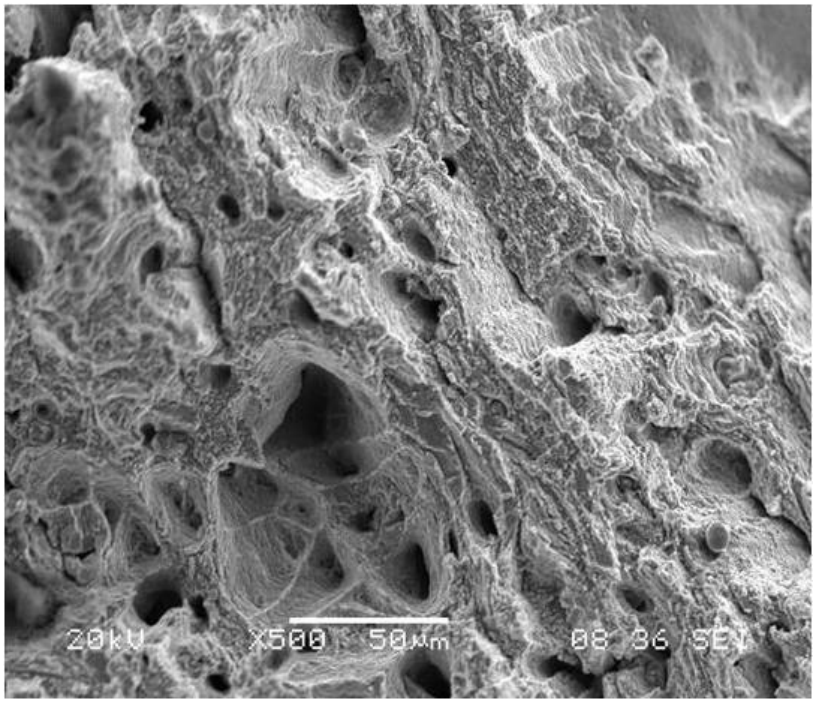

Figure 4-23: SEM fractograph of Gleeble specimen tested (a) at 1170^{o}C held for 0.1seconds (insert shows re-solidified liquid phase), and (b) 1120^{o}C held for 0.1seconds.

possibility, Haynes alloy 282 specimens subjected to heat treatment at 1100^{o}C, which dissolves the $M_{23}C_6$ carbides and leaves the M_5B_3 borides as the main intergranular precipitates (Figure 4-24a), were rapidly heated by the Gleeble system to various peak temperatures.

The Gleeble simulation results showed that grain boundary liquation still occurs at 1150^{o}C and 1170^{o}C, despite the exclusion of the $M_{23}C_6$ carbides, which indicates that the subsolidus non-equilibrium liquation reaction is attributable to constitutional liquation of the M_5B_3 borides (Figure 4-24b). Figure 4-24c shows the results of an SEM-EDS line scan across a M_5B_3 particle along a liquated grain boundary region in a Gleeble simulated specimen that was heat treated at 1100^{o}C. The enrichment of the boride with Mo and the depletion of Cr in the boride, shown by the line scan results, are consistent with the results of the TEM-EDS analysis of the boride phase (Figure 4-3b)

4.5.2 Factors Aiding HAZ Liquation Cracking in the Haynes Alloy 282

In many of the available studies on intergranular liquation cracking, it is reported that the mere occurrence of liquation is adjudged to be inadequate to induce a microstructure susceptible to cracking. The liquid phase must of necessity wet, infiltrate and spread along grain boundary region in a continuous or semi-continuous fashion, replacing the solid-solid interfacial energy along the grain boundary with a weaker solid-liquid interfacial energy [49]. Ineffective wetting of grain boundary regions by the liquid film will results in the liquid existing in isolated pocket that allows for substantial solid-solid intergranular contact. To a first approximation, the distribution of intergranular liquid can be treated in accordance with the relationship proposed by Smith [154]:

(a)

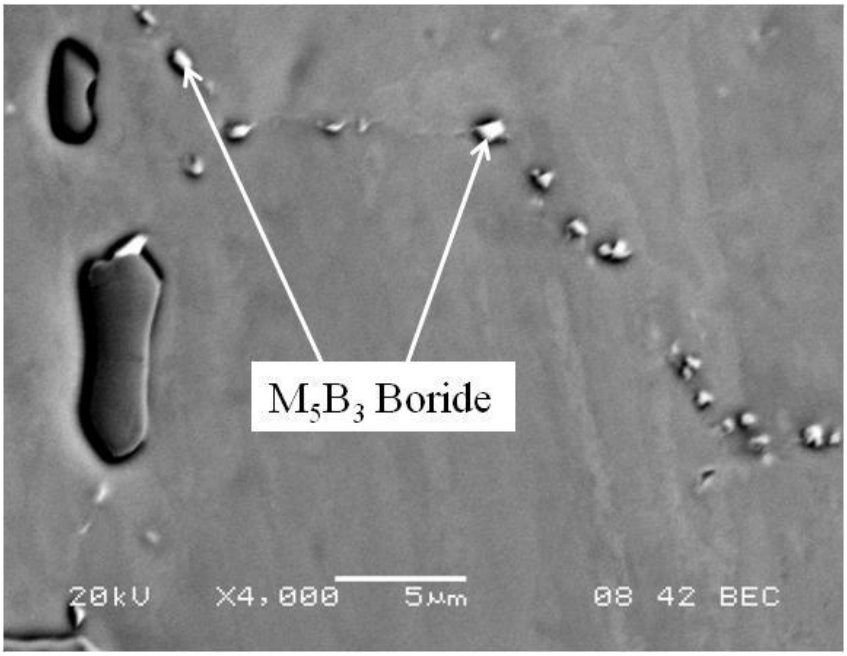

(b)

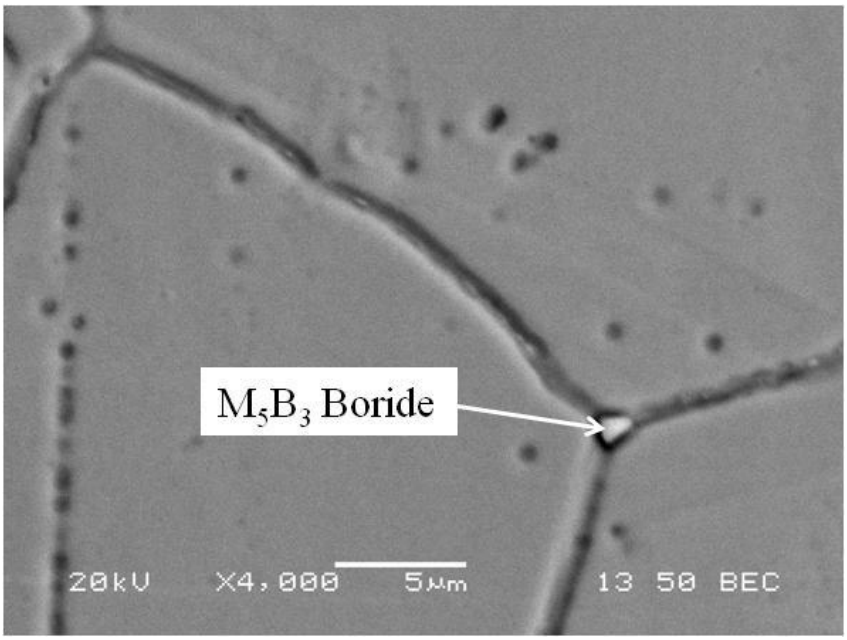

Figure 4-24: SEM micrographs of (a) solution heat treated specimen at 1100^{o}C before Gleeble simulation, and (b) Gleeble simulation specimen rapidly heated to 1170^{o}C and held for 1 second, which shows intergranular M_5B_3 particle associated with liquated and widened grain boundaries.

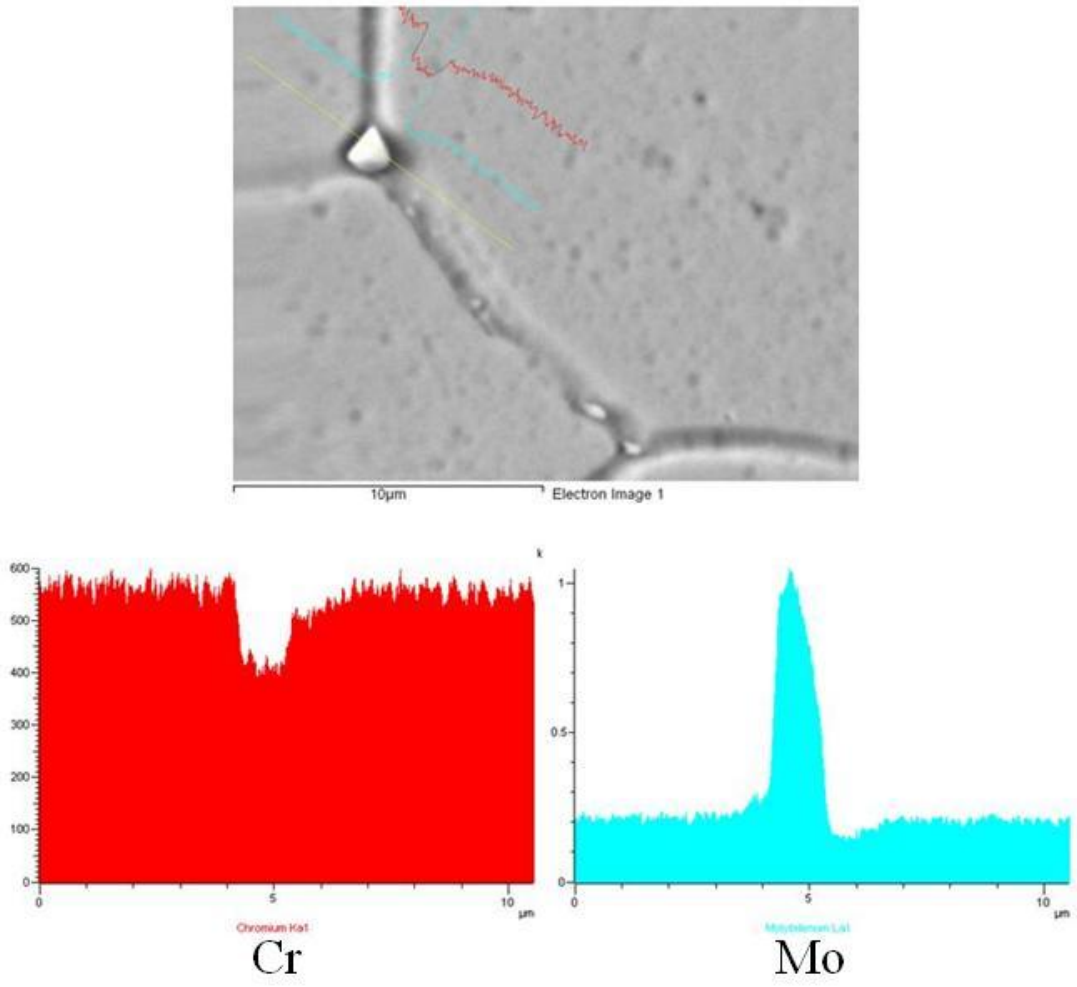

Figure 4-24c: Results of SEM-EDS line-scans across a M_5B_3 particle along liquated grain boundary region.

$$\gamma_{gb} = 2\,\gamma_{SL}\,\mathrm{Cos}\,\theta \quad \ldots\ldots\ldots\ldots\ldots\ldots\ldots\ldots\ldots\ldots\ldots\ldots\ldots\ldots\ldots\ldots\ldots \quad (4.8)$$

where θ is the wetting angle, γ_{gb} is the grain boundary energy and γ_{SL} is the solid-liquid interface energy. From Equation 4.8, it can be seen that for a given grain boundary energy, the lower the solid-liquid interface energy, the lower will be the wetting angle and the easier it will be for such a liquid to wet and spread along the grain boundary. The presence of boron atoms in the intergranular liquid produced by liquation of the M_5B_3 borides could substantially aid the wetting behavior of the liquid through the influence of the surface active boron atoms in lowering the solid-liquid interface energy along the grain boundary. In an alternate and/or complementary case, as apparent from Equation 4.8, for a given solid-liquid interfacial energy, the higher the grain boundary energy, the higher is the tendency for it to be wetted and penetrated by liquid phase.

In the present study, EBSD analyses of grain boundary character showed that most of the grain boundaries in the as-received and heat treated Haynes alloy 282 are more of a ‘random’ nature with a higher order of “Σ” values (Figure 4-25). Random high angle grain boundaries are inherently of higher energy than special boundaries. The fact that most of the grain boundaries in the Haynes alloy 282 are of the high energy type could be another factor that enables intergranular wetting and penetration by liquid film in the alloy. Guo et al. [96] and Kokawa et al. [155] confirmed that liquid penetration at grain boundary was greatest at high angle boundaries and relatively insignificant at low angle boundaries.

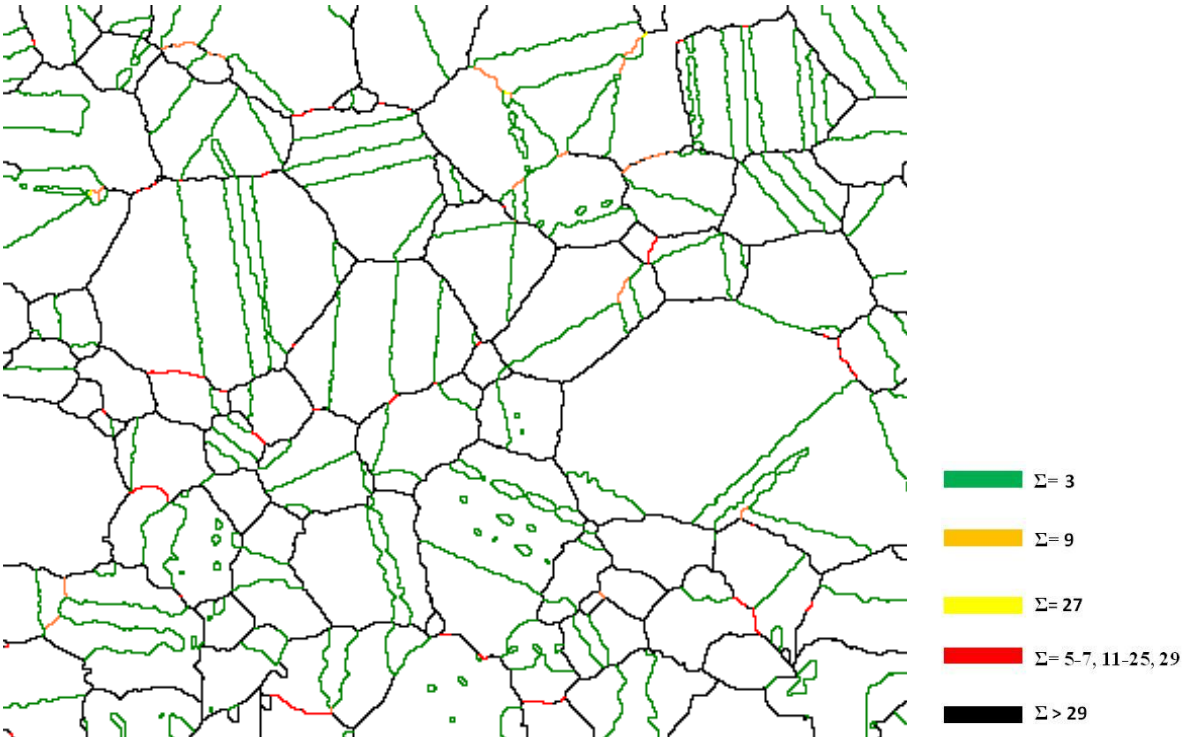

Figure 4-25: EBSD analysis of grain boundary character distribution in the Haynes alloy 282. High angle grain boundaries Σ > 29 in black color.

Furthermore, the metastable liquid produced by the constitutional liquation of intergranular second phase particles always reacts with the adjacent solid grains through back diffusion of solute atoms across the solid-liquid interface. In these situations, the non-equilibrium solid-liquid interfacial energy is extremely low [156], which would make the liquid to effectively wet the grain boundary and exhibit extensive penetration. A theoretical model developed for describing the penetration of the liquid phase along a grain boundary has also shown that grain boundary penetration requires an under-saturated solid [157]. This is essentially the situation prevalent in the subsolidus HAZs during non-equilibrium rapid heating and cooling of welding operation. During the rapid heating cycle, decomposition of intergranular M_5B_3 borides can result in the release of boron atoms along grain boundary regions.

Aside from aiding grain boundary wetting, the boron released from M_5B_3 borides is a potent melting point depressing element in nickel alloys. The enrichment of intergranular regions with boron atoms can reduce the starting temperature for grain boundary liquation during heating and also reduce the terminal solidification temperature during cooling. Previous studies [66,158] have shown that on-cooling hot ductility behaviour is dependent on the hot ductility behaviour during heating. On-heating ductility behaviour can thus provide an indication of expected ductility behaviour during cooling. Any factor that reduces the on-heating ductility will reduce the ductility during cooling. As an example, any factor that decreases the on-heating zero ductility temperature will reduce the ductility recovery temperature (DRT) during cooling. DRT during cooling is generally lower than the zero ductility temperature during heating [66, 158].

Therefore, in the present work, the grain boundary liquation which reduced the on-heating zero ductility temperature would in effect enlarge the brittle temperature range and delay the ductility recovery of the HAZ during cooling, both of which would promote susceptibility to liquation cracking. Therefore, the subsolidus liquation reaction of the intergranular M_5B_3 borides constitutes a major factor that reduces the resistance of the newly developed Haynes alloy 282 to weld HAZ cracking.

4.5.3 Effect of Heat Input on HAZ Cracking of Haynes Alloy 282

The susceptibility of precipitation strengthened superalloys to weld HAZ liquation cracking has generally been attributed to both mechanical and metallurgical factors. The metallurgical factors include, pre-weld heat treatment schedules, processing conditions (wrought, forged or cast) and grain size, among others. The mechanical factors are principally influenced by the magnitude of heat input, i.e. welding parameters, which inadvertently controls the states of stresses in the weldment. The understanding of how susceptibility to weld HAZ cracking is influenced by laser heat input is crucial to developing an optimum welding procedure for preventing or minimizing the cracking problem and facilitates the application of laser beam for joining the newly developed nickel-base Haynes alloy 282. Therefore, an investigation was carried out to determine the fundamental dependence of weld HAZ cracking on laser heat input as controlled by welding parameters.

The effect of laser beam welding heat input on the magnitude of HAZ cracking and weld size is presented in Figure 4-26 and Table 4-4 respectively. The total crack length (TCL), depth of penetration, FZ and HAZ area were observed to vary with heat

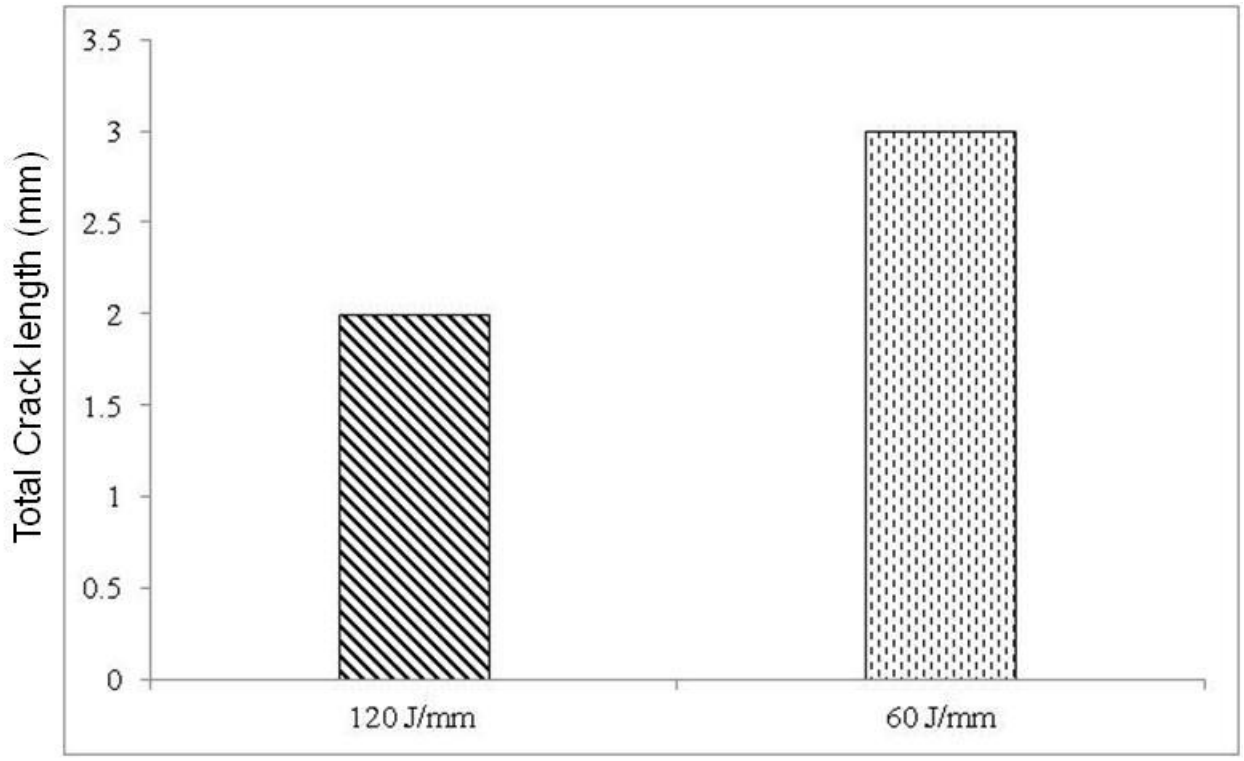

Figure 4 - 26: Effect of Heat Input on variation in Total Crack Length (TCL).

Table 4 - 4: Dimensions of high and low heat input laser welds

Speed mm/min	Power kW	Heat Input J/mm	Depth of Penetration (mm)	Top Width/Depth Ratio	Area FZ mm^2	Area HAZ mm^2
1000	2.0	120	4.6	0.7	5.9	8.6
2000	2.0	60	3.9	0.5	3.2	4.2

input, which is a function of laser power and welding speed. Since the size of the weld changes with heat input, in order to enable a more realistic comparison analysis of the cracking behavior, quantitative index of cracking CI was calculated by normalizing the TCL with respect to the HAZ area, by using a method reported by Richards et al [54]. The CI, as a quantitative indicator of the length of crack per unit area, provides a meaningful comparison of the susceptibility of the alloy to HAZ cracking. The low heat input laser weld experienced a larger extent of cracking compared to the high heat input laser weld. The CI of low heat input weld (60 J/mm) is appreciably larger than the CI of a higher heat input weld (120 J/mm) (Figure 4-27). Miller and Chadwick [159] related the tensile stress σ required to cause cracking by overcoming the surface tension γsl at the solid/liquid interface on liquated boundaries to the liquid film thickness h by the equation:

$$\sigma = 2\gamma_{sl} / h \quad \text{..... (4.9)}$$

The implication of this relationship is that any factor that reduces the thickness of the intergranular liquid could in effect improve the resistance to cracking by increasing the magnitude of stress required to cause intergranular microfissuring. Grain boundary liquid film migration (LFM) is another fundamental mechanism by which the thickness of metastable intergranular films can significantly decrease through rapid solidification, thereby aiding resistance to liquation cracking [133,159]. This solidification mode, which is controlled by a high diffusion rate in the liquid, is an alternative to lattice diffusion controlled and the normal dendritic solidification types. Reversed grain boundary curvature, which is a vital microstructural feature of the LFM process, was observed in the HAZ in the present work (Figure 4-28).

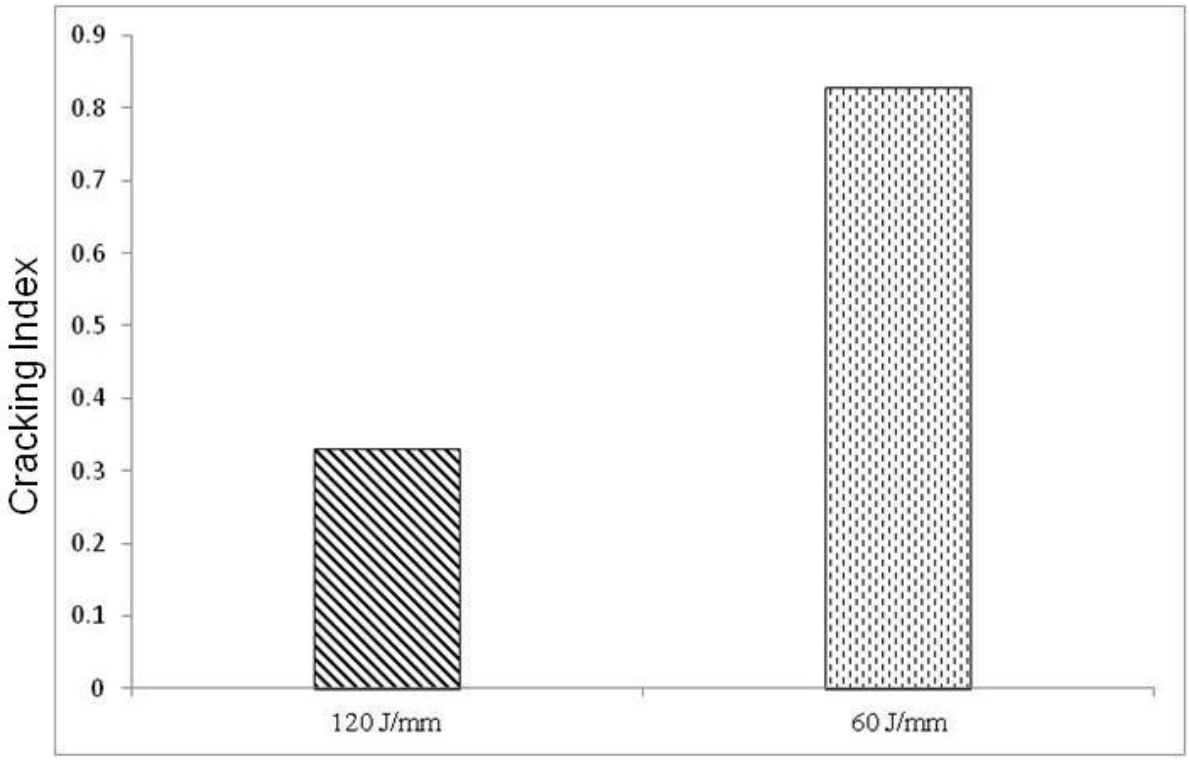

Figure 4-27: Effect of Heat Input on variation in cracking index (CI).

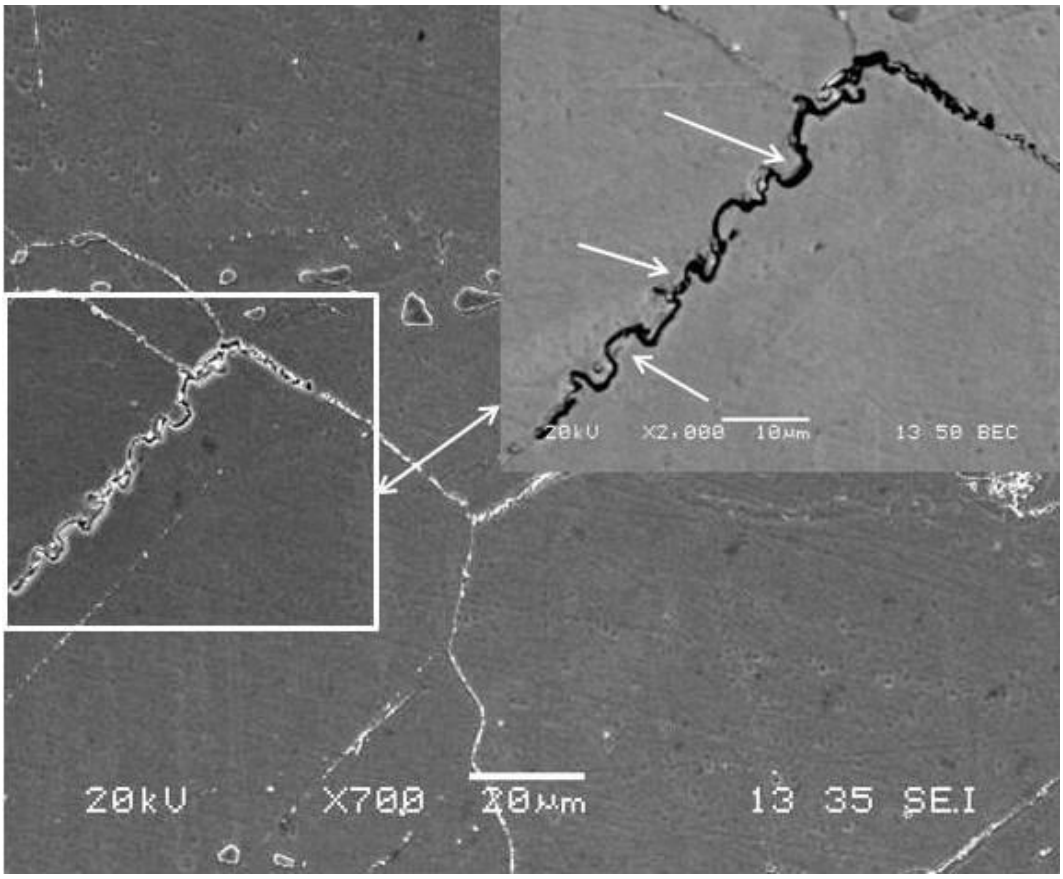

Figure 4-28: Image (SEM) showing grain boundary with typical intergranular liquid film migration feature.

Weld HAZ is generally known to spend a longer time at peak temperatures during high heat input welding compared to in low heat input weld. The longer amount of time that the HAZ spends at peak temperatures during high heat input welding could favor extensive re-solidification via LFM and/or solute back-diffusion process and thus, eliminate or significantly reduce intergranular liquid film thickness compared to low heat input welding. According to Equation (4.9), such reduction in the thickness of the grain boundary liquid film thickness, which would increase the magnitude of tensile stress required for cracking, could be a contributing factor to the lesser extent of HAZ cracking observed in high heat input welds.

Aside from the possible influence of heat input on the size of intergranular liquid film thickness, the magnitude of the driving force for cracking, welding stress, can also be influenced by the level of heat input involved during welding. During welding, the generation of thermally induced stress and associated strain is unavoidable. This is fundamentally due to differences in the rates of expansion and contraction of the HAZ owing to variation in the temperature experienced by these regions. The magnitude of such thermally generated welding stress is directly proportional to HAZ temperature gradient. High heat input welds are known to exhibit shallow temperature gradient in the HAZ during welding compared to the steep HAZ thermal gradient that characterizes low heat input welds. Therefore, the larger extent of cracking observed in low heat input laser welds, in the present work, may be related to a greater level of thermally induced stress generated during welding compared to the higher heat input weld.

Tungsten inert gas (TIG) arc welding is known to be an inherent high heat input welding process [34]. In the present study, some of the solution treated Haynes alloy 282

specimens were welded by the TIG process with a high heat input of 490 J/mm. Microstructural examination showed that both FZ and HAZ in the TIG welded materials were free of cracks which corroborate the result obtained in the laser welds in that an increase in heat input reduces HAZ cracking. However, the TIG weld is shallow (~ 1.1 mm in depth) with a large surface width (~ 5.2 mm) and contains a wide HAZ (Figure 4-29).

Although it was observed in the present work that reduction in heat input increases TCL and cracking susceptibility, generally, the low heat input welding process such as laser welding, is still preferred due to better weld shape and size in terms of penetration and width, and reduced material distortions that are associated with low heat input welds. Therefore, the focus in this research was subsequently directed towards improving the resistance of Haynes alloy 282 to HAZ cracking during laser beam welding, through pre-weld microstructural modifications and this will be presented and discussed next.

4.5.4 Effect of Pre-weld Heat Treatments on HAZ Cracking of Haynes Alloy 282

Previous studies on the weldability of precipitation strengthened Ni-based superalloys have shown that carefully designed pre-weld microstructural modification through thermal treatments can be beneficial in reducing the problem of susceptibility to HAZ hot cracking [107,161-162]. For example, Thompson et.al. [162] reported that weldability is positively affected by solution annealing and adversely by aging in the IN 718 alloy. It has also been reported that IN 718 and IN 718Plus specimens that were

(a)

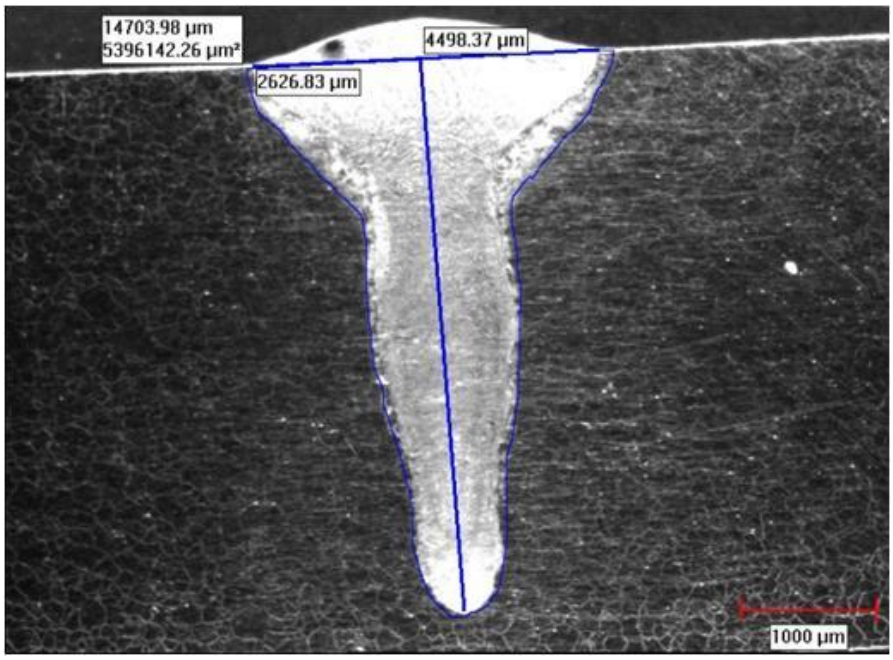

(b)

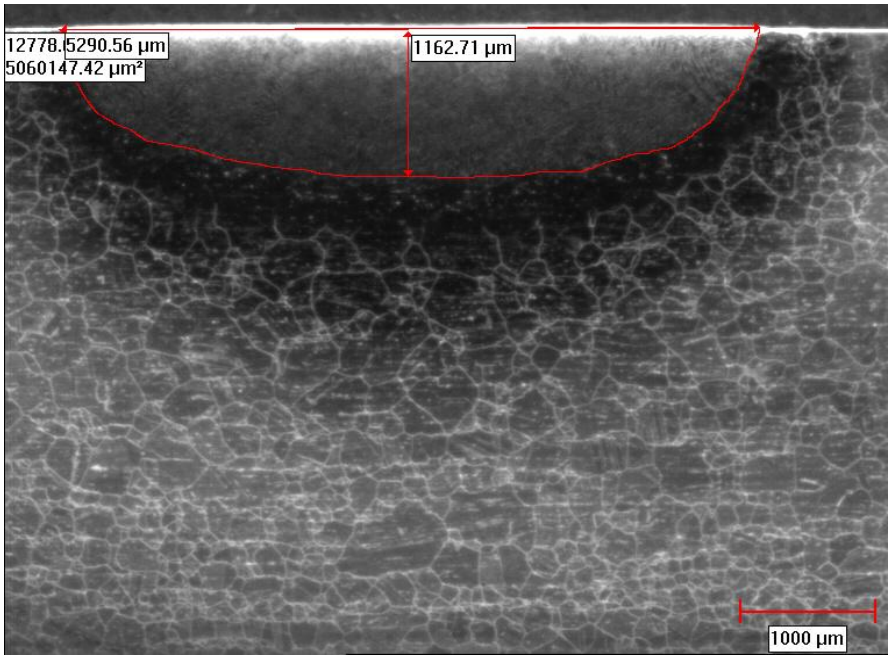

Figure 4-29: Low magnification optical micrographs showing general weld profile of Haynes alloy 282 made with (a) low heat input laser beam and (b) high heat input TIG weld.

subjected to high temperature solution heat treatment (1050–1150^{o}C) are more susceptible to HAZ hot cracking [98-99]. In Udimet 700 [65] and IN 738 alloy [163], significant improvement in resistance to weld cracking was achieved by an overaging treatment as compared to welding in standard solution heat treatment condition. The improvement in the resistance to weld cracking by the overaging treatment was attributed to the minimized effect of stresses and strains that accompany rapid γ' precipitation. Overaging by coarsening of the γ' phase prior to welding reduces alloy hardness, which consequently enhances its capability to relax part of the welding stresses and strains generated on cooling. Overaging treatment of Haynes alloy 282 specimens before welding, however, resulted in more and extensive HAZ liquation cracking.

As discussed earlier in this thesis, liquation of the M_5B_3 borides is found to be the major factor that causes HAZ cracking in the Haynes alloy 282. Therefore, heat treatments of the alloy at 1050^{o}C – 1150^{o}C for 2 hours were carried out to study the effect of the dissolution behavior of the boride particles. The results showed that no major dissolution of the boride particles occurs at 1050^{o}C, but an increase in heat treatment temperature to 1080^{o}C - 1100^{o}C (Figure 4-24a) results in significant dissolution of the particles, such that very few discrete particles remain after heat treatment at these temperatures. A further increase in temperature to 1120^{o}C and above resulted in the complete dissolution of the boride particles (Figures 4-30a and b). Specimens subjected to heat treatment at 1050^{o}C – 1150^{o}C and air-cooled were laser welded to examine the effect of the boride dissolution on susceptibility to HAZ cracking. Three different welding test coupons were used for each pre-weld heat treatment condition. Ten weld cross-sections were prepared from each test coupon for the crack measurement. The

(a)

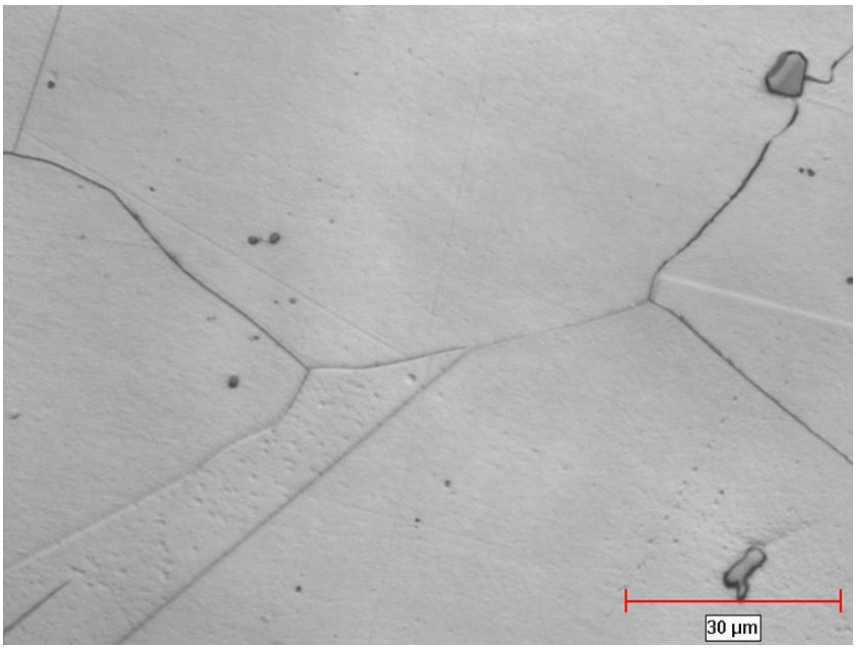

(b)

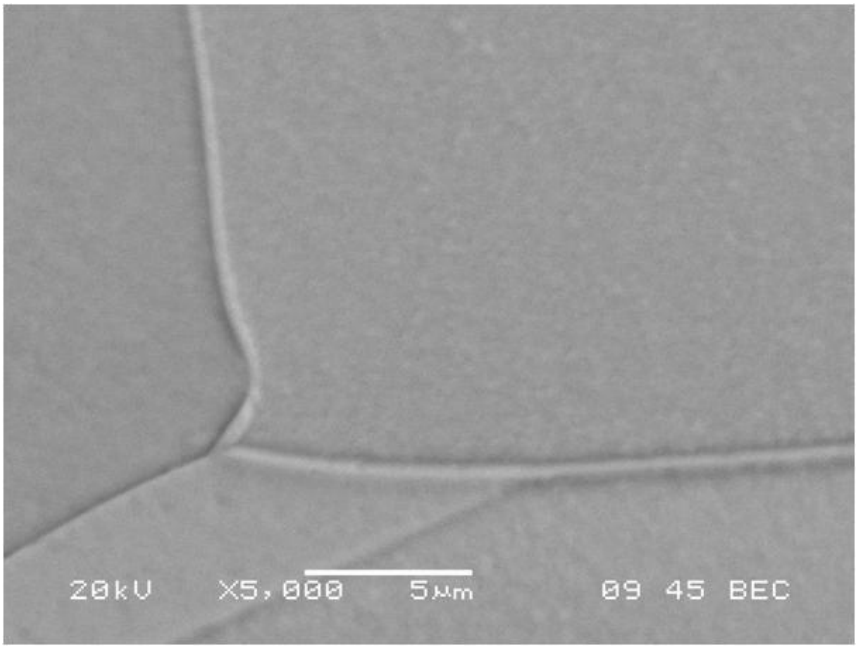

Figure 4-30: (a) Optical and (b) SEM micrographs of specimen solution heat treated at 1150^{o}C showing the grain boundaries free of M_5B_3 boride particles.

average values of the TCL in the ten weld cross-sections from the three different welded test coupons for each of the pre-weld heat treatment conditions are presented in Figure 4-31.

As shown by the results, the presence of the boride particles in the specimen that had been heat treated at 1050^{o}C resulted in an appreciable cracking of the HAZ. Reduction in the volume fraction of the borides by heat treatment at 1080^{o}C - 1100^{o}C significantly reduced the level of cracking. Interestingly, however, complete dissolution of the boride particles by a pre-weld heat treatment at 1120^{o}C and above exacerbates, rather than, reduces the cracking. The reason why complete dissolution of the borides, which are known to aid susceptibility to cracking, by constitutionally liquating during welding, caused increase rather than decrease in cracking was investigated.

At 1120^{o}C and above, which are temperatures above the solvus temperature of the boride phase, all the boron atoms initially tied down in the boride particles were released into the surrounding austenitic, γ, matrix phase. As previously mentioned in section 4.2, the size misfit of boron atoms for both the substitutional and interstitial sites in austenitic lattice makes it energetically favorable for boron atoms to segregate to loosely packed regions, like grain boundaries. When alloys are quenched from high temperature, the equilibrium vacancy concentration falls and vacancies migrate to interfaces such as grain boundaries where they can be readily annihilated. Solute atoms in a crystal, especially surface-active elements like boron, have an associated strain energy that can be relieved by pairing with vacancy to form vacancy-solute complex. Vacancy flow, with an associated solute flux, to annihilation sites like grain boundaries can thus occur during cooling from high temperature, which is a phenomenon generally referred to as non-

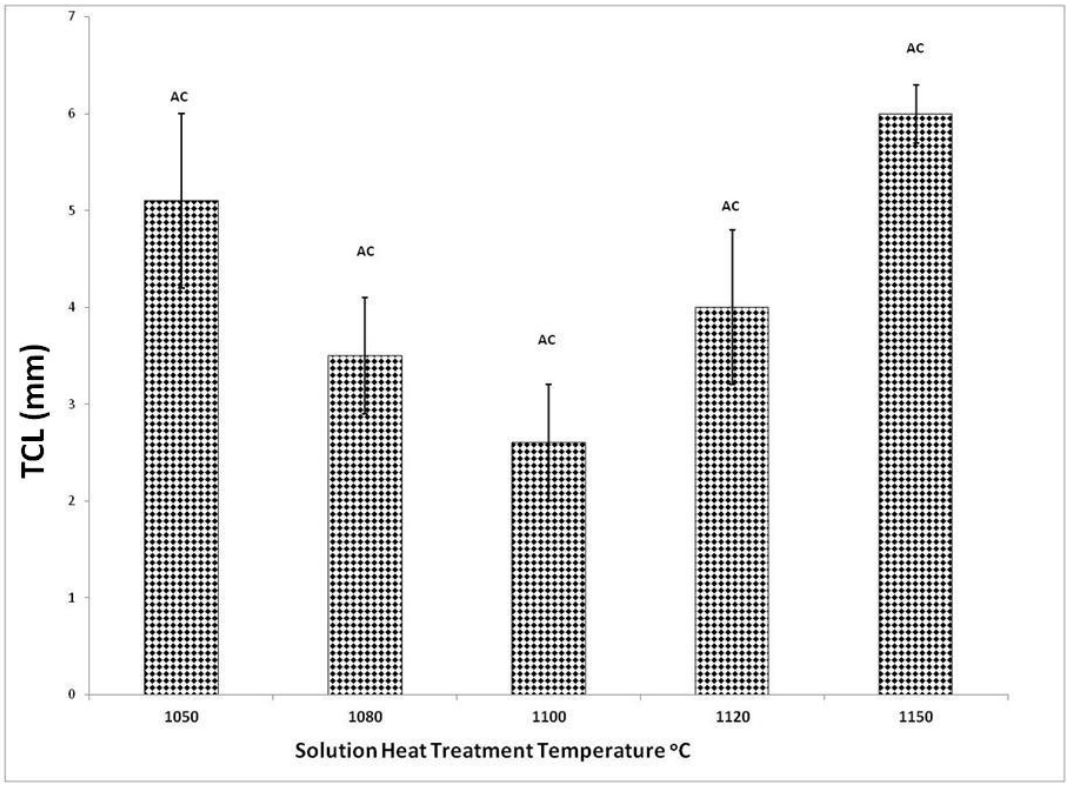

Figure 4-31: Variation of total crack length in Haynes alloy 282 subjected to pre-weld solution heat treatment at different temperatures followed by air-cooling (AC).

equilibrium elemental intergranular segregation [88, 164]. Therefore, non-equilibrium segregation of boron atoms, released by the dissolution of boride particles, to grain boundary regions can occur during pre-weld heat treatments at 1120^{o}C and above, the extent of which is expected to increase with temperature.

Secondary ion mass spectroscopy (SIMS) analysis of the alloy confirmed non-equilibrium intergranular segregation of boron in the alloy. An increase in heat treatment temperature resulted in increased non-equilibrium intergranular boron segregation during cooling (Figure 4-32). Non-equilibrium intergranular segregated boron atoms can damage cracking resistance by causing grain boundary liquation in the HAZ during welding, similar to what is caused by constitutional liquation of the M_5B_3 boride particles. This may explain the observed increase in HAZ cracking with an increase in pre-weld heat treatment temperature above 1120^{o}C. Moreover, non-equilibrium segregation is very sensitive to cooling rate from heat treatment temperature. Rapid cooling rates, such as the one involved during water quenching, can cause excess solute-vacancy complex to be "frozen in", and reduce non-equilibrium segregation, since sufficient time would not be available for the migration of the solute-vacancy complex to annihilation sites. At intermediate cooling rates, such as in air-cooling, vacancy-solute complexes can have sufficient time to migrate to annihilation sites, which may result in a more severe grain boundary elemental segregation. A much slower cooling rate like furnace cooling, however, can cause de-segregation of solute atoms, which would eventually result in less severe intergranular segregation [164]. Hence, a more severe grain boundary segregation of boron and concomitant higher level of HAZ cracking are expected in air-cooled than in water-quenched and furnace-cooled heat treated specimens. This was investigated in the

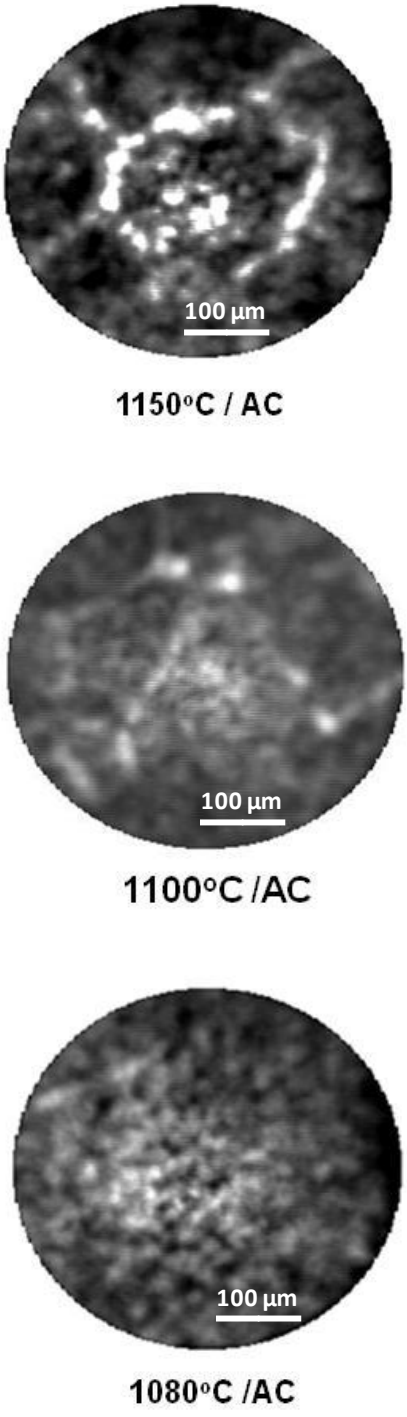

Figure 4-32: SIMS image showing increase in non-equilibrium segregation of boron with increase in heat treatment temperature in (air-cooling condition).

present work by examining the extent of HAZ cracking in ten weld cross-sections from each of the three different welded test coupons subjected to pre-weld heat treatment at 1150^{o}C and water-quenched, air-cooled and furnace-cooled. As shown by the results presented in Figure 4-33, the highest level of cracking occurred in the air-cooled condition. Notwithstanding the significantly higher hardness value of the furnace-cooled specimen compared to the air-cooled specimen (Figure 4-34), which normally could be expected to aid cracking, cracking is rather more in the air-cooled condition, where more non-equilibrium boron segregation is expected.

The results thus indicate that aside from constitutional liquation of the M_5B_3 borides, non-equilibrium segregation of boron atoms, released by the dissolution of the boride particles during pre-weld heat treatment, is another probable factor that renders the HAZ of the new Haynes alloy 282 to be susceptible to cracking. Accordingly, a viable approach to effectively reduce HAZ cracking in the alloy could be to reduce the volume fraction of the liquating M_5B_3 boride particles as much as possible, by pre-weld heat treatment while minimizing non-equilibrium boron segregation.

The results of the work performed in this research suggest that this is possible by using the pre-weld heat treatment at 1080-1100^{o}C as the results of the TCL from the three different welded test coupons (Figures 4-31 and 4-33) consistently show that the specimens subjected to pre-weld heat treatment at 1080-1100^{o}C produce the lowest level of HAZ cracking compared to other heat treatment conditions. Even though pre-weld heat treatment at 1080 -1100^{o}C reduces cracking, cracks still occur in these conditions.

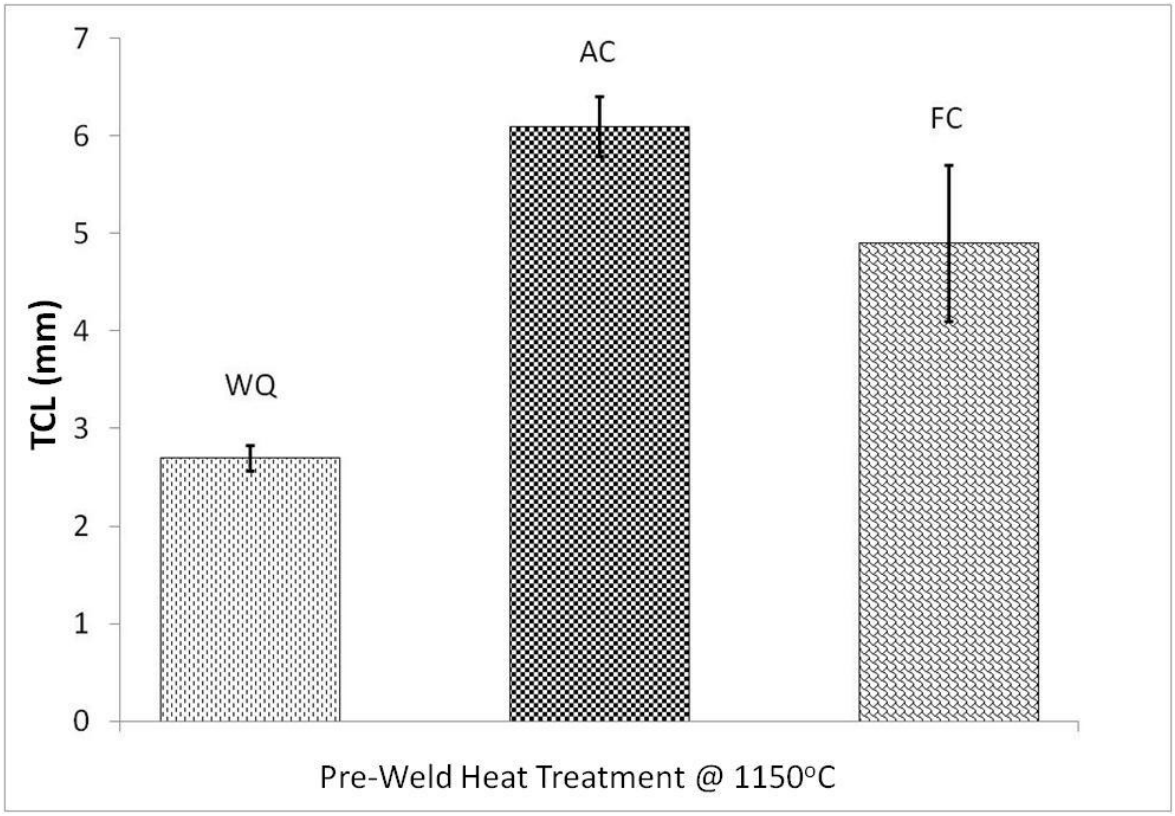

Figure 4-33: Total crack length in Haynes alloy 282 heat treated at 1150^{o}C and water quenched (WQ), air-cooled (AC) and furnace-cooled (FC).

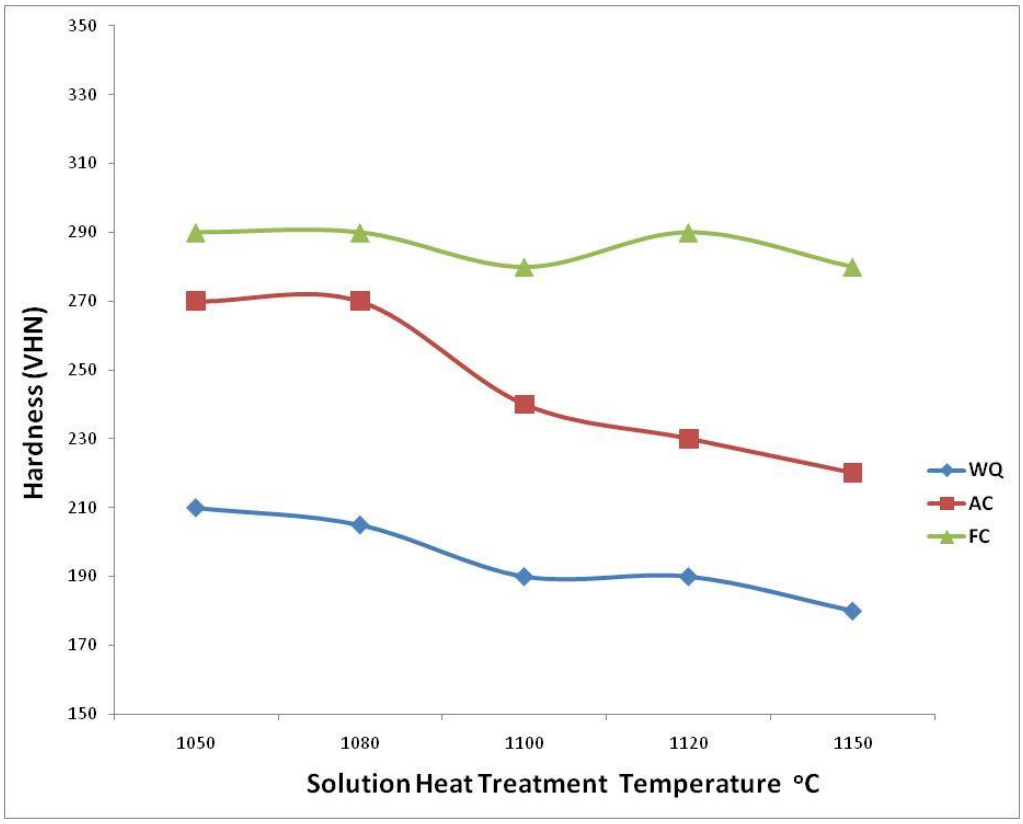

Figure 4-34: Variation of Haynes alloy 282 hardness with solution heat treatment temperature and for different cooling conditions.

4.5.5 Further Reduction in HAZ Cracking through Grain Refinement

Additional investigation was carried out in this research to study how to entirely prevent or minimize HAZ cracking in the 1080-1100^{o}C pre-weld heat treatment conditions. As stated earlier, grain boundary liquation is found to be the primary material cause of the susceptibility of the alloy to HAZ cracking. Also in section 4.5.3, using Equation (4.9) as proposed by Miller et al. [159], the relationship between tensile stress, σ, required to cause cracking by overcoming the surface γ_{sl} tension at the solid-liquid interface on liquated grain boundaries to the liquid film thickness *h*, implies that any factor that reduces the thickness of the intergranular liquid could also improve resistance to cracking by increasing the magnitude of stress required to cause intergranular cracks.

It is conceivable that the thickness of intergranular liquid, produced by the constitutional liquation of the few M_5B_3 borides present in the 1080^{o}C - 1100^{o}C condition, can be reduced by increasing the grain boundary surface area in the alloy to enable a wider spread of the intergranular liquid film. This idea was investigated by thermo-mechanically processing the alloy through cold-working and annealing heat treatment to refine its grain size and increase the grain boundary surface area. The average grain size was reduced from about 140 µm to about 40 µm and the material with refined grains was subjected to a pre-weld heat treatment at 1080^{o}C for 2 hrs, and laser beam welded. Interestingly, by refining the grains to effectively reduce the thickness of the intergranular liquid film produced by the liquation reaction of the few M_5B_3 borides in the 1080^{o}C condition produced crack-free welds in the new alloy for the very first time [165]. A micrograph that shows the crack-free weld region in the alloy with refined grains is presented as Figure 4-35.

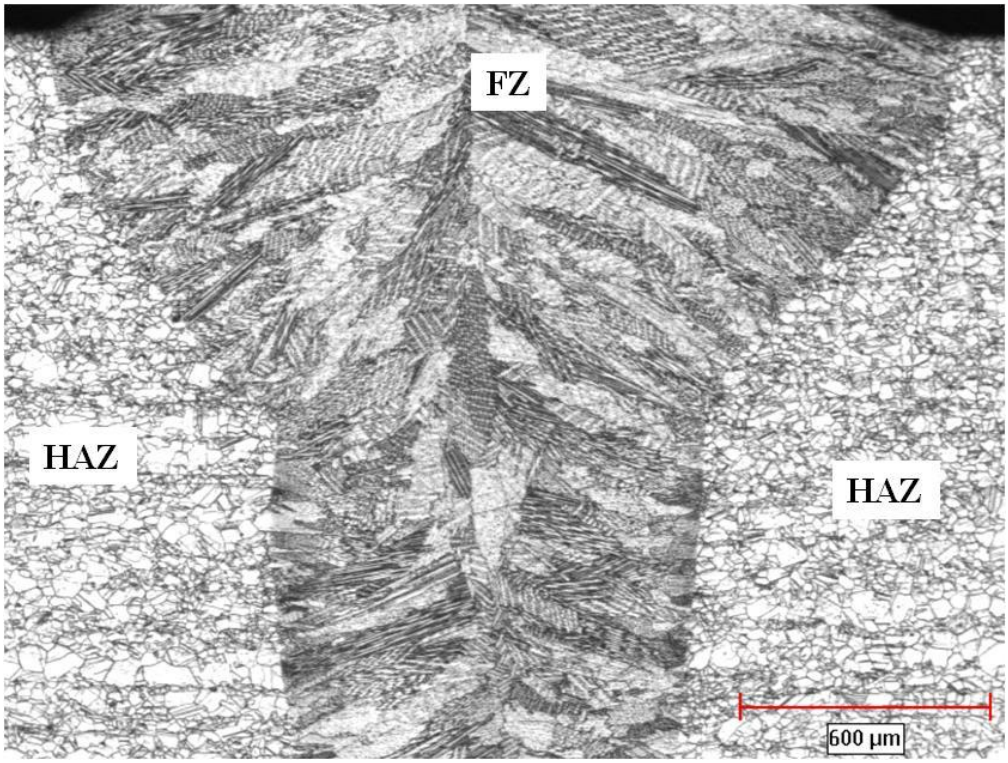

Figure 4-35: An optical micrograph showing typical crack-free weld section in Haynes alloy 282 with the refined grains.

It has been reported in the literature that weld cracking can be significantly influenced by material grain size [162, 166]. However, very limited information is available on how grain size affects susceptibility to cracking. In the present work, it was found that the formation of crack-free welds is not merely attributable to reduced grain size without considering the effects of grain refinement on the intergranular liquid produced by subsolidus liquation of the M_5B_3 borides. Gleeble hot ductility tests showed that enhanced resistance to cracking, through improved high temperature ductility, does not occur with reduction in grain size when the material was free of the M_5B_3 borides (Figure 4-36). In contrast, however, when the liquating M_5B_3 borides were present in the material, reduction in grain size produces a significant increase in high temperature ductility of the material (Figure 4-37). These, indicate that a crucial role of grain size in enhancing material resistance to HAZ cracking is by improving hot ductility through its influence on intergranular liquation. The understanding enabled by this study and the resultant approach that was found effective to produce crack-free welds through grain refinement coupled with an appropriate pre-weld heat treatment may also be applicable to other difficult-to-weld nickel-base superalloys.

In practice, subsequent to any fabrication and repair processes, welded superalloy components are subjected to post-weld heat treatment (PWHT) before being deployed for service. The PWHT is designed to restore the microstructure and properties of the welded material that may have been altered during the welding process by subjecting the welded material to standard heat treatment [167]. Like Haynes alloy 282, IN 718Plus is another newly developed γ’ precipitation hardened nickel-base superalloy for improved high temperature performance. A previous study by Idowu [168] showed that while

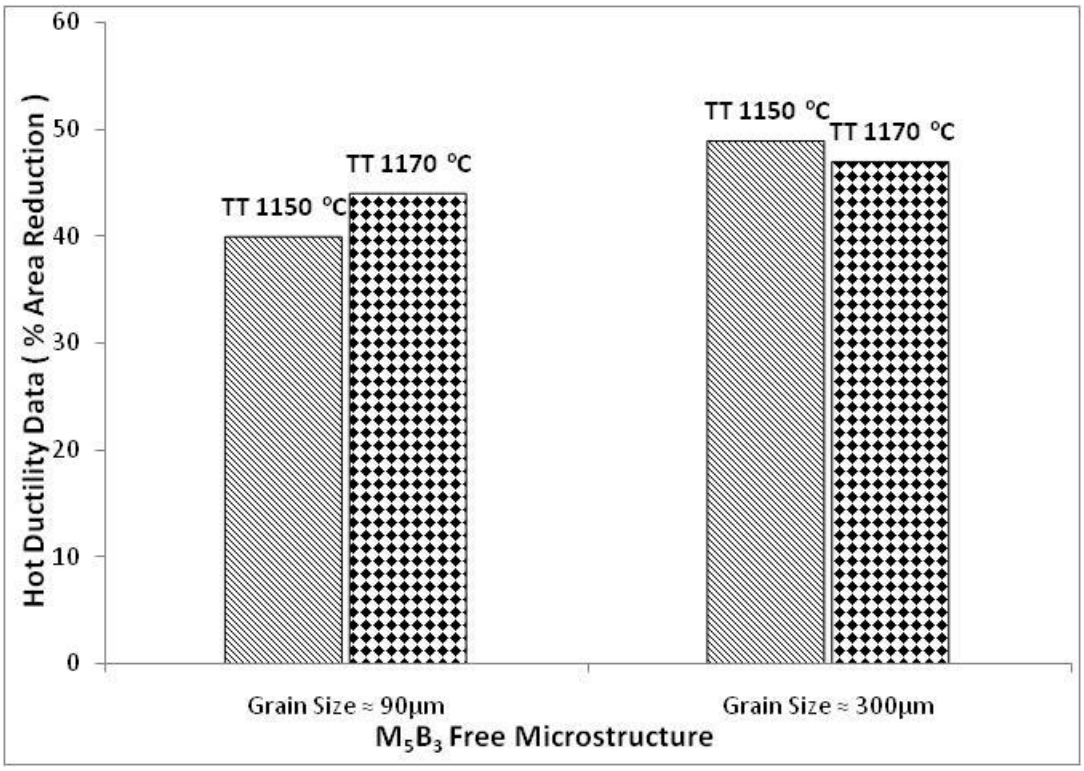

Figure 4-36: Hot ductility of Haynes alloy 282 without M_5B_3 borides and with different grain sizes at test temperature (TT) 1150^{o}C and 1170^{o}C.

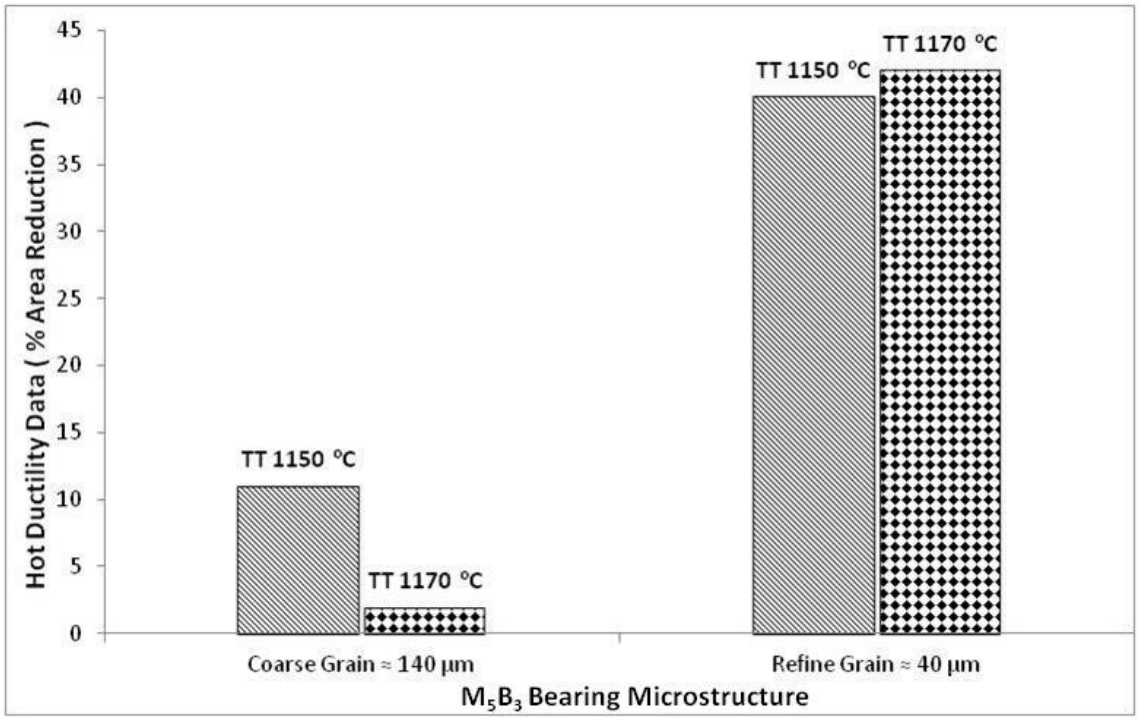

Figure 4-37: Hot ductility of Haynes alloy 282 containing M_5B_3 borides with different grain sizes at test temperature (TT) 1150^{o}C and 1170^{o}C.

IN 718Plus can also resist cracking during welding through the use of appropriate pre-weld heat treatment, the alloy cracks during subsequent PWHT. Therefore, the weldability study of Haynes alloy 282 performed in this work is considered incomplete without investigating the resistance of the alloy to cracking during PWHT.

To investigate the PWHT response of Haynes alloy 282, specimens subjected to pre-weld heat treatment at 1100^{o}C for 2 hours and the specimens with refined grains were post-weld heat treated (PWHTed) using the standard heat treatment for the alloy - 1150^{o}C for 2 hour/WQ + 1010^{o}C for 2 hour/AC + 788^{o}C for 2 hour/AC. Following the heat treatment, the occurrence of cracking in PWHTed specimens was investigated. Figure 4-38 shows a typical general overview of the PWHTed laser welded Haynes alloy 282 subjected to pre-weld heat treatment at 1100^{o}C. Microscopic examination of the PWHTed specimens did not reveal any cracks in the FZ, and in the HAZ of the materials with refined grains. Also, compared to the as-welded condition, no noticeable increase in cracking was observed in the specimen subjected to pre-weld heat treatment at 1100^{o}C (Figure 4-39). The results, thus, indicate that the pre-weld heat treated Haynes alloy 282 specimens are resistant to cracking during PWHT. This is in contrast to the reported case of IN 718Plus, which even though resists cracking during welding, cracks during PWHT [168].

Previous investigations on PWHT cracking in nickel-base superalloys [10,102,106,169-171] indicate that PWHT cracking occurs when aging contraction stresses, which develop by precipitation of γ' particles during PWHT, are preferentially relaxed in the HAZ, that has already been embrittled by various metallurgical reactions during welding. It has been generally reported that the susceptibility of γ' precipitation

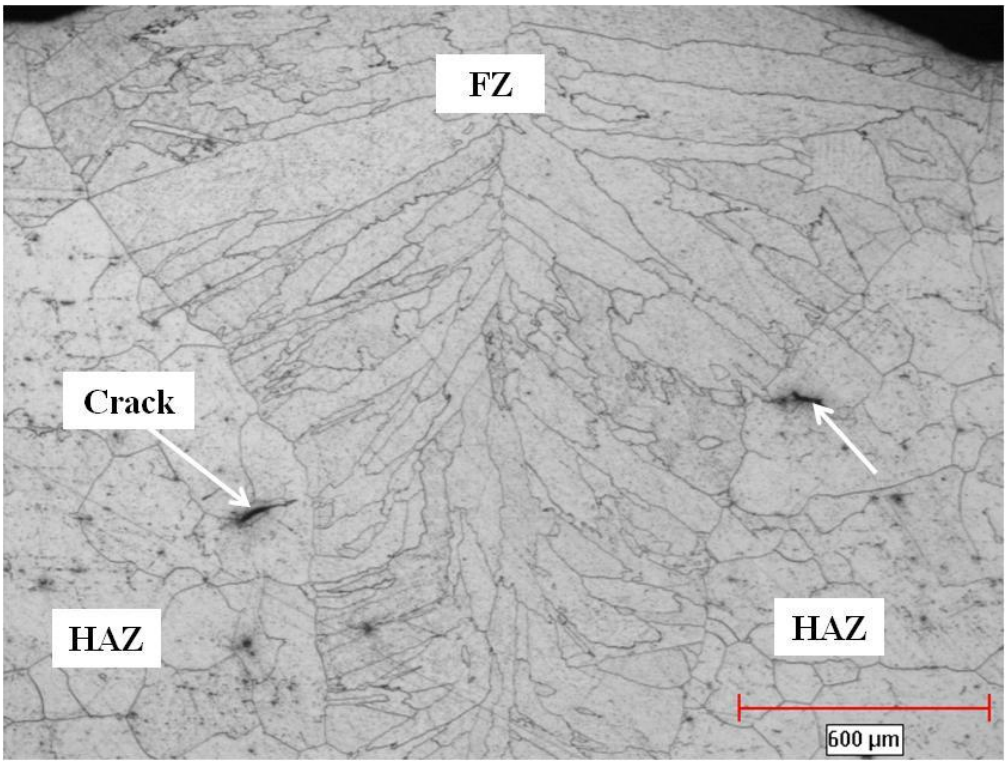

Figures 4-38: Optical micrograph of PWHTed laser welded Haynes alloy 282 subjected to pre-weld heat treatment at 1100^{o}C showing the general overview of PWHTed material.

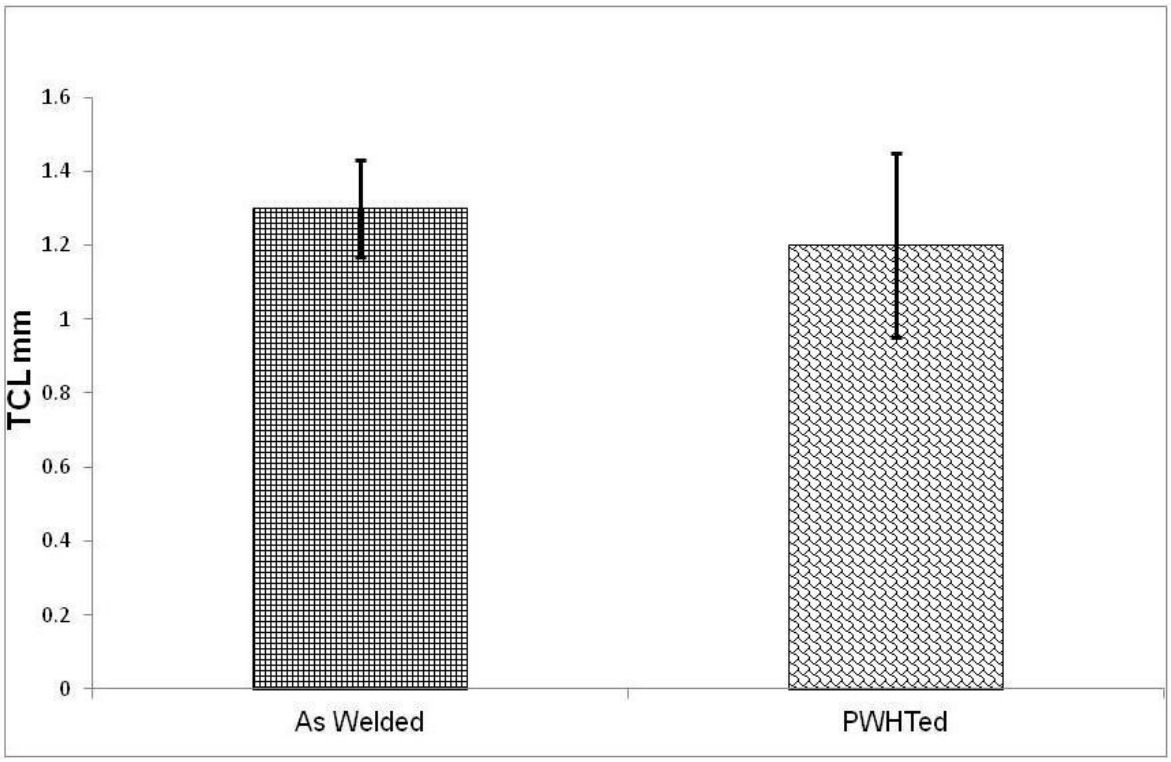

Figure 4-39: Total crack length in Haynes alloy 282 in as-welded and PWHTed conditions.

strengthened superalloys increases with increases in the concentration of γ' forming elements, Al and Ti. The total wt. % of Al + Ti in Haynes alloy 282 (3.6%) is higher than that in IN 718Plus (2.2%).

Notwithstanding the higher γ' content in Haynes alloy 282, the alloy did not crack during PWHT, in contrast to IN 718Plus, which has a lower γ' content and cracks during PWHT. A major factor identified by Idowu [168], which contributes to cracking in IN 718Plus during PWHT is the extensive formation of delta (δ) phase precipitates from Laves phase particles along the grain boundaries of the material. Precipitates of Laves phase and delta phase are known to be very brittle and have weak interfaces with the γ matrix [172], which aid easy crack initiation and /or propagation during PWHT as well as confer inferior mechanical properties on weldment. A major forming element for Laves phase and δ phase in superalloys is niobium [162, 166].

The Haynes alloy 282 was developed with its composition free of Nb and as such, the Laves phase and δ phase which were reported to reduce resistance to PWHT cracking in IN 718Plus are not present in the material [Figure 4-40]. This preclusion of Nb in the chemical composition of Haynes alloy 282 seems to aid the resistance of the material to PWHT cracking. Therefore, the results show that the benefit of the new approach developed in this research for preventing cracking in Haynes alloy 282, during welding, is not undermined by formation of cracking in welded material during PWHT.

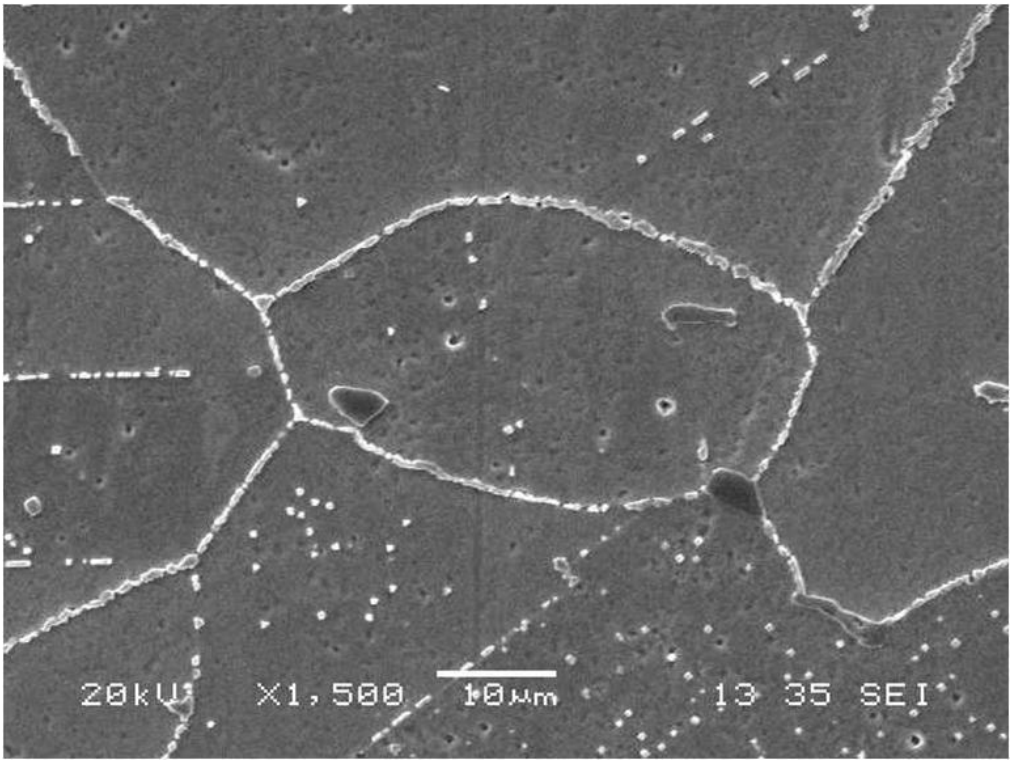

Figure 4-40: SEM Image of PWHTed-HAZ microstructure of Haynes alloy 282.

CHAPTER 5

Summary and Conclusions

The major findings and conclusions in the research are summarized as follows,

1) The microstructure of Haynes alloy 282 in its standard condition consists of a gamma (γ) solid solution matrix and MC carbides (M mostly being Ti and Mo), $M_{23}C_6$ carbides and M_5B_3 borides, which are identified and reported for the first time in the material in this study.

2) A DSC analysis shows that the solidus, liquidus and the equilibrium solvus of the main strengthening phase (γ') in Haynes alloy 282 are ~ 1244^{o}C, ~1360^{o}C, and ~ 1000^{o}C, respectively.

3) Microstructural study of laser welded specimens shows that the alloy cracks during welding and the cracks are mainly confined to the HAZ while the FZ is crack free.

4) The micro-segregation pattern observed during solidification in the weld FZ shows that only Ti and Mo, out of the major metallic alloying elements in the material, exhibit substantial partitioning into the interdendritic liquid.

5) Examination and analyses by TEM reveal that secondary solidification reaction products formed in the FZ from the interdendritic liquid, are Ti-Mo

rich MC-type carbide particles, while the γ-γ' eutectic micro-constituents that often form in nickel-base superalloys are not observed.

6) Modified primary solidification path due to carbon addition can be used to explain the preclusion of the γ-γ' eutectic transformation products in the newly developed Haynes alloy 282.

7) Careful microstructural study of laser welded specimens and Gleeble thermo-mechanical simulation revealed that a fundamental mechanism of HAZ cracking in Haynes alloy 282 involves grain boundary liquation caused by the subsolidus liquation reaction of the newly identified M_5B_3 boride particles.

8) An increase in the magnitude of heat input during laser welding results in the reduction of the extent of HAZ liquation cracking. This is attributed to a combination of :

   (i) possible increase in the magnitude of tensile stress required to induce cracking due to reduction in intergranular liquid film thickness enabled by longer available time for the re-solidification of intergranular liquid in high heat input welds, and

   (ii) lower level of thermally generated welding stress caused by shallower temperature gradient in the HAZ associated with high heat input welds.

9) Although, it has been observed that reduction in heat input increases cracking, low heat input laser welds are generally preferred over high heat input welds. In order to minimize HAZ liquation cracking in the alloy during low heat input welding, microstructural modification of the material by pre-weld heat treatment was studied. Complete dissolution of the liquating M_5B_3 borides by pre-weld heat treatment exacerbates, instead of lessening the susceptibility of the alloy to HAZ cracking, which is attributable to the non-equilibrium intergranular segregation of boron atoms released by the dissolution of the boride particles.

10) SIMS analyses confirm that increase in the pre-weld heat treatment temperature increase non-equilibrium intergranular boron segregation in the Haynes alloy 282.

11) Carefully designed pre-weld microstructural modification by heat treatment at 1080^oC – 1100^oC is capable of minimizing HAZ cracking by reducing the volume fraction of the M_5B_3 borides while also minimizing non-equilibrium grain boundary boron segregation.

12) Further improvement in cracking resistance is produced by subjecting the material to thermo-mechanically induced grain refinement coupled with pre-

weld heat treatment at 1080^{o}C which for the first time resulted in crack-free welds in Haynes alloy 282.

13) Whilst grain size has been previously reported to influence weld cracking in superalloys, the results of Gleeble hot ductility test in the present work indicate that a crucial role of grain size in HAZ cracking is through its influence on intergranular liquation, which affects material hot ductility.

14) Microstructural study of specimens laser welded in the pre-weld heat treatment condition developed in this work and subsequently subjected to PWHT does not show any occurrence of cracking during PWHT.

15) The benefit of the approach developed in this study for preventing weld cracking in Haynes alloy 282 during welding, is not undermined by cracking during PWHT.

CHAPTER 6

Suggestions for Future Work

1. In order to evaluate the effects of the preclusion of weld cracking by the new approach developed in this research on the mechanical properties of Haynes alloy 282, various mechanical testing of welded and PWHTed specimens of the material are suggested, including ambient and elevated temperature low-cycle fatigue and high cycle, thermo-mechanical fatigue and creep test.

2. Grain boundary liquid film migration (LFM) is a fundamental solidification phenomenon through which nickel-base superalloys can resist HAZ liquation cracking [160, 173]. A more extensive intergranular LFM was noticed in conditions with low non-equilibrium grain boundary boron segregation compared to those with higher levels of non-equilibrium grain boundary boron segregation. Therefore, the influence of non-equilibrium grain boundary segregation of boron atoms on the LFM solidification phenomenon in superalloy, can be further investigated. This may offer deeper insight into the mechanisms through which non-equilibrium grain boundary boron segregation promotes susceptibility to HAZ liquation cracking in nickel-base superalloys.

REFERENCES

[1]. Sims, C.T., Stoloff, N.S., Hagel, W.C., (Eds)., Superalloys II: "High Temperature Materials for Aerospace and Industrial Power", John Wiley & Sons - Interscience publication, 1987: p. 3

[2]. Pike, L.M., "Development of fabricable gamma-prime (γ') strengthened superalloy", Superalloy 2008. (Eds., Reed, R.C., Green, K. A., Pierre, C., Gabb, T. P., Fahrmann, M. G., Huron, E. S. and Woodard, S. A.), TMS 2008: p. 191

[3]. Ojo, O.A., "On Liquation cracking of Cast Inconel 738LC Superalloy Welds", PhD Thesis, University of Manitoba, 2004

[4]. Vishwakarma, K., "Microstructural Analysis of Weld Cracking IN 718Plus Superalloy", PhD Thesis, University of Manitoba, 2007

[5]. Huang, X., "A microstructural study of heat affected zone microfissuring of electron beam welds in cast alloy 718", PhD Thesis, University of Manitoba, 1994

[6]. Owczarski, W.A., "Process and Metallurgical Factors in Joining Supperalloys and other High Service Temperature Materials", SUPERALLOYS Source Book, M.J. Donachie, Jr. ed., American Society for Metals, Metals Park, 1984, p. 369

[7]. Bradley, E.F., A Technical Guide, ASM International, Metal Park OH, 1998: p. 58

[8]. Alloy digests Haynes 282: A publication of ASM International material park, Ohio 44073-0002, U.S.A. 2006

[9]. Pike, L.M., "Low-Cycle Fatigue behavior of Haynes 282", ASME Turbo Expo 2007, Montreal Canada, paper no. GT2007-28267, 2007.

[10]. Duvall, D.S., Owczarski, W.A., "Studies of PWHT cracking in Nickel-Base Alloy", Weld. Res. Suppl., Weld. J., 48 (1), 1969: p.10s

[11]. Penkeller, H.J., Crzyrska-Filemonowicz, A, Wosik, J., "Quantitative microstructural characterization of Ni-base superalloys", Material Chemistry and Physics, 81, 2003: p. 417

[12]. D'Annessa, A.T., Owens, J.S., "Procedure for avoiding heat - treat cracking in nickel-base superalloy weldment", Technical report AFML-TR-70-224, Air Force Materials laboratory, Wright-Patterson air Force base, Ohio, 1970.

[13]. Smith, W.F., "Structure and properties of Engineering alloys", 2nd edition, New York McGraw-Hill, 1993: p.504

[14]. Reed, R.C., "The Superalloy: Fundamental and Applications", Cambridge University Press, 2006: p. 35

[15]. Decker, R.F., "Strengthening Mechanism in Nickel-Base Superalloys", Climax Molybdenum Company Symposium, Zurich 1969.

[16]. Mott, N.F., "Imperfections in nearly perfects crystals". W. Shockley (Ed.), John Willey and Sons, New York, 1952, p. 173.

[17]. Mott, N.F., Nabarro, F.R.N., "Report of conference on strength of solids", Phys. Sci. 1948: p. 1.

[18]. Ardell, A.J., "Precipitation Hardening", Metall. Trans., 16A, 1985: p. 2131-2165.

[19]. Fayman, Y.C., "Gamma - Gamma prime partitioning behavior in Waspaloy", Materials Science and Engineering, 82, 1986: p. 203.

[20]. Durand-Charre, M., "The microstructure of superalloys", translated by J.H. Davidson, 1997.

[21]. Donachie, M.J., Donachie S.J., "Superalloy a Technical Guide", 2nd edition, ASM International, Materials Park, OH, 2002: p. 211

[22]. Hagel, W.C., Beattie, H.J., "Iron and Steel Institute Special Report", London 64, 1959: p. 98.

[23]. Raynor, D., Silcock, J.M., "Strengthening mechanism in gamma-prime precipitating alloys", Met. Sci. J. 4, 1970: p.121.

[24]. Orowan, E., "Symposium on Internal Stresses in Metals", Institute of Metals, London, 1948: p. 45

[25]. Larson, J.M., "Carbide morphology in P/M IN-792", Metall. Transac., 7A(10), 1976: p. 1497

[26]. Brown, L.M., Ham, R.K., "Strengthening methods in crystals", Elsevier Amsterdam, 1971: p. 9

[27]. Decker, R.F., Sims, C.T., "The Metallurgy of Nickel-base alloys". The Superalloys. Sims, T.C and Hagel, W.C. Eds., John Wiley and Sons, New York, 1972: p 33.

[28]. Ross, E.W., Sims, C.T., "Nickel-Base Alloys". The Superalloys. Sims T.C. and Hagel, W.C. Eds. John Wiley and Sons, New York, 1987: p. 97.

[29]. Antolovich, S.D., Camphell, J.E., "Fracture properties of superalloys", Superalloy source book. A collection of outstanding articles from the technical literature. ASM Metal park: Ohio, 1984, p 112.

[30]. Hoffelner, W., Kny., E.S, Stickler., R., McCall, W.J.Z., "Effect of Aging treatments on the microstructure of the Ni-based superalloy IN-738", Werktofftech, 10(84), 1979.

[31]. Zang, H.R., Ojo, O.A., Chaturvedi, M.C., "Nanosize boride particles in heat treated nickel-base superalloy", Scriptal Materialla. 58, 2008: p.167.

[32]. Shidu, R.K., Ojo, O.A., Chaturvedi, M.C., "Microstructural response of directionally solidified Rene 80 superalloy to Gas tungsten Arc welding", Metal & Mater Trans. A, 40A, 2009: p. 150.

[33]. Mazubuchu K., "Encyclopedia of Materials Science and Engineering", M.B. Bever (Ed), 7, 1986: p. 5280

[34]. Kou, S., "Welding Metallurgy", 2nd Edition, John Wiley and Sons Inc., Hoboken, 2003

[35]. Electron Beam Welding, ASM Handbook, "Welding, Brazing and Soldering", ASM International, 6, 1993: p. 254.

[36]. Salim, P.R., Schubert, F., "Solidification phenomena and properties of cast and welded material", Proc. Conf. on Solidification and Casting of metals, Sheffield England, 1979: p.389.

[37]. David, S.A., Viteck, J.M., "Principle of weld solidification and microstructure in International trends in Welding Science Technology". 1992: p. 147

[38]. Lancaster, J.F., "Metallurgy of Welding". Chapman and Hall, New York, 1993

[39]. Radhakrishna, C., Rao, K.P., "The formation and control of Laves phase in superalloy 718 welds", Journal of Materials Science, 32, 1997: p. 1977

[40]. Solomon, H.D., in Treatise on materials science and technology: "Embrittlement of engineering alloys", Briant, C.L and Banjerji, S.K. (Eds.), Academic Press, New York, 1983: p. 525.

[41]. Savage, W.F., Nippes, E.F., Erickson, J.S., "Solidification mechanisms in fusion welds", Weld. J., 55, 1976: p. 213s.

[42]. Savage, W.F., Nippes, E.F., Miller, T.W., "Microsegregation in partially melted regions in 70Cu-30Ni weldments", Weld. J., 55, 1976: p. 181s.

[43]. Savage, W.F., Nippes, E.F., Miller, T.W., "Microsegregation in 70Cu-30Ni weld metal", Weld. J., 55, 1976: p. 165s.

[44]. Savage, W.F., Nippes, E.F., Szekeres, E.S., "Study of weld interface phenomena in a low alloy steel", Weld. J., 55, 1976: p. 260s.

[45]. Savage, W.F., Houdremont lecture: "solidification, segregation and weld imperfections", Weld. World, 18, 1980: p. 89.

[46]. Savage, W.F., Lundin, C. D., Aronson, A.H., "Weld metal solidification mechanics", Weld. J., 44(4), 1965: p. 175s.

[47]. Boettinger, W. J., Coriell, S.R., Sekerka, R.F., "Mechanism of microsegregation-free solidification", Mater. Sci., Eng., 65(1), 1984: p. 27

[48]. Cieslak, M.J., "Cracking Phenomenon associated with Welding", ASM Handbook, Welding, Brazing and Soldering, ASM International, 16, 1993: p. 88.

[49]. Borland, J.C., "Generalized theory of super-solidus cracking in welds (and Castings)", Brit. Weld. J., 7(8), 1960: p. 508.

[50]. Singer, A.R.E., Jennings, P.H., "Hot shortness of some aluminum alloy, J. Inst. Metals", 73, 1947: p.197.

[51]. Dowd, J.D., "Weld cracking of aluminum alloy", Weld. J., 31(10), 1952: p 448.

[52]. Cross, C.E., Tack, W.T., Loechel, L.W., "Aluminum Weldability and hot tearing theory", in Proc. Materials Weldability Symposium, Detroit, MI, ASM International Publ. Metal Park, 1990.

[53]. Nakata, K., Matsuda, F., "Evaluations of ductility characteristics and cracking susceptibility of Al alloy during welding". Trans. JSRI, 24, 1995: p.83.

[54]. Richards, N.L., Nakkalil, R., Chaturvedi, M.C., "The Influence of EBW parameters on HAZ microfissuring in Incoloy 903". Metall. Mater. Trans. A. 25A 1994: p. 1733.

[55]. Koren, A., Roman, M., Kaufman, A., Weisshaus, I., "Improving the weldability of Ni-base superalloy IN 713C", Weld. J., 61 (11), 1982: p. 348.

[56]. Vero, J., "Hot tearing of Aluminum alloys", Metal Industry, 48(17), 1936: p.191.

[57]. Singer, A.R.E., Jennings, P.H., "Hot shortness of Aluminum silicon alloys of commercial purity", J. Inst. Metals, 1946: p.16

[58]. Pumphrey, W.I., Jennings, P.H., "A consideration of the nature of brittleness at temperatures above the solidus in casting and welds in aluminium alloys", J. Inst. Metals, 75, 1948: p. 235.

[59]. Singer, A.R.E., Cotrell, S.H., "Properties of Al- Si Alloys at the temperatures in the region of solidus", JOIM, 73, 1946: p. 33.

[60]. Medovar, B.I., "Austenitic Steels and Alloys, Alloyed with Boron for Welded Structures", Automat Weld , 7, 1954: p. 12

[61]. Pellini, W.F., "Strain theory of Hot Tearing", Foundry, 80, 1952: p. 192.

[62]. Matsuda, F., Nakagawa, H., Sodara, K., “Dynamic observation of solidification and solidification cracking during welding with optical microscope”. Transaction of the JWRI, 11(2), 1982: p. 67.

[63]. Radhakrishnan, B., Thompson, R.G., “A phase diagram approach to study liquation cracking in alloy 718”. Metall. Trans. 22A, 1991: p. 887.

[64]. Chaturvedi, M.C., “Liquation cracking in Heat Affected Zone in Ni-Superalloy Welds”, Materials Science Forum, 546-549, 2007: p. 1163.

[65]. Owczarski, W.A., Duvall, D.S., “Sullivan, C. P., A model for Heat Affected Zone cracking in Nickel-Base Superalloy”, Welding J., 50, 1971: p. 145.

[66]. Lin, W., Lippold, J.C., Baeslack, W.A., “Analysis of weldability testing technique for heat affected zone liquation cracking” Weld. J., 71(4), 1993: p. 135s.

[67]. Pepe, J.J., Savage, W.F., “Effect of Constitutional Liquation in 18-Ni maraging steel weldment”. Weld. J., 46, 1967: p. 411s.

[68]. Vincent, R., “Precipitation around welds in nickel-based superalloy IN 718”. Acta Metall., 33, 1985: p.1205.

[69]. Lin, W., “A methodology for quantifying heat affected zone liquation cracking susceptibility”. PhD Dissertation. The Ohio State University, Columbus, Ohio 1991.

[70]. Nakkalil, R., Richards, N.L., Chaturvedi, M.C., “Microstructural Characterisation of Incoloy 903 Weldments”. Metall. Trans. A., 24A, 1993: p 1169

[71]. Ojo, O.A., Richards, N.L., Chaturvedi, M.C., “Study of Fusion Zone and Heat-Affected Zone Microstructures in Tungsten inert Gas-Welded Inconel 738LC Superalloy”, Metall. Trans. A, 37A, 2006: p 421.

[72]. Weiss, B., Grotke, G.E., Stickler, R., "Physical Metallurgy of Hot Ductility Testing", Weld. J., 49, 1970: p 471s.

[73]. Radhakrishnan, B., Thompson, R.G., "The effect of Weld Heat Affected Zone (HAZ) Liquation Kinetics on Hot-Cracking Susceptibility of Alloy 718", Metall. Trans. A, 24A, 1993: p. 1409

[74]. Vishwakarma, K.R., Richards, N.L., Chaturvedi, M.C., "HAZ microfissuring in EB Welded Allvac 718Plus Alloy", in: E.A. Loria (Ed.), Superalloys 718, 625, 706 and Derivatives 2005, The Minerals, Metals and Materials Society, 2005: p. 637.

[75]. Brooks, J.A., "Effect of Alloy Modifications on HAZ cracking of A-286 Stainless Steel", Weld. J., 53, 1974: p 517s

[76]. Aronson, A.N., "Constitutional liquation in the Iron-Iron Carbide system", MSc Thesis, Rensselaer Polythenic Institute., Troy, New York, 1963

[77]. Tamura, H., Wantanabe, T., "Mechanism of liquation cracking in the weld heat-affected zone of austenitic stainless steel". Trans. of the Japan Welding Soc., 2, 1973: p. 3.

[78]. Mclean, D., "Grain boundaries in Metals", Clarendon Press, Oxford, 1957

[79]. Hondros, E.D., Seah, M.P., "Interfacial and Surface microchemistry, in Physical Metallurgy", Ed. Cahn, R.W., 3rd Edition, North Holland, Amsterdam 1984: p. 855.

[80]. Mclean, M., Strang, A., "Effects of trace elements on mechanical properties of superalloys". Met. Technol., 11, 1984: p. 454

[81]. Westbrook, J.H., Aust, K.T., “Solute hardening at Interfaces in high purity lead, Acta Metall.”, 11, 1963; p. 1151.

[82]. Aust, K.T., Hanneman, R.E., Nissen, P., Westbrook, J.H., “Solute induced hardening near grain boundaries in zone refined materials”, Acta Metall., 16, 1968; p. 291.

[83]. Eadie, R.L., Aust, K.T., “Solute induced grain boundaries hardening in Aluminum”, Scripta Metall., 4(8), 1970: p. 641.

[84]. Aust, K.T., “Selective segregation at grain boundaries”, Canadian Metallurgical Quarterly, 13(1), 1974: p. 133.

[85]. Paine, D.C., Weatherly, G.C., Aust, K.T., “A STEM study of grain boundary segregation in Al-6.5 wt. % Mg Alloy”, J. Mater. Sci., 21(12), 1986: p. 4257-4261

[86]. Anthony, T.R., “Solute segregations in vacancy gradients generated by sintering and temperature changes”, Acta Metall., 17(5), 1969: p. 603.

[87]. Faulkner, R.G., Jones, R.B., Lu, Z., Flewitt, P.E.J., “Grain boundary impurity segregation and neutron irradiation effects in Ferritic alloys”, Phil. Mag., 85(19), 2005: p. 2065.

[88]. Karlsson, L., Norden, H., “Non-Equilibrium grain boundary segregation of boron in austenitic stainless steel, II fine scale segregation behaviour, precipitation behaviour and distribution of elements IV”, Acta Metall., 36(1), 1988: p.13.

[89]. Chen, W., Chaturvedi, M.C., “Grain boundary segregation of boron in IN 718”, Metall. Mater. Trans. A., 29A, 1998: p.1947.

[90]. Guttmann, M., “Equilibrium segregation in a ternary solution: A model for temper embrittlement”, Surf. Sci., 53, 1975: p. 213.

[91]. Kujanpaa, V.P., David, S.A., White, C.L., "Characterisation of Heat Affected Zone cracking in austenitic stainless steel welds", Weld., J., 66, 1987: p 221s.

[92]. Huang, X., Chaturvedi, M.C., "An investigation of microstructure and HAZ microfissuring of cast alloy 718, 625, 706 and various derivatives" (Ed. Loria E.A), 1994: p. 871.

[93]. Huang, X., Chaturvedi, M.C., Richards, N.L., Jackman, J., "The effects of grain boundary segregation of boron in cast alloy 718on HAZ microfissuring- A SIMS analysis". Acta Materialia 45(8), 1997: p. 3095.

[94]. Benhadad, S., Richards, N.L., Chaturvedi, M.C., "The influence of minor elements on weldability of IN 718 type superalloy". Metallurgical and Materials Transaction A., 33A, 2002: p.2005

[95]. Guo, H., Chaturvedi, M.C., Richards, N.L., "Effect of Sulphur on hot ductility and HAZ microfissuring in alloy 718 weld". Sci. and Technol. of Welding and Joining, 5(6), 2000: p.378

[96]. Guo, H., Chaturvedi, M.C., Richards, N.L., McMahon, G.S., "Interdependence of character of grain boundaries, intergranular segregations of boron and grain boundary liquation in simulated weld heat affected zone in IN 718", Scripta Mater., 40(3), 1999: p. 383

[97]. Guo, H., Chaturvedi, M.C., Richards, N.L., "Effect of Boron concentration and grain size on Weld Heat Affected Zone Microfissuring in IN 718 base superalloys", The Sci. and Technol. of Welding and Joining, 4(4), 1999: p. 257.

[98]. Idowu, O.I., Ojo, O.A., Chaturvedi, M.C., "Crack free Electron beam welding of Allvac 718Plus Superalloy". Weld. J., 88 (8) 2009: p. 179s.

[99]. Vishwakarma, K., Chaturvedi, M.C., "A study of HAZ Microfissuring in a newly developed Allvac 718 Plus Superalloy", Superalloy 2008 TMS. p. 241.

[100]. Thamburaj, R., Goldak, J.A., Wallace, W., "Influence of chemical composition on post-weld heat treatment cracking in Rene 41", SAMPE Quartely, 10(4), 1979: p. 6

[101]. Kayacan, R., Varol, R., Kimilli, O., "The effects of pre- and post-weld heat treatment variables on the strain-age cracking in welded Rene 41 components", Materials Research Bullettin 39, 2004: p. 2171.

[102]. Carlton, J.B., Prager, M., "Variables Influencing the Strain Age Cracking and mechanical properties of Rene 41and related alloys", Weld Res. Council Bull., 150, 1970: p. 13

[103]. Hughes, W.P., Berry, T.F., "Study of strain age cracking characteristic in welded Rene 41", Weld. J., 46 (8), 1967: p. 361s.

[104]. Dix, A.W., Savage, W.F., "Factors influencing strain age cracking in IN X-750", Weld. J., 50(6), 1971: p. 247s.

[105]. Franklin, J. E., Savage, W. F., "Stress relaxation and strain-age cracking in Rene 41 weldments", Weld. J., 53(9), 1974: p. 380s.

[106]. Prager, M., Sines, G., "Mechanism of cracking during postwelding heat treatment of Ni-base alloy", Weld Res. Council Bull., 150, 1970: p. 24.

[107]. Kelly, T.J., "Welding metallurgy of investment cast Ni-based superalloys in Proc. Symp. on weldability of materials", Detroit, MI, ASM Inter. Patterson, R.A, and Mahin, K.W, (Eds)., Materials park, OH, 1990: p.151.

[108]. Jordan, D. E., Richards, E. G., in "Heat Treatment Aspects of Metal Joining Processes", The Iron and Steel Institute, London, 1972: p. 71.

[109]. Burdekin, F.M., in "Heat Treatment Aspects of Metal Joining Processes", The Iron and Steel Institute, London, 1972: p. 6.

[110]. Thompson, E.G., Nunez, S., Prager, M., "Practical Solution to strain age cracking of Rene 41", Weld. J., 47 (7), 1968: p. 299s.

[111]. 1976 Welding Handbook, 1, 7th Edition, American Welding Society, Miami.

[112]. Baeslack III, W.A., Lippold, J.C., "Evaluation of weldability testing techniques", Proceeding of EWI, North American Welding research seminar on 'The influence of new materials development on weldability', Columbus, Ohio. 1987.

[113]. Savage, W.F., Lundin, C.D., "Varestraint Test", Weld. J., 44(10), 1965: p. 433s.

[114]. Kriescher, C.H., "A critical analysis of the weld HAZ hot ductility Test", Weld J., 42, 1963: p. 49s.

[115]. Lundin, C.D., Qiao, C.Y.P., Gull, T.P.S., Goodwin, G.M., "Hot ductility and hot cracking behavior of modified 316 stainless steel designed for high-temperature service", Weld. J., 72(5) 1993: p. 189s

[116]. Donati, J.R., Zacharie, G., "Evaluation of the tendency for hot cracking in the heat affected zone of welded 18Cr-10Ni Austenitic steels", Review de Metallurgie, 71(12), 1974: p. 905.

[117]. Nippes, E. F., Savage, W. F., Bastian, B.J., Mason, H. F., Curran, R. M., "Investigation of hot ductility of high temperature alloys", Weld. J., 34, 1955: p.183s.

[118]. Muesch, H., "Welding of Alloyed ferritic and martensitic steel in piping system for high temperature", Mannesmann Research Institute Duisburg/Metallurgical Soc. of AIME, 1984: p. 253.

[119]. Williams, C.S., "Steel strength and ductility response to arc-welding thermal cycle", Weld J., 42(1), 1963: p.1s.

[120]. Duval, D.S., Owczarski W.A., "Further Heat Affected Zone Studies in Heat-Resistant Nickel Alloy", Weld. J., 46 (9), 1967: p. 63, 73, 93.

[121]. Qian, M., "An Investigation of repair weldability of Waspaloy and Alloy 718". PhD Dissertation. The Ohio State University, Columbus, Ohio, 2001.

[122]. Scott, W.S., "A study of weld HAZ liquation cracking in Cast Ni-based superalloy". PhD Dissertation. The Ohio State University, Columbus, Ohio, 1991

[123]. Andersson, J., Sjoberg, G., Chaturvedi, M., " Hot ductility study of Haynes 282 superalloy", 7th International Symposium on Superalloy 718 and Derivatives 2, p. 539, 2010.

[124]. Chirieleison, G., Snyder, L., Hansen, T., Sharma, R., White, H., " The effect of ageing heat treatments on the mechanical properties of gamma prime strengthened nickel based superalloy weld metal" ASM Proceedings of the International Conference: Trends in Welding Research, p. 140, 2009.

[125]. White, H., Santella, M., Specht, E.D., " Weldability of Haynes 282 alloy for new fabrications and after service exposure" Energy Materials: Materials Science and Engineering for Energy Systems, 4 (2), p. 84, 2009.

[126]. Ian, M., Michael, W., Christian, W., Bharat, J., Alfred, B., Mechanical and Microstructural Evaluation of Friction Stir processed Haynes 282 Superalloy. Final report - Research experience for undergraduates. Summer 2011. South Dakota School of Mines and Technology.

[127]. Goldstein, J.I., Newbury, D.E., Echlin, P., Joy, D.C., Fiori, C.E., Lifshin, E., "Scanning Electron Microscopy and X-ray Microanalysis", Plenum Press, new York, NY, 1981.

[128]. Kronberg, M.L., Wilson, F.H., "Secondary recrystallization in copper", Journal of Metal, AIME, 1(8), 1949: p. 501.

[129]. Maxwell, D.H., Baldwin, J.F., Radavich, J.F., "New concept in superalloy ductility", Metallurgia, 42(8), 1975, p. 332.

[130]. Kurban, M., Erb, U., Aust, K.T., "A grain boundary characterization study of Boron segregation and carbide precipitation in alloy 304 austenitic stainless steels. Scripta Mater.", 54(6) 2006: p. 1053.

[131]. Goldschmidt, H.J., "Effect of Boron additions to austenitic stainless steel", J. Iron Steel Inst., 209, 1971: p. 910.

[132]. Chen, W., Chaturvedi, M.C., Richards, N.L., "Effect of Boron segregation at grain boundaries on heat affected zone cracking in Wrought IN 718", Metall. Trans. A, 32A, 2001: p. 931.

[133]. Nakkalil R., Richards N.L., Chaturvedi M.C., "Grain boundary liquid film migration during welding of Incoloy 903", Scripta Metall. Mater., 26, 1992: p. 545.

[134]. Strum M.J., Summers L.T., Morris J.W., "The aging response of a Iron based superalloy", Weld. J., 1983; 62: 235.

[135]. Liu, L., Sommer, F., Fu, H.Z., "Effect of solidification conditions on MC carbides in a Nickel-base superalloy in 738 LC", Scr. Metall. Mater., 30, 1994: p. 587.

[136]. Quested P.N., McLean M., "Effect of variations in Temperature Gradient and Solidification rate on microstructure and creep behaviour of IN738 LC". Solidification Technology in the Foundry and Cast House. The Metals Society Coventry England, 1980: p. 586.

[137]. Bower T.E., Brody H.D., Flemings M.C., "Measurement of Solute Redistribution in Dendritic Solidification", Trans. AIME, 236, 1966: p. 615-24

[138]. Scheil E., "Remarks on the crystal layer formation", Z. Metallkd., 34, 1942: p.70.

[139]. DuPont J.N., Robino C.V., Marder A.R., Notis M.R., "Solidification of Nb-Bearing Superalloys: Part II. Pseudo Ternary Solidification Surfaces", Metall. Mater. Trans. A, 29A, 1998: p. 2797.

[140]. Nakao Y., Shinozaki K., "Hot cracking susceptibilities of nickel-base superalloys weld zones". Proc. Int. Conf. on High Temperature Materials, Liege, Belgium, 1990; p. 24.

[141]. Knornovsky G.A., Cieslak M.J., Headley T.J., Romig A.D Jr., Hammetter W.F., "Inconel 718: A Solidification Diagram", Metall. Trans. A, 20A, 1989: p. 2149.

[142]. Thompson R.G., Mayo D.E., Radhakrishnan B., "The relationship between carbon content, microstructure, and intergranular liquation cracking in cast nickel alloy 718", Metall. Trans. A, 22A, 1991: p. 557.

[143]. DuPont J.N., Robino C.V., "The Influence of Nb and C on the Solidification Microstructures of Fe-Ni-Cr Alloys", Script. Mater., 41, 1999: p. 449.

[144]. Backerud L., Carlsson B., Oskarsson R., Mikus M., "A Study of the Nickel-rich and Cobalt-rich Corners of the Systems Ni-Ti-C and Co-Ti-C", Scand. J. Metall., 3, 1976: p. 225.

[145]. David S.A., Vitek J.M., Babu S.S., Boatner L.A., Reed R.W., "Welding of nickel base superalloy single crystals", Sci. and Technol. Welding Joining, 2(2), 1997: p. 79.

[146]. Zupanic, F., Boncina, T., Krizman, A., "Structure of the Ni-base superalloy IN 713C after continuous casting", in T. M. Pollock, R. D. Kissinger (Eds), Proceedings of superalloys conference 2000. TMS 2000: p. 239

[147]. Al-Jarba, K.A., Fuchs, G.E., "Effects of Carbon additions on the as-cast microstructure and defect formation of single crystal Ni-based superalloy", Mater. Sci. Eng. A, 373(1-2), 2004, p. 255.

[148]. Wang, Y.L, Richards, N.L., Chaturvedi, M.C., "Weldability of directionally solidified TMS-75 and TMD-1035 superalloy", Proceedings of the superalloys conference, Champion S Pennsylvania, USA, 19-23; 2004: p. 529.

[149]. Ernst, S.C., Beaslack III, W.A., Lippold, J.C., "Weldability of high-strength, low-expansion superalloys", Weld., J., 68(10), 1989, p. 418.

[150]. Jahnke, B., "High-Temperature Electron Beam Welding of the Nickel-Based Superalloys IN 738LC", Weld. J., 16(11), 982: p. 343s.

[151]. Ojo, O.A., Richards, N.L., Chaturvedi, M.C., "Liquation of various Phases in HAZ during welding of cast IN 738LC", Mat. Sci. Tech, 20(8), 2004: p.1027.

[152]. Ojo, O.A., Chaturvedi, M.C., "Liquation Microfissuring in the weld Heat Affected Zone of an Overaged Precipitation-Hardened Nickel-base Superalloy", Metall. & Mater. Trans. A, 38A, 2007: p.356

[153]. Owczarski, W.A., "Some Minor Element Effects on Weldability of Heat Resistant Nickel Base Superalloys, in Effects of Minor Elements on the Weldability of High Nickel Alloys", Proceedings of a Symposium Sponsored by the Welding Research Council, New York, 6, 1969.

[154]. Smith, C.S., "Grains, Phases, and Interfaces: An interpretation of microstructure", Trans. AIME, 175, 1948: p. 15.

[155]. Kokawa, H., Lee, C.H., North, T.H., "Effect of Grain boundaries on Isothermal solidification during transient liquid phase brazing", Metall., Trans. A. 29A(7), 1991: p. 1627.

[156]. Askay, I.A., Hoge, C.E., Pask, J.A., "Wetting Under Chemical and Nonequilibrium Conditions", J. Phys. Chem., 78(12), 1974: p.1178.

[157]. Chatain, D., Rabkin, E., Derenne, J., Bernardin, J., "Role of Solid/Liquid interface faceting in rapid penetrations of a liquid phase along Grain boundaries", Acta Mater., 49, 2001: p. 1123.

[158]. Lundin, C. D., Qiao, C. Y. P., Swinderman, R.W., "Weld HAZ characterization of modified 800 alloys, Proceedings of the International Trends in Welding Science and Technology", Gatlinburg, Tennessee, USA, 262, 1993: p. 65.

[159]. Miller, W.A., Chadwick, G.A., "On the magnitude of solid/liquid interfacial energy of pure metals and its relation to grain boundary melting". Acta Met. J., 15, 1967: p. 607.

[160]. Radhakrishnan, B., Thompson, R.G., "Liquid film migration (LFM) in the weld HAZ of alloy 718", Scriptal Matall. Materi., 24, 1990: p. 537

[161]. Cam, G., Kocak, M., "Progress in Joining of Advance Materials", Int, Mater. Rev., 43(1), 1998: p.1

[162]. Thompson, R.G., "Microfissuring of Alloy 718 in the weld Heat Affected zone", J. Met., 7, 1988: p. 44.

[163]. Thakur, A., Richards, N.L., Chaturvedi, M.C., "On Crack-free welding of Inconel 738", Int. J. Join Mater., 15(14), 2003: p. 21.

[164]. Karlsson, L., Norden, H., Odelius, A., "Non-Equilibrium grain boundary segregation of boron in austenitic stainless steel, I. Large scale segregation", Acta Metall. 36(1), 1988: p.1

[165]. Osoba, L.O., Ding, R.G., Ojo, O.A., "Improved resistance to laser weld HAZ microfissuring in a newly developed superalloy Haynes 282", Met Trans 2012 (In press)

[166]. Nakkalil, R., Richards, N.L., Chaturvedi, M.C., "The Influence of solidification mode on HAZ microfissuring in nickel-iron base superalloy", Acta Metall. Mater. 41(12), 1993: p. 3381.

[167]. Shidu, R.K., Richards, N.L., Chaturvedi, M.C., "Post-weld heat treatment, cracking in autogenous GTA welded cast IN738LC superalloy", Mater. Sci. and Tech. 23(2), 2007: p. 202.

[168]. Idowu, O.I., "Heat Affected Zone Cracking of Allvac 718Plus Superalloy during High Power Beam Welding and Post-weld Heat Treatment", PhD Thesis, University of Manitoba, 2010

[169]. Nakao, Y., "Study of reheat cracking of nickel-base superalloy, Waspaloy", Transaction of the Japan Welding Society, 19 (1) 1988.

[170]. Prager, M., Shira, C. S., "Welding of Precipitation-Hardening Nickel-base Alloys", Weld. Res. Council bulletin series, 128, 1968: p. 1

[171]. Thamburaj, R., Wallace, W., Goldack, J.A., "Post-weld heat treatment cracking in superalloys", Inter. Met. Rev. 28(1), 1983: p. 1

[172]. Schirra, J.J., Caless, R.H., Halata, R.W., "The effect of Laves phase on mechanical properties of wrought and cast + HIP 718", Superalloys 718, 625, 706 and various derivatives (Ed. Loria, E.A.), 1991: p 375.

[173]. Ojo, O.A., Richards, N.L., Chaturvedi, M.C., "Liquid film migration of constitututionally liquated γ' in weld heat affected zone (HAZ) of IN 738LC superalloy", Scripta Mater. 51(2), 2004: p. 141